Mémoire

Auteur : Panier, Lucy
Promoteur(s) : Dupret, Marc-Antoine; Van Grootel, Valérie
Faculté : Faculté des Sciences
Diplôme : Master en sciences spatiales, à finalité approfondie
Année académique : 2022-2023
URI/URL : http://hdl.handle.net/2268.2/18767

Université de Liège

Master Thesis

Modelling and seismic probing of core-helium burning stars with mixed modes

Master in Space Sciences

Author:
Lucy I. Panier

Supervisor:
Marc-Antoine Dupret

Co-Supervisor:
Valérie Van Grootel

Research Focus

August 16, 2023

Acknowledgements

The process to complete this master thesis has been possible thanks to the help and support I received. I would like to express my gratitude to the people who made that possible.

First and foremost, I am deeply grateful to my supervisor Marc-Antoine Dupret and co-supervisor Valérie Van Grootel for their invaluable guidance and support. I would like to add a special thanks to my professor Mr Dupret for his expertise and patience that have played a crucial role to shape and write this master thesis. I am truly fortunate to have had them as my advisors.

I am grateful to the members of my reading committee, Arlette Noels, Michaël De Becker and Gaël Buldgen. I would also like to thank Arlette Noels and Richard Scuflaire for their generous contribution of knowledge and expertise that has enriched this work and helped me navigate the complexity of the field.

I would like to deeply thank my friends, with a special thanks to Celia and Julie, for their constant help, tears they wiped away, incredible moral support and cheerfulness. I am also thankful to my fellow classmates with whom I shared the complicity and experience of this academic journey.

Lastly, I want to express my sincere gratitude to my family, my pack, whose unwavering support and care, have been a source of strength. A special thanks to my father for his belief in me, which kept my spirits high during this process. I would also like to add a special thanks to Anne-Marie and Jonathan that kept their door opened for more than a year. This peaceful environment significantly contributed to my motivation.

I would not have been able to complete this academic journey without these wonderful people, thank you.

Contents

Chapter 1

Introduction

1.1 Context

The study of stellar pulsations, Asteroseismology, is an important domain of stellar astrophysics. Stellar oscillations can be used to understand the internal structure and dynamics of stars. Indeed, pulsations create some patterns of deformation of the stellar surface that are shown as variations of luminosity and radial velocity when measuring the spectrum. Indirectly, these seismic signatures provide information about the envelope and sometimes the deep interior of a star. This information can be used to learn more about stellar evolution.

Asteroseismology is particularly interesting to study red giants. These bright stars, visible at large distances, have the particularity of having coupled oscillation modes. Their oscillations can resemble pressure modes and gravity modes at the same observed frequency, which are known as mixed mode. The seismic signature resembling gravity mode propagates in deep layers, while the one resembling pressure mode propagates in the extended envelope. This is therefore useful for studying distinct parts of the interior.

In addition, red giants can be used as probes to study the properties of stellar populations in different regions of the Milky Way. Thanks to this, it is possible to access valuable information to study the history of our galaxy. This field is referred to as 'Galactic Archaeology'.

Recent observational advances given by missions such as the NASA's space mission Kepler (2009–2018) and ESA's space mission CoRoT (2006–2012) provided a large amount of high-quality data in stellar physics. This makes it possible to study red giant oscillations with unprecedented observational quality, making a revolution in red giants Asteroseismology.

Given the interest in this field, this work aims to study the physical properties and evolution of red giants in core-helium burning phase. At first, the trend of various physical parameters within the core is analysed for a reference star, and then for a variable envelope mass and core size. This part of the study is based on a code of stellar evolution, *Clés*, developed by the group 'Astrophysique Stellaire Théorique et Astérosismologie' of the Department of Astrophysics, Geophysics and Oceanography of the University of Liège (Scuflaire et al., 2007). The next step aims to extend the study by using another model based on polytropes as approximation. This qualitative framework provides a complement to the discussion and is implemented with a Python code developed for the purpose of this work. We compare the model to the

profiles obtained with *Clés* and discuss the final results.

In the final part of this master thesis, useful concepts of red giants asteroseismology are introduced. We investigate some features of the mixed mode signature: the Brunt–Väisälä frequency, period spacing and large separation from the asymptotic theory. We focus on a reference star, and then study the dependence of these parameters on the envelope mass and core size.

1.2 Stellar Evolution : Red-Giant Stars

This work concerns low-mass red giants in the helium burning phase. These stars are in post-main sequence stage characterised by helium burning in the core. To provide a background to the study of theses celestial bodies, the evolutionary stages from the post-main sequence to the horizontal branch are presented as follows.

1.2.1 Post-Main Sequence

During their evolution, stars spend a large amount of their lifetime on the main sequence where hydrogen is depleted into helium in the core. Central reactions become less efficient when approaching the end of the main sequence, leading to a complete shutdown of the hydrogen burning. This phase is referred to as the **terminal age main sequence (TAMS)**. The transition from the main sequence to the red giant branch (RGB) can be described as an inert helium core, surrounded by a hydrogen burning shell located at the base of the envelope. The H-shell becomes the main source of energy during this phase. As the hydrogen surrounding the He-core is depleting, the shell gradually becomes thinner, while the mass of the helium core continues to increase. This holds until it reaches the so-called Schönberg-Chandrasekhar limit mass. Low- to intermediate-mass stars arrive at the end of the main sequence phase with a He-core mass below this limit.

The evolution of a red giant up to the horizontal branch can be divided into several stages: the Red Giant Branch (RGB), the Zero-Age Horizontal Branch (ZAHB), and finally, the Horizontal Branch (HB) in core helium burning phase. Each of these stages plays a role in shaping a star during its lifetime.

1.2.2 Red Giant Branch

Once the Schönberg-Chandrasekhar limit is reached, the structure of the star readjusts to maintain hydrostatic equilibrium, resulting in the contraction of the core and the expansion of the envelope. As the opacity of the cooling envelope increases, it becomes convective. Finally, the star reaches the base of the Red Giant Branch (RGB).

Throughout the RGB, the outer layers of the star expand and cool, while the convective envelope goes deeper towards the hydrogen shell. This phase is characterised by an increasing luminosity.

As the convective envelope deepens, at some point it encounters a region with distinct chemical compositions compared to the surface. Material from this region is mixed with surface layers, resulting in short phases called "first dredge-up" and

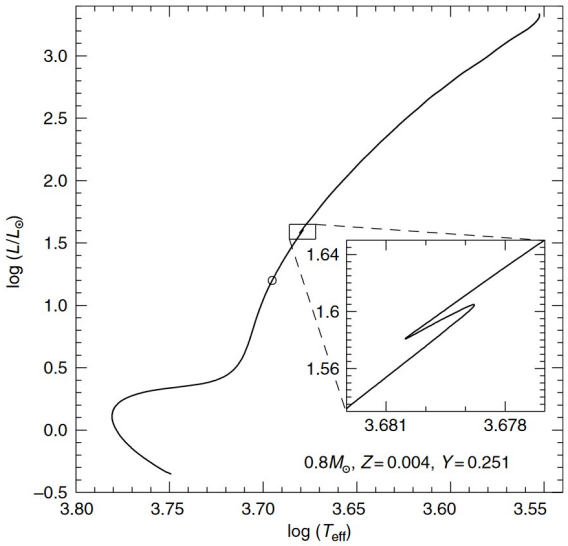

FIGURE 1.1: Red Giant Branch in the H-R diagram.The bump is visible as a zigzag. The edge of the branch is called the tip of RGB. ("The Hydrogen Burning Phase" 2005)

"Bump" visible as a zigzag pattern on the Hertzsprung-Russell (HR) diagram (Fig.1.1).

Throughout the ascension on the RGB, the He-core progressively gains in mass. For low-mass stars ($\lesssim$ 1.8 $M_\odot$), a critical core mass of approximately $\sim$ 0.48 $M_\odot$ is a state where He-burning reactions are initiated. These stars have a degenerate core, leading to a thermal runaway called the **Helium Flash**, marking the end of the red giant phase and the start of the Zero-Age Horizontal Branch **ZAHB**.

In contrast, more massive stars have a less degenerate core, resulting in a gradual onset of helium burning reactions with no helium flash.

1.2.3 Horizontal Branch

The next phase concerns the core helium burning. After the helium flash, the core expands and cools down. This allows quieter He-burning reactions, which marks the beginning of the horizontal branch phase. At this stage, the core is convective due to the sensitivity of the He-burning reactions *3-alpha* (3 He $\rightarrow$ C and when there is enough carbon, C + He $\rightarrow$ O) to the temperature[1]. The end of the HB is reached with the helium exhaustion in the core, producing a He-burning shell, in analogy to the hydrogen exhaustion.

The theoretical boundary of the mixed core in red giants follows a model that includes the so-called semi-convective zone. The following section introduces these concepts and the general equations governing the interior of a star.

1.3 Stellar Structure and General Equations

This section introduces the governing equations of the stellar interior to describe its dynamics, structure and provide a background to apprehend the next Chapters.

The theory is based on some assumptions:

- Stars have a **spherical shape** leading to spherical symmetry and are self-gravitating. The effects of stellar rotation and magnetic field are neglected.

[1] Reactions of He-burning are located close to the centre, where T is higher.

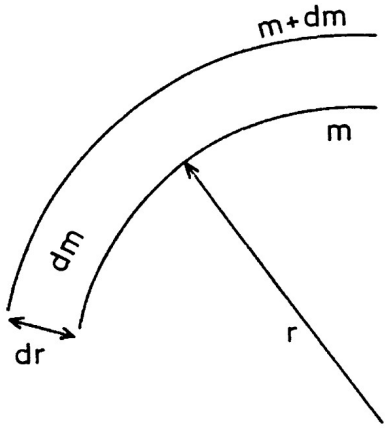

FIGURE 1.2: Illustration of a shell of thickness dr and mass dm within a sphere of radius $\mathbf{r}$ and mass m (Kippenhahn, Weigert, and Weiss, 2013)

- As a consequence of the first assumption, the physical parameters (density, temperature, pressure, ...) only depend on two variables, the radial distance and time, $(\mathbf{r}, t)$.
- We neglect the time variation of the physical parameters meaning they depend on one variable only, the radial distance, $\mathbf{r}$.

For a star spherically symmetric, isolated and static, we obtain the following basic equations.

1.3.1 Equation of Continuity

To study the stellar mass distribution, we define $m(\mathbf{r})$ as the mass contained in a sphere of radius $\mathbf{r}$, within the interior of the star. At the surface, we obtain the total mass, $m(R) = M$.

The mass of a shell, dm, within the sphere (Fig. 1.2) varies with respect to its thickness, dr, according to

$$\mathrm{d}m = 4\pi r^2 \rho \mathrm{d}r,$$

where ρ is the density. This is called the continuity equation of the mass.

The differential equation can be integrated to obtain the mass of the sphere as followed

$$m(r) = \int_0^r 4\pi r'^2 \rho dr'.$$

1.3.2 Equation of Poisson

Usually, the gravitational field of a star can be derived from a gravitational potential Φ, which is a solution to the *Poisson equation*

$$\nabla^2 \Phi = 4\pi G\rho, \tag{1.1}$$

where $G = 6.67408 \times 10^{-11} Nm^2 kg^{-2}$ is the gravitational constant describing the gravitational field

$$g = \frac{Gm}{r^2}.$$

1.3.3 Hydrostatic Equilibrium

The hydrostatic equilibrium is derived from the balance of forces of an element within the interior of a star. Consider a gas column of mass $m(\mathbf{r})$, radial distance $\mathbf{r}$ and density ρ. The **hydrostatic equilibrium** is defined as:

$$\frac{\mathrm{d}P(r)}{\mathrm{d}r} = -\frac{Gm}{r^2}\rho \tag{1.2}$$

It describes the forces applied on the element of gas acting against each other to maintain the structure of a star. The weight of the element must be compensated by the pressure coming from the matter below it, to avoid a collapse or an explosion of a star.

1.3.4 Conservation of Energy

Let us consider a shell of thickness dr, mass dm and radial distance from centre r (Fig. 1.2) inside a sphere of radius r. The power radiated by the sphere is called the luminosity L_r. We assumed the **Local Thermodynamic Equilibrium (LTE)**.

The LTE implies that the rate of energy production of the core is exactly balanced by the rate of energy dL_r transported to outer layers. The source of energy of the core are the nuclear reactions. Recalling that $dm = 4\pi\rho dr$, we obtain the conservation of energy

$$dL_r = 4\pi r^2 \rho\epsilon dr = \epsilon dm,$$

where ϵ is the rate of nuclear energy production per unit mass. Finally, the differential equation becomes

$$\frac{dL_r}{dm} = \epsilon.$$

The luminosity of a sphere of radius r is given with the integration over the mass

$$L_r = \int_0^m \epsilon dm'. \tag{1.3}$$

Luminosity vanishes at the centre $z = 0$ and is equal to the total luminosity at the surface $z = R$.

1.3.5 Energy Transport

There are different mechanisms able to transport energy from hot regions, to cooler ones. Depending on the region of interest, there are three ways to efficiently transfer energy to the outer layers: radiation, conduction and convection. For the purpose of this work, we restrain ourselves to the transport by radiation and convection.

↪ **Radiative transfer**:

The transport of energy by radiation is a process driven by the gradient of temperature. The exchange of energy operates through photons absorption and re-emission. The mean free path of these particles, described by the region opacity, has therefore a huge impact on the process.

Consider a layer of thickness dr within the interior of a star at a distance r from the centre. From the radiative transfer equation in *LTE*, integrated over the whole frequency range, we define the diffusion equation as

$$L_r = -\frac{16\pi r^2 acT^3}{3\kappa\rho}\frac{dT}{dr}, \tag{1.4}$$

Where the luminosity, L_r, is the radiation power crossing a sphere of radius r, $a = 4\sigma/c$ and σ denotes the Stephan-Boltzmann constant.

The process of radiative transfer is always present as long as there is a temperature gradient. The real gradient is defined as

$$\nabla = \frac{d\ln T}{d\ln P}, \tag{1.5}$$

Describing the variation of temperature T with depth, in terms of pressure P.

We explicit the gradient by using the hydrostatic relation $\frac{\mathrm{d}P}{\mathrm{d}r} = -\frac{\rho G m}{r^2}$ and the definition of L_r:

$$\nabla = \frac{d\ln T}{d\ln P} = \frac{P}{T}\frac{\mathrm{d}P/\mathrm{d}r}{\mathrm{d}T/\mathrm{d}r} = -\frac{P}{T}\frac{\mathrm{d}T}{\mathrm{d}r}\frac{r^2}{\rho m G} = \frac{3\kappa P L_r}{16\pi acGmT^4}. \tag{1.6}$$

↪ **Convection**:

The transport of energy by convection is a process driven by the dynamic instability of a region. The transfer occurs through the motion of macroscopic mass elements called *convective bubbles* when the gradient of temperature is noticeably high. Usually, the motion of elements around their equilibrium position follows a dynamic stability implying that these masses come back to their initial position post perturbations. In the case of dynamic instability, also called convective instability, the motion of the elements amplifies the disturbance and trigger large-scale motion which is a mixing of the region.

Convection instability is described through an instability criterion. Consider a layer of thickness dr at a distance r from the centre (Fig. 1.3). As central temperature and density are higher than in outer layers, their gradient is directed towards the centre. We study the motion of a bubble of gas moved from r to $r + \Delta r$.

Intuitively, we have 2 cases:

- **Case 1** if $\rho_{\mathbf{bubble}} > \rho_{\mathbf{surr}}$, the bubble is **more massive** than the surroundings. It is pushed back to its initial position by gravity. This is the **STABLE case**.
- **Case 2** if $\rho_{\mathbf{bubble}} < \rho_{\mathbf{surr}}$, then the bubble is **less massive** than the surroundings. It is pushed further upward. This is the **UNSTABLE case**.

Let us define a theoretical gradient, the adiabatic gradient as:

$$\nabla_{ad} = \left.\frac{\partial\ln T}{\partial\ln P}\right|_S,$$

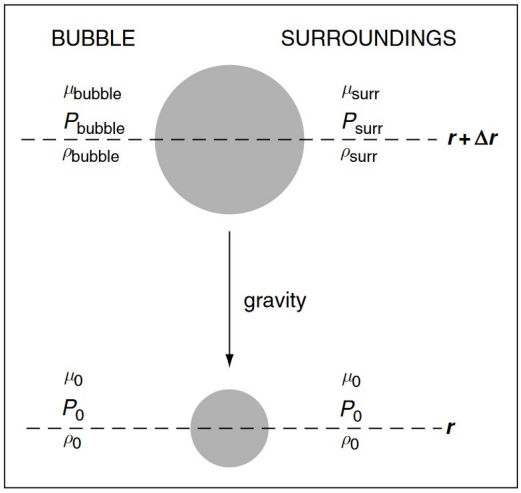

FIGURE 1.3: Schematic presentation of the convective problem ("Equations of Stellar Structure" 2005).

Where S is the constant entropy. The criterion of instability is given by

$$\left.\frac{\partial \ln T}{\partial \ln P}\right|_S < \left(\frac{\mathrm{d}\ln T}{\mathrm{d}\ln P}\right)_{bubble} < \left(\frac{\mathrm{d}\ln T}{\mathrm{d}\ln P}\right)_{surr} \tag{1.7}$$

We denote $\nabla_b = \left(\frac{\mathrm{d}\ln T}{\mathrm{d}\ln P}\right)_{bubble}$ the bubble gradient and $\nabla = \left(\frac{\mathrm{d}\ln T}{\mathrm{d}\ln P}\right)_{surr}$ the gradient of the medium (real gradient).

Therefore, the **convective instability condition** is

$$\nabla_{ad} < \nabla_b < \nabla \;\Rightarrow\; \nabla > \nabla_{ad}\ . \tag{1.8}$$

1.3.6 Schwarzschild criterion

The real gradient within the interior of a star is difficult to determine. If there is convection in addition to radiative transfer then luminosity is the result of the two contributions, $L = L_r + L_c$. We define another theoretical gradient based on the definition of the real gradient (Eq.1.5), but using the total luminosity:

$$\nabla_{rad} = \frac{d\ln T}{d\ln P} = \frac{3\kappa P L}{16\pi acGmT^4}. \tag{1.9}$$

This is called the radiative gradient. It expresses the required theoretical gradient needed to ensure the transfer of the whole produced energy by radiation and it is larger than the real gradient as $L > L_r$. The Schwarzschild criterion comes from the convective instability criterion (Eq.1.8) where we assumed $\Delta\mu = 0$ and used the ideal gas law. We can write:

$$\frac{\nabla_{rad}}{\nabla} = \frac{L}{L_r}.$$

If $\nabla > \nabla_{ad}$ then $\nabla_{rad} > \nabla$, which gives the Schwarzschild criterion, another form of the convective instability condition:

$$\nabla_{ad} < \nabla_{rad}\ . \tag{1.10}$$

When the radiative gradient is too large, the transport by radiation of L_r to outer layers is not efficient enough to ensure the whole transfer. An instability is created and drive convective motion that can share the weight of carrying such an amount of energy L.

1.3.7 Ledoux criterion

The Ledoux criterion is a general case of the Schwarzschild criterion and was proposed by the astrophysicist Paul Ledoux. In this case, the radial chemical composition of the region of interest is variable i.e. $\nabla\mu \neq 0$. The element of matter passes through a medium of different compositions as it moves through the region. The ideal gas law is replaced by a general equation of state:

$$\frac{\mathrm{d}\rho}{\rho} = \alpha\frac{\mathrm{d}P}{P} - \delta\frac{\mathrm{d}T}{T} + \phi\frac{\mathrm{d}\mu}{\mu}, \tag{1.11}$$

where

$$\begin{cases} \alpha = \frac{\partial \ln\rho}{\partial \ln P}|_{T,\mu} \\ \delta = \frac{\partial \ln\rho}{\partial \ln T}|_{P,\mu} \\ \phi = \frac{\partial \ln\rho}{\partial \ln\mu}|_{P,T} \end{cases}$$

And α , δ , ϕ $= 1$ describes an ideal gas.

Let us make the following assumptions and recall some previous results:

- The equilibrium pressure $P_s = P_b$ between the bubble element and the surroundings implies that $\mathrm{d}P_s = \mathrm{d}P_b$.
- We assume that the molecular weight of the element does not change, $\mathrm{d}\mu_b = 0$, in contrast to its surroundings where $\mathrm{d}\mu_s \neq 0$.
- The convective instability implies $\rho_b < \rho_s$. Therefore, we write $\mathrm{d}\rho_b < \mathrm{d}\rho_s$.
- The pressure gradient is negative i.e. $\mathrm{d}P/P < 0$

From equation (1.11), we obtain the following inequality

$$\left(\alpha\frac{\mathrm{d}P}{P}\right)_b - \left(\delta\frac{\mathrm{d}T}{T}\right)_b + \left(\phi\frac{\mathrm{d}\mu}{\mu}\right)_b < \left(\alpha\frac{\mathrm{d}P}{P}\right)_s - \left(\delta\frac{\mathrm{d}T}{T}\right)_s + \left(\phi\frac{\mathrm{d}\mu}{\mu}\right)_s \tag{1.12}$$

$$\Leftrightarrow \left(\frac{\mathrm{d}T}{T}\right)_b > \left(\frac{\mathrm{d}T}{T}\right)_s - \left(\frac{\phi}{\delta}\frac{\mathrm{d}\mu}{\mu}\right)_s \tag{1.13}$$

$$\Leftrightarrow \left(\frac{\mathrm{d}T}{T}\frac{P}{\mathrm{d}P}\right)_b < \left(\frac{\mathrm{d}T}{T}\frac{P}{\mathrm{d}P}\right)_s - \left(\frac{\phi}{\delta}\frac{\mathrm{d}\mu}{\mu}\frac{P}{\mathrm{d}P}\right)_s \tag{1.14}$$

$$\Leftrightarrow \left(\frac{\mathrm{d}\ln T}{\mathrm{d}\ln P}\right)_b < \left(\frac{\mathrm{d}\ln T}{\mathrm{d}\ln P}\right)_s - \left(\frac{\phi}{\delta}\frac{\mathrm{d}\ln\mu}{\mathrm{d}\ln P}\right)_s. \tag{1.15}$$

Where:

$$\nabla = \frac{d\ln T}{d\ln P} \ , \ \nabla_{ad} = \left.\frac{\partial \ln T}{\partial \ln P}\right|_S \ , \ \nabla_\mu = \frac{d\ln \mu}{d\ln P} \ . \tag{1.16}$$

Using realtion 1.8, equation 1.15 becomes

$$\Rightarrow \ \nabla_b < \nabla - \frac{\phi}{\delta}\nabla_\mu \tag{1.17}$$

$$\Leftrightarrow \ \nabla_{ad} < \nabla - \frac{\phi}{\delta}\nabla_\mu \tag{1.18}$$

$$\Leftrightarrow \ \nabla_{ad} < \nabla_{rad} - \frac{\phi}{\delta}\nabla_\mu \tag{1.19}$$

$$\Leftrightarrow \ \nabla_{rad} > \nabla_{ad} + \frac{\phi}{\delta}\nabla_\mu \tag{1.20}$$

Defining the ledoux gradient $\nabla_L = \nabla_{ad} + \frac{\phi}{\delta}\nabla_\mu$, equation 1.20 is the **Ledoux criterion** of dynamical instability. From this equation we see that if $\nabla_\mu = 0$, the Schwarzschild criterion appears.

Furthermore, the case $\nabla_\mu > 0$ has a stabilising effect. This comes from the moving bubble that encounters a medium of smaller molecular weight. Its motion is thus slowed down because the element is pushed downwards. In this case of **dynamic stability** for a radiative layer then $\nabla_{ad} = \nabla$ and we assume no heat exchange $\nabla_b = \nabla_{ad}$ such that the elements rise adiabatically. This gives the Ledoux criterion for stability:

$$\Leftrightarrow \ \nabla_{rad} < \nabla_L \tag{1.21}$$

1.3.8 Overshooting

In this case, a convective overshooting region refers to an **extension** of a convective core. It describes a region where $\nabla_{rad} < \nabla_{ad}$ but where matter is still mixed with the convective core because of the inertia of the elements accelerated there. In other words, this is a mechanism where the mass elements rising in the convective region continue their motion after **passing** the convective boundary, even if there is no longer a net force pushing them upward.

This is due to their **inertia** that gives them a non-zero velocity. After some distance, they are slowed down in the extended region and pushed backwards. As a consequence, mixing occurs beyond the Schwarzschild boundary. This extends the mixed core size. Overshooting can have a significant influence on the evolution of a star. This extra-mixing can provide more burning material to the core, and therefore additional fuel for nuclear reactions.

1.3.9 Semi-Convection

Semi-convection refers to a layer where the Ledoux criterion for stability (section 1.3.7) is operating while the Schwarzschild's criteria is unstable.

$$\nabla_{ad} < \nabla_{rad} < \nabla_{ad} + \frac{\phi}{\delta}\nabla_\mu \tag{1.22}$$

This comes from the variable chemical composition creating a molecular weight gradient $\Delta\mu > 0$ that acts against convection. The result is that a displaced mass element oscillates up and down at a growing amplitude and goes higher and higher into the layer. This is a region of slow mixing.

Chapter 2

Theoretical Modelling

2.1 Introduction

This chapter explores the behaviour of several physical parameters of a given star throughout its evolution on the horizontal branch. These include temperature, luminosity, density, opacity and trajectory in the Hertzsprung–Russell (H-R) diagram. The modelling is performed using a theoretical model, *Clés*, covering the entire sequence from the beginning of helium core burning to its completion. By varying some of the initial parameters of the star, the link between the variables is investigated and the results, interpreted.

Throughout this analysis, the dependence of the evolutionary sequence on the envelope mass and size of the mixed core is examined.

2.2 Modelling

This section introduces the code, *Clés*, and the initial parameters of interest.

2.2.1 CLES

Clés, for *Code Liégeois d'Évolution Stellaire*, is a stellar evolution code developed by the group "Astrophysique Stellaire Théorique et Astérosismologie" of the Department of Astrophysics, Geophysics and Oceanography of the University of Liège (Scuflaire et al., 2007). The version used for this work is able to compute the full sequence of evolution of a star on the horizontal branch with a set of initial parameters. The code is separated into two programs, one focusing on the computation of the first model of the sequence, **Zero-Age Horizontal Branch (ZAHB)**, and the other one on computing the remaining models of evolution on the **Horizontal Branch (HB)**. For each step of the evolution, the set of physical parameters of the star are computed on a grid of points, from the centre to the surface. The code uses the concept of semi-convective, convective and radiative regions discussed in the introductory Chapter 1. Our first modelling lead to convergence problems when the end of the core helium burning phase was reached. In a new version of the code, this problem was solved by blocking any further extension of the convective core and suppressing mixing in the semi-convective layer when a critical value of the central helium abundance is reached.

This theoretical modelling is useful in the field of Asteroseismology.

2.2.2 Semi-Convection Problem

As previously seen in Chapter 1, the radiative gradient in a convective layer is higher than the adiabatic gradient ($\nabla_{rad} > \nabla_{ad}$). At the boundary of the convective zone, the radiative gradient drops, becomes equal to the adiabatic gradient ($\nabla_{rad} = \nabla_{ad}$) then goes below to form a radiative layer ($\nabla_{rad} < \nabla_{ad}$). A discontinuity in the radiative gradient profile appears at the boundary of the mixed core. The origin of this drops is explained as:

↪ The nuclear reactions occurring at the centre of the convective core transform helium into heavier elements (carbon then oxygen). The new chemical elements are **homogenised** by the mixing core. As a result, the outer region has a chemical composition that is **distinct** since no reaction occurs there and it is not part of the mixing. This creates a discontinuity in the composition profile on the border.

↪ Given these features, the opacity profile has a step shape on the mixed core boundary. The origin of this discontinuity is presented with a simple model in Chapter 3 (Eq.3.12). The opacity is mainly due to the **free-free transition** and **electron scattering**. These processes strongly depend on the atomic number of metallic elements: Z^2. While the mixed core increases in mass, Z increases. The profile is therefore different between the two regions.

↪ Finally, the discontinuous drop of the **radiative gradient** on the boundary is explained by the strong **dependence** on **opacity** shown with its definition (Eq.1.9).

The challenge in modelling a core-He burning star lies in handling the intermediate zone between the border of the convective zone and the outer radiative zone. When the star evolves, the radiative gradient tends to increase beyond the convective zone. This poses a problem when dealing with the mixing of the core because the rise of the radiative gradient could lead to the creation of an additional convective layer, thereby, misidentifying the border of the convective core. This is a numerical issue that might result in helium being re-injected into the core, which is not supposed to happen.

To prevent the radiative gradient from surpassing the adiabatic gradient, the model introduces a semi-convective zone (Section 1.3.9) by imposing a non-zero molecular weight gradient ∇_μ and ensuring that the adiabatic and radiative gradients are equal $\nabla_{rad} = \nabla_{ad}$ throughout the layer. This guarantees that the radiative gradient remains limited by the adiabatic gradient. The issue is illustrated in Figure 2.1.

The semi-convective region is therefore, considered as another extension of the mixed core but where the mixing is slow, causing a variable chemical composition. The real gradient ∇ is fixed to be equal to the adiabatic gradient ($\nabla_{ad} = \nabla$) up to the discontinuous boundary of the semi-convective layer.

2.2.3 General Structure

The model structure of the interior can be divided into several regions:

- The **mixing core** encompasses the Schwarzschild region and the overshooting region (Section 1.3.6 and 1.3.8) during the early stages of evolution. The core mass of a star grows throughout its evolution on the horizontal branch. The

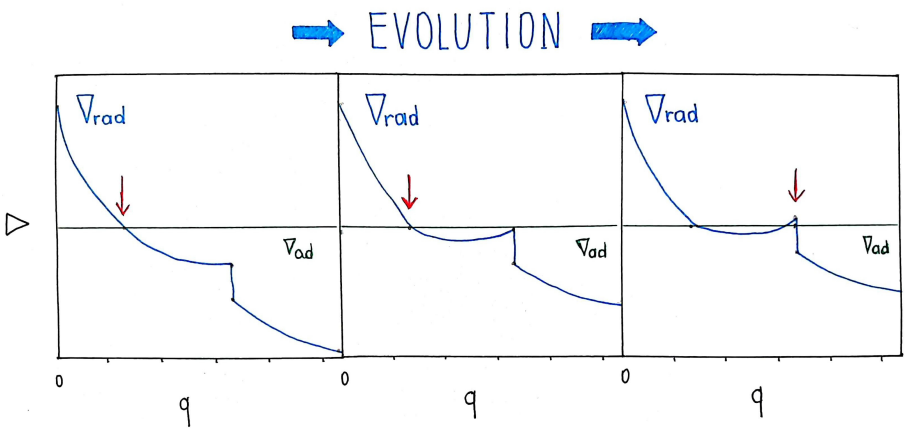

FIGURE 2.1: Schematic figure illustrating the semi-convection problem.

model assumes a homogeneous chemical composition, following the assumption made for the Schwarzschild criterion.

- Beyond the overshooting region, the rise of the radiative gradient leads to the presence of a **semi-convective** region that extends the core, as discussed previously (Section 2.2.2). In this region, the chemical composition is variable, resulting in a non-zero molecular weight gradient.
- A **radiative** helium region lies between the convective core and the hydrogen burning shell.
- An **hydrogen burning shell** surrounds the core. Within this shell, hydrogen is being depleted and transformed into helium through the main chain of reactions, the *CNO cycle*.
- Above it, the envelope is mainly convective up to the photosphere. In this work, our primary focus is on the core and the hydrogen-burning shell.

2.2.4 Initial Parameters

The computation of a full sequence of evolution with *Clés* is based on several initial parameters as variables, including the mass of the helium core, total mass, relative size of the overshooting layer, metallicity, etc. Table 2.1 summarises the default values of the parameters of interest.

The values are expressed in relation to the solar radius, solar mass, total mass of the chemical composition, etc. Let α_{ov} denotes the overshooting region in units of $\Delta \log P$, $\mathrm{Y_{crit}}$ the critical mass fraction of central helium, $\mathrm{M_{He}}$ the relative mass of the helium core, Z the metallicity, and M the total mass:

Initial Parameters	Values
α_{ov}	0.50
M ($M_\odot$)	1
Y_{crit}	0.1
Z	0.014
M_{He} ($M_\odot$)	0.45

TABLE 2.1: Some of the initial parameters, by default, of a sequence of evolution computed by the code *Clés* are as follows.

The ones discussed in this work are the following:

- **Total Mass** The evolution of physical parameters is investigated by varying the initial total mass of the star.

  1) The first sequence is computed using a total mass of reference, $1M_\odot$ in order to analyse the behaviour of the variables throughout the HB. The other parameters are kept at their default value.

  2) Several sequences are computed by altering the initial total mass of the star, enabling an analysis of how these variables depend on mass.

- **Overshooting parameter α_{ov}** The influence of the overshooting layer is examined by changing the default value (0.50) to a small layer (0.15). This comparison makes it possible to distinguish between a significant overshooting and a nearly nonexistent overshooting.

2.3 Results and Discussion

In this section, we discuss the results of the computed sequence for various physical parameters. The figures extracted from the evolutionary sequence are displayed as a set to visualise the behaviour.

2.3.1 Reference Mass

The first part of the results present a reference mass of $1M_\odot$.

H-R Diagram

As a start, we examine the Hertzsprung-Russell diagram of the reference star. Figure 2.2 illustrates the trajectory followed by the star during its evolution on the horizontal branch. The markers represent specific evolutionary steps, along with their corresponding central helium abundances Y_c.

The loop observed at the beginning of the trajectory may be attributed to the onset of core helium burning. The star total luminosity gradually decreases on the horizontal branch, while the effective temperature shows a slight increase. At a state around Y_c= 0.34, a bifurcation appears in the trajectory. From this point, luminosity increases while effective temperature slightly decreases.

Surface luminosity is influenced by internal luminosity. Studying the trend of the internal physical parameters can help to interpret this trajectory. This is precisely

what is explored in the upcoming sections.

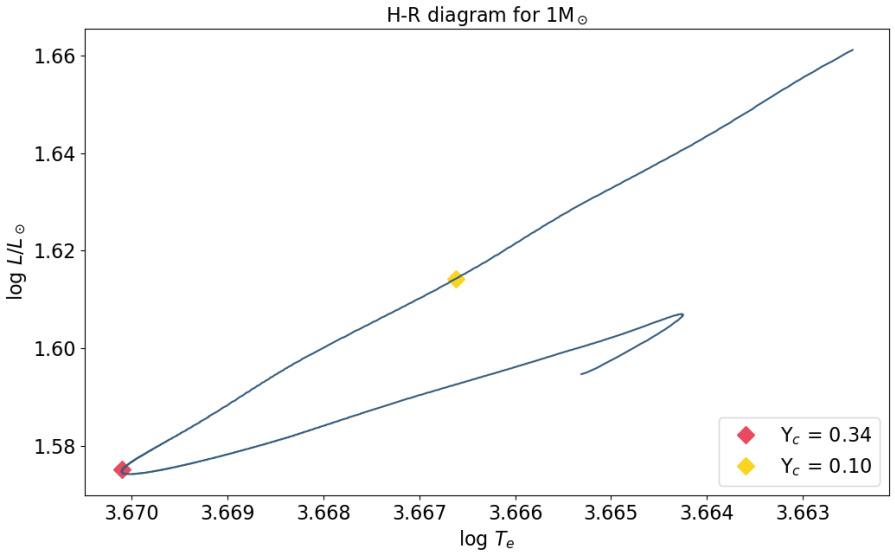

FIGURE 2.2: H-R diagram for 1 $M_\odot$ core-He burning star. The markers indicate a state of central helium abundance (Y_c=0.34 in red and Y_c = 0.10 in yellow)

Luminosity

To investigate the H-R trajectory, we examine the local luminosity within the interior of the star, focusing on the H-shell and the core. These regions provide the energy source of the star and their combination influences the surface luminosity. The shell and He-core luminosities are the powers produced by nuclear reactions in, respectively, the He-core and the H-shell.

Let m_0 be the mass of a sphere of radius $\mathbf{r_0}$, where $0 < \mathbf{r_0} < \mathbf{r_{shell}}$, and M be the total mass. Then, theses parameters are defined as:

$$\begin{cases} L_{\text{He}} = \int_0^{m_0} \epsilon \mathrm{d}m = L(m_0) \\ L_{\text{shell}} = \int_{m_0}^{M} \epsilon \mathrm{d}m = L(M) - L(m_0). \end{cases}$$

In Figure 2.3, several regions in the central part of the star can be observed. The physical parameter (in this case, luminosity) is plotted as a function of the relative mass $m/M_\odot$ which covers the centre up to the H-shell. The orange line delimits the convective core (following Schwarzschild criterion) and includes the extension of the overshooting layer. The black line defines the boundary between the core and the hydrogen burning shell. Further descriptions of these regions will be made in Section 2.3.1 with the help of the gradients profile. While central helium is burning, luminosity tends to increase in the core and decrease in the shell.

Figure 2.3 illustrates this trend between the early model Y_c= 0.93 and the middle state Y_c = 0.52 (panels 2.3a and 2.3b). The plateau observed at first, in the core then in the shell, comes from the energy transfer under thermal equilibrium where

$dL/dm = \epsilon_0$ in the entire layer. There is no other source and loss of energy throughout the region than nuclear reactions of **He-burning** at the centre and **H-burning** in the shell.

Later in the evolution, the observed trend changes in the shell. In fact, in Figure 2.3c, starting around $Y_c = 0.34$, the decrease in L_{shell} slows down and no longer compensates for the increase in L_{He}. As a consequence, the surface luminosity, which is a combination of the two, stops decreasing and starts to increase. Figure 2.4 shows the L_{shell} and L_{He} profile compared to the variation of the central abundance of helium. As Y_c decreases throughout the horizontal branch, the figure shows the whole evolution of the He-core and shell luminosity.

The L_{shell} decreases during the sequence of evolution then increases at the end, when the fraction of helium reaches a critical value, $Y_c = 0.10$. This shows the reactivation of the shell observed in Figure 2.3c. He-core luminosity, on the other hand, tends to increase during the evolution until the critical state $Y_c = 0.10$, where core-He burning reactions shut down.

$\hookrightarrow$ Now, we can understand the H-R diagram much better:

The total luminosity comes from the source of energy. It is then significantly influenced by the H-burning shell surrounding the He-core. A decrease of L_{shell} induces a decrease of the surface luminosity. That explains the first trajectory of the star on the evolutionary diagram. In addition, the onset of the core-He burning at the beginning induces a small bump observed in L_{shell} profile and a loop in the H-R diagram. At the end of the sequence, the reactivation of the L_{shell} combine to the increasing L_{He} affects the total luminosity and as a consequence, it draws a bifurcation in the H-R diagram.

In order to investigate the trend followed by the luminosity, other parameters need to be analysed. As mentioned in Chapter 1, the local luminosity mainly depends on nuclear rate ϵ, opacity and temperature.

Nuclear Reactions

The luminosity trend can be investigated by looking at the source of energy, i.e. the nuclear rates. The rates can be observed in Figure 2.5 shows in the deep interior. The helium burns mainly through the *3-α reaction*, ϵ_{He} while the hydrogen burning into helium occurs through the *pp-chain* and the *CNO cycle*[1]. As expected, the helium burning from the *3-α reaction* is located at the centre of the star. this comes from the high **sensitivity** to temperature which increases towards the centre. On the other hand, the H-burning is located in the shell surrounding the core.

Following the evolution, the first two panels (2.5a and 2.5b) show the nuclear rates profiles between $Y_c = 0.93$ and $Y_c = 0.52$. The shell decreases in activity while the hydrogen is being depleted into helium. In the core, the helium burning continues. This is a first result that gives us an indication of why the shell luminosity decreases while the core luminosity increases.

[1] CNO cycle is more efficient here.

The last panel in Figure 2.5c shows another interesting result occurring at the end of the sequence. The nuclear reactions in the shell that were previously decreasing are starting to increase after passing the critical value Y_c=0.10. As previously mentioned, the shell luminosity increases gradually starting from roughly the same Y_c. This confirms a reactivation of the shell at the end of the sequence. Furthermore, we can see once more that the convective core mass decreases at this stage.

Temperature

The temperature profile contributes to the increasing luminosity at the centre. Indeed, figure 2.6 shows that during the evolution, the central temperature increases. The last panel, 2.6c, shows that even at the end of the sequence, for this example $Y_c = 2.57\ 10^{-4}$, its trend remains the same in the core. This temperature increase is small but since the *3-alpha reactions* are extremely sensitive to the temperature, this leads to a significant increase of L_{He}.

Opacity

The opacity profile (Fig. 2.7), indicates that central opacity increases throughout the evolution. The reason behind this trend is investigated in the next Chapter 3. An increase of opacity is accompanied by an increase of the convective core mass.

There are some discontinuities in the profile. They are actually due to a discontinuity in the chemical composition profile. Indeed, in the first panel 2.7a, we see that the core-He burning creates a chemical composition distinct from the outer core and that it draws a discontinuity of the opacity profile at the border. This gap becomes larger as the core-He burning continues.

The third panel highlights the effect of the semi-convective zone on the profile. It displaces the previous discontinuity at its upper boundary and creates a zone of variable chemical composition within it. This is in order to stabilise the mixing and ensure equal gradients ($\nabla_{rad} = \nabla = \nabla_{ad}$). Beyond the semi-convective zone, the composition remains homogeneous and distinct from what the inner zone. The convective core, overshooting zone and semi-convective zone are illustrated in Figure 2.10b.

At the end of the sequence, while the convective core mass decreases, the chemical composition no longer changes as a result of the end of mixing. This leaves the discontinuities of the profile intact as shown in Figure 2.8.

Furthermore, from chapter 1, we learned that the radiative gradient is sensitive to opacity and that its behaviour determines the dynamics of a region (convective, radiative). Therefore, it is interesting to study gradients, considering what we know about the profiles of luminosity and opacity.

Gradients

The adiabatic, radiative and real gradients (∇_{ad} , ∇_{rad} , ∇) are useful parameters to understand the delimitation of the convective and semi-convective layers. Figures 2.9 and 2.10 show the evolution of these gradients and illustrate the various layers. Looking at the early and middle stages of the evolution (3 panels of Fig.2.9), we confirm that the large value of the radiative gradient at the centre explains the convective core. Furthermore, we previously observed that the core opacity tends to increase in

time, leading to energy confinement. This is correlated with the high value of the radiative gradient.

At the convective boundary, the radiative gradient becomes lower than the adiabatic gradient. Therefore, outside the convective core, the medium is radiative up to the convective envelope, which is not studied in this work. When the gradient rises in the overshooting region to meet the adiabatic gradient, a semi-convective layer appears. The extension of the semi-convective layer with the evolution causes the motion of the discontinuity boundary towards the shell. Finally, after reaching the critical state Y_c=0.10, the semi-convective layer disappears and the core-He burning reactions shut down (Fig.2.11).

Density

In previous figures, we observed a contraction of the convective core when approaching the total exhaustion of central helium. The density profile is interesting to study. Figure 2.12 shows 3 stages of evolution. From the first panel to the second, density has a decreasing trend. A discontinuity on the mixed core boundary appears rather quickly after the start of the core-He burning (panel 2.12b). This comes from a discontinuity in the chemical profile due to the nuclear reactions: the mean molecular weight μ has a discontinuous drop on the mixed core boundary due to the core mass increase. Density depends on the latter through the ideal gas law ($\rho \propto \mu P/T$). While temperature and pressure are continuous parameters, density is affected by the discontinuity of μ. With the same reasoning, the semi-convective upper boundary carries the discontinuity as shown in the last panel 2.12c.

The central density decreases until reaching a helium abundance around $Y_c = 0.34$. From that stage, the it increases (Fig. 2.13). In other words, approaching the critical value $Y_c = 0.10$ induces a drastic change similar to the previously discussed shell luminosity. Beyond this stage, the last panel 2.13c shows that the core mass decreases, leading to an increase of the entire density profile. This change of regime is mainly due to the exhaustion of the available fuel. This is particularly critical in this case as three helium nuclei need to meet simultaneously to fuse. Fuel exhaustion of this kind, lead to the core contraction.

Relation (ρ_c , T_c)

The relation between the central temperature and density (Fig. 2.14) reveals that while T_c increases throughout the evolution, ρ_c decreases until reaching a state around y_c=0.34. From there, it increases. The same results was observed on the density profile as a function of the mass ratio.

Dependence μ

Why density decreases in the core while temperature increases ? To intuitively investigate this trend, let us remember that these parameters are related to each other through the ideal gas law:

$$T \propto \frac{P}{\rho}\mu$$

the mean molecular weight μ increases in the core during the evolution. The study of the relation between temperature, pressure and density reveals that temperature is more sensitive to the mean molecular weight tendency than density. Indeed, the logarithmic dependence T-P (Fig.2.16) compared between two models extracted from the sequence of evolution (Y_c=0.90 and Y_c=0.30), shows that it is not fixed in time (the figure translates). On the other hand, the logarithmic dependence ρ-P (Fig.2.17) compared with the same states (Y_c=0.90 and Y_c=0.30), shows that the logarithmic relation between ρ and P remains fixed in time. In other words, when the central μ increases, to keep the ratio ρ/P constant, the central temperature increases as well. This idea is explained more visually with the schematic figure 2.15.

Physically, it can be explained as follows. When temperature increases due to the increase of the core mass, the nuclear reaction rate also increases. To prevent the core from producing too much energy compared to what is transported outside the region (which would cause a thermal disequilibrium), the convective core mass increases. This expansion affects the reaction rate because it causes a decrease of the probability of collision between particles (helium atoms have to meet for the *3-α reaction*). This way, the core energy production is kept under control.

Finally, the constant slope in the logarithmic relation between pressure and density (Fig.2.17) forms the research question explored in Chapter 3, where we use the polytropes model to express pressure in terms of density. The core of the idea comes from the results of this Chapter: $lnP \sim \gamma\ ln\rho + cst$.

Conclusion

The overall results can be understood as follows: After the onset of core-He burning, the evolution on the horizontal branch begins. The core mass increases with the nuclear reactions. In parallel, the central temperature, luminosity and opacity increase. To maintain control of the energy production, the density decreases. Meanwhile, the activity of the shell decreases as the hydrogen is depleted into helium. This causes a decrease of the shell luminosity and the surface luminosity.

However, when reaching a value of central helium abundance in the range [0.34-0.32] the material becomes poor which decreases the probability of reaction. To maintain the needed energy production, either temperature or density must increase. As T is already increasing, a change in the density profile has the most impact. This way, the central density increases while the central helium comes closer and closer to the critical value $Y_c = 0.10$. From this critical abundance, the core-He burning shuts down due to the fuel exhaustion. To prevent the star from going out of equilibrium, the entire core contracts and the envelope expands. This induces a temperature increase in the shell and causes a reactivation of the hydrogen burning. The shell luminosity increases in parallel to the surface luminosity. This entire phase explains the bifurcations observed in some profile such as the density and the H-R diagram, around and below Y_c=0.34.

2.3.2 Envelope Mass Dependence

Let us now investigate the dependence on the envelope mass of these variables. To quantify this impact, we modify the total mass of a reference star, since the mass of the helium core is fixed.

H-R Diagram

From figure 2.18, we observe the dependence on the envelope mass of the evolution of red giant stars. The trajectories are distinct from the start. The higher the mass, the higher is the total luminosity and the effective temperature. A bifurcation of the trajectory appears for each star and the latter occurs around the same central helium abundance ($Y_c \in [0.34,0.35]$). Finally, we notice a strange behaviour for 1.2 $M_\odot$, 1.6 $M_\odot$ and 1.7 $M_\odot$ after the critical helium mass fraction Y_c=0.10. The solution seems to explode and this is not physical. It is most likely an effect of the numerical resolution in the extreme case of $Y_c \to 0$.

Luminosity

Figure 2.19 shows the luminosity profile for stars of different masses. The central helium value Y_c used as reference for the plots follows the mass of reference, $1M_\odot$. The luminosity profiles are at the same age but not exactly the same Y_c.

At the beginning of the He-core burning (panel 2.19a), luminosity is the same for each mass in the core, and different in the envelope: the helium core of each mass has the same initial mass M_{He}, while the envelopes have different masses and sizes from the start. The weight of the envelope above the H-shell is larger for a more massive star. The temperature and luminosity of the shell are therefore higher and so is the total luminosity. This is similar to the well-known mass luminosity relation in main sequence stars. However, the slope of the "mass-luminosity" relation is much smaller during the core helium burning phase ($L \propto M$) compared to the main sequence, where typically $L \propto M^3$.

While the He-core grows in mass, the luminosity profiles have the same trend compared to the one discussed for the reference mass. L_{He} increases with time while L_{shell} decreases. However, the gap between the set of luminosities increases in the core during the evolution. The higher is the mass of a star, the higher becomes the core luminosity. Let us also notice that the core mass grows slightly further for a more massive star (panel 2.19b). Finally, the last panel 2.19c shows that the shell luminosity starts to increase beyond Y_c=0.10.

Furthermore, the envelope mass seems to have an effect on the evolution rate. The He-core luminosity profile as a function of the age (Fig. 2.20a) and then Y_c (Fig. 2.20b), highlights that by varying the total mass, the time-scale of evolution is different. A more massive star has a larger envelope and evolution seems faster. In other words, the same age does not correspond to the same central helium abundance. He-core reaches central helium exhaustion earlier for higher masses. This can also explain why the He-core luminosities for the set of stars separate from each other during the evolution. The cores evolve at a different rate and as a consequence, the corresponding luminosities increase at a different rate. This result might be understood as follows: the higher the mass, the higher is L_{shell}, then the faster is the progression of the H-shell inside the envelope. As a consequence, the changes of T and ρ inside the shell and below it are faster and the increase of the He-burning efficiency is also faster.

Relation (ρ_c , T_c)

Let us examine the relation between central density ρ_c and central temperature T_c in Figure 2.21, as discussed previously for the reference mass.

The bifurcation of density occurs at the same Y_c for the entire set of stars (Y_c $\in$ [0.34, 0.32]). This supports the previous explanation: a poor abundance of central helium significantly affects the rate of nuclear reactions as the probability of reaction decreases tremendously. To compensate for this effect and maintain the production of central energy, the convective core mass decreases (central density bifurcation in the profile). At some point, helium exhaustion becomes so critical (Y_c=0.10) that this mechanism is not efficient anymore. This also affects the shell that undergoes a reactivation. Finally, as the entire core contracts, the envelope expands and cools down, explaining the decreases of the surface temperature in the H-R diagram.

Conclusion

In conclusion, the envelope mass has an effect on the evolution of a star. From the beginning, the initial total luminosity and temperature are affected by a change of mass. The evolution rate seems to be also affected by the envelope mass since the more massive is a star, the faster it reaches the central helium exhaustion. Finally, a **central** contraction of the core appears at a similar state for the entire set of stars, in the range [0.34,0.32]. This supports with the idea of a lack of fuel that tries to be compensated until the mechanism is no longer efficient to sustain the core-He burning (Y_c=0.10).

2.3.3 Overshooting Variation

We use the same approach, by changing the size of the overshooting region. The stars of interest in this discussion are the reference mass ($\alpha_{ov} = 0.50$) and the same envelope mass with a small overshooting parameters $\alpha_{ov} = 0.15$.

H-R Diagram

As a starting point, we can examine at the H-R diagram (Fig. 2.22). The trajectories have a slight difference marked at the beginning of the sequence and at the bifurcation. Despite these small gaps aside, the trajectories are similar. This small change implies that the size of the overshooting region does not have a **significant** impact on the evolution of the star.

Gradients

To obtain a better understanding of the internal differences between the pair of stars, we examine the gradients closely. In the **first model** of the sequence, the size of the mixed core is clearly distinct (Fig. 2.23a) depending on the overshooting size. As a consequence, the radiative gradient is different locally leading to a variation of the size of the mixed core. Later in the evolution, we observe that the rise of the gradient does not occur at the same time by varying the overshooting. In fact, the semi-convective layer appears faster in the evolution of a star with a small overshooting.

As an example, in the selected figure 2.24, we observe that the overshooting layer and the semi-convective layer compensate each other in size. The size of the mixed core remains therefore approximately the same for both stars. As the discontinuity

at the border of the mixed core is almost at the same mass ratio m/M, the structure of the star is similar. This means that the rest of the star is less affected by the overshooting change than the core. However, the size difference of the semi-convective region does affect the chemical profile. As mentioned earlier, the semi-convection creates a variable chemical profile. A larger semi-convective region implies that the modification of the chemical profile extends further and is greater, as observed in Figure 2.25. The chemical composition of the core affects the structure of the star, but as the difference remains small compared to the entire star, it is not significant. This also explains why the difference in the H-R diagram is small.

Furthermore, As mentioned previously, the temperature gradient ∇ is fixed as $\nabla = \nabla_{ad}$ within the mixed core, up to the limit of the semi-convective layer. The effect of a variation of overshooting with the temperature gradient is therefore negligible. This is due to the compensation of the layers that keeps the total size of the mixed core almost the same. This contributes to understanding why the shell, and more generally the evolutionary trajectory, is just slightly affected by the variation of overshooting.

Luminosity

To confirm that the overshooting does not significantly affect the star on the point of view of the evolution, the luminosity profile is interesting to examine (Fig. 2.26) . The plateau of shell and core luminosities are similar in both cases, during the evolution. This explains the similar trajectories in the H-R diagram.

Conclusion

In conclusion, the size of the overshooting layer affects the size of the mixed core in early stages and the age appearance of the semi-convective layer. Furthermore, the two layers seem to compensate each other so that the total extension of the mixed core remains almost the same in later stages. This means that the size of the semi-convective layer adapts. The latter affects the chemical composition profile. However, even with a difference of molecular gradient ∇_μ between the pair of stars, the real gradient (temperature gradient) is more or less the same in the entire core, as a consequence of the layers adapting their size to each other. The general structure of the shell and the outer parts is then lightly affected by the variation of overshooting. As a consequence, the trajectories of evolution are similar and the age that marking the exhaustion of central helium remains almost the same. We can conclude that the overshooting does not significantly affect the evolution of a star of reference.

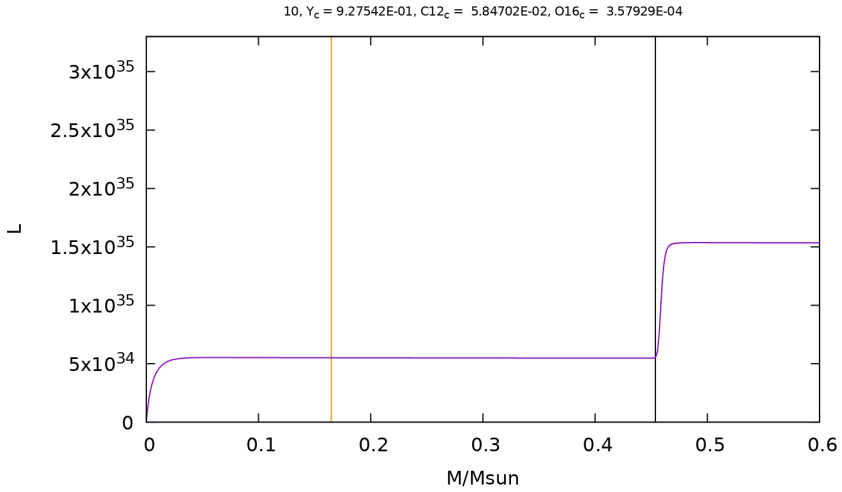

(A) $Y_c = 0.93$, the convective core mass grows.

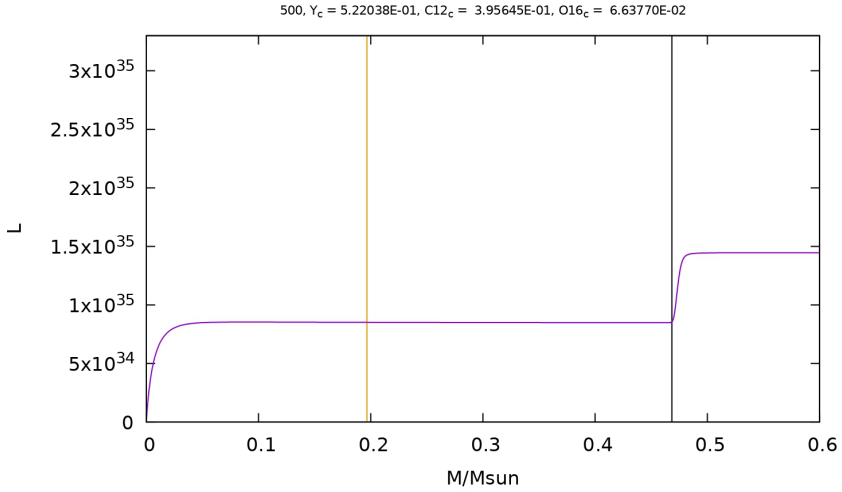

(B) $Y_c = 0.52$.

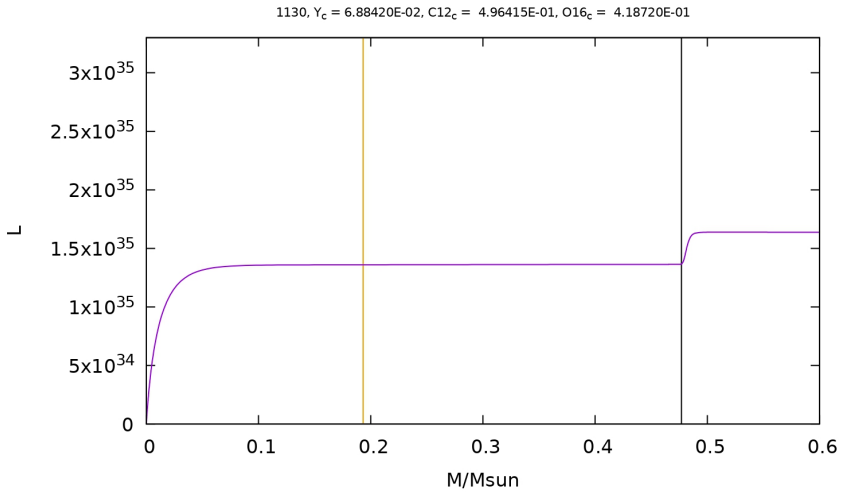

(C) $Y_c = 0.07$, the convective core mass decreases.

FIGURE 2.3: Luminosity profile as a function of the mass ratio $m/M_\odot$ for 1 $M_\odot$. The mixed core boundary (convective + overshooting layer) is the vertical orange line and the shell boundary is the vertical black line. The figure is divided into 3 sub-figures extracted from the whole sequence of evolution.

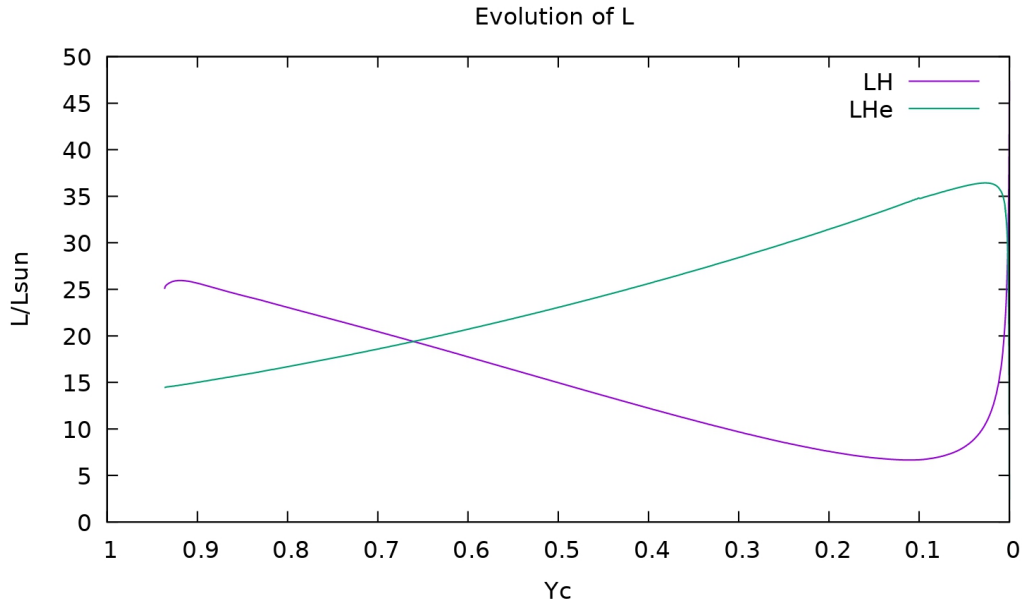

FIGURE 2.4: Luminosity profiles as functions of the mass fraction of central helium for 1 $M_{\odot}$. The shell luminosity is in green and the He-core luminosity in purple.

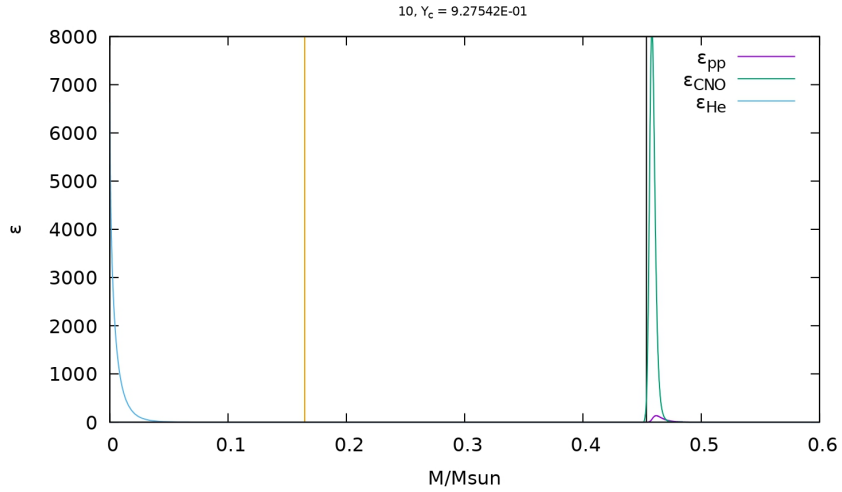

(A) $Y_c = 0.93$, the core mass grows.

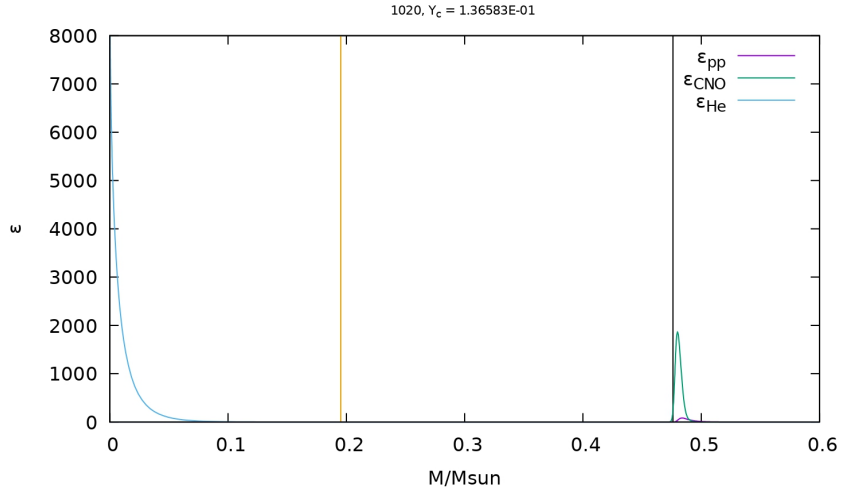

(B) $Y_c = 0.52$, the core is slowing down its expansion.

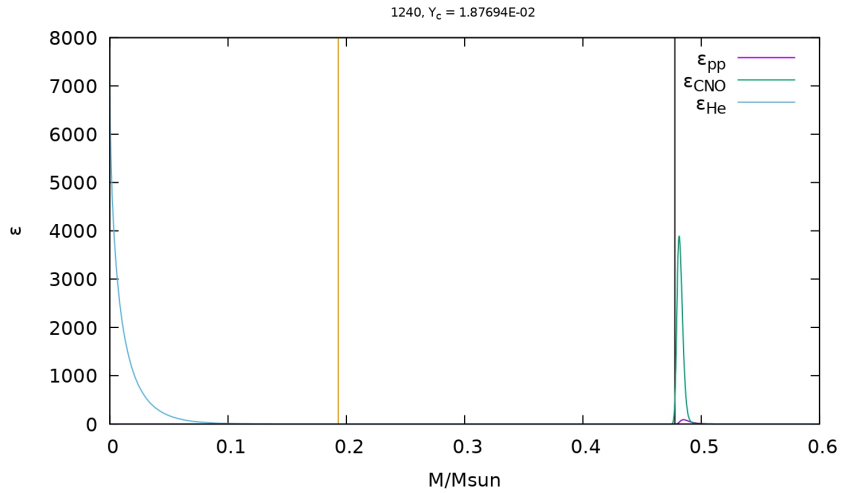

(C) $Y_c = 0.02$, the mixed core retracts and the semi-convective layer disappeared at $Y_c = 0.10$.

FIGURE 2.5: Nuclear rate profiles as functions of the mass ratio $m/M_\odot$ for 1 $M_\odot$. The mixed core boundary (convective + overshooting layer) is the vertical orange line and the shell boundary is the vertical black line. The figure is divided into 3 sub-figures extracted from the whole sequence of evolution.

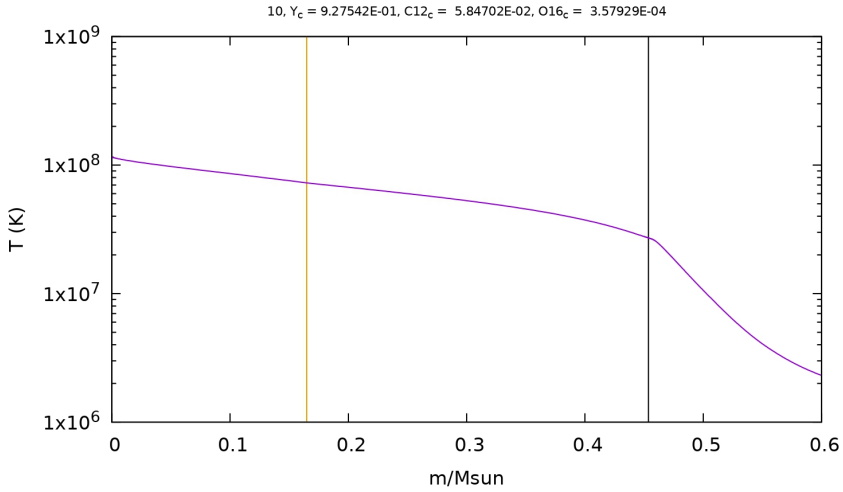

(A) $Y_c = 0.93$, the core mass grows.

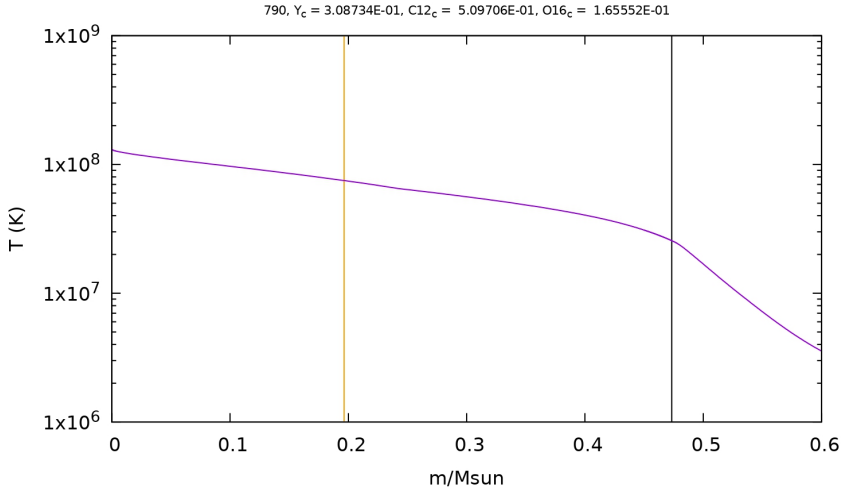

(B) $Y_c = 0.31$, the core is slowing down its expansion.

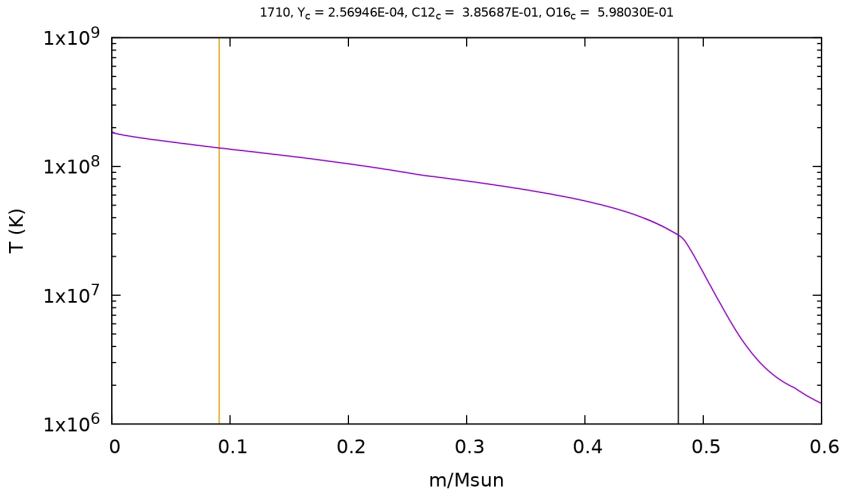

(C) $Y_c = 2.57\ 10^{-04}$, the mixed core retracts. The semi-convective layer disappeared at $Y_c = 0.10$.

FIGURE 2.6: Temperature profile as a function of the mass ratio $m/M_\odot$ for 1 $M_\odot$. The mixed core boundary (convective + overshooting layer) is the vertical orange line and the shell boundary is the vertical black line. The figure is divided into 3 sub-figures extracted from the whole sequence of evolution.

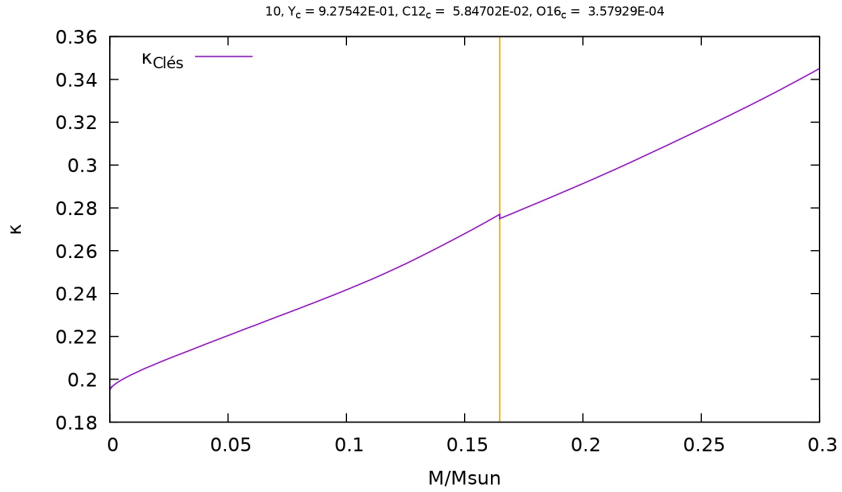

(A) $Y_c = 0.93$, the core mass grows.

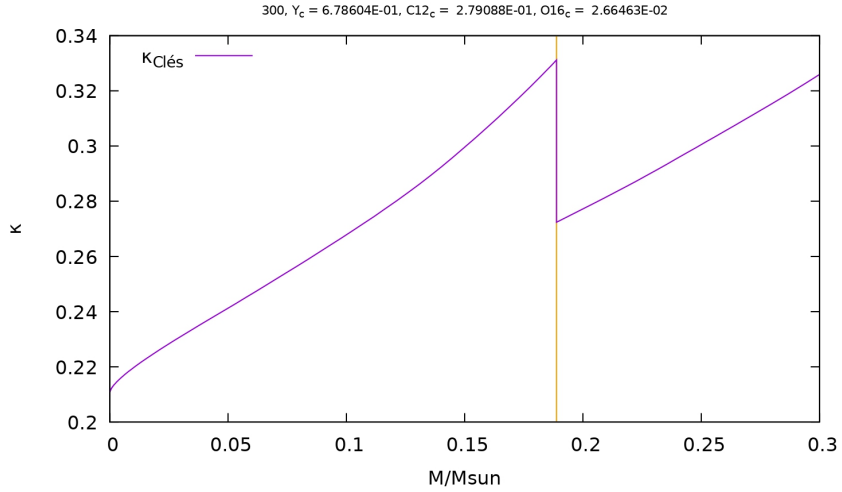

(B) $Y_c = 0.68$

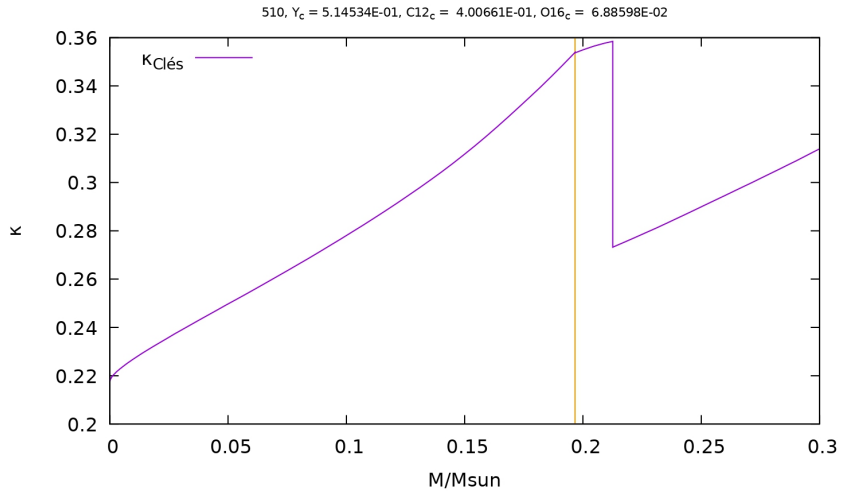

(C) $Y_c = 0.52$, the semi-convective layer expands.

FIGURE 2.7: Opacity profile as a function of the mass ratio $m/M_\odot$ for 1 $M_\odot$. The mixed core boundary (convective + overshooting layer) is the vertical orange line and the shell boundary is the vertical black line. The figure is divided into sub-figures extracted from the sequence of evolution.

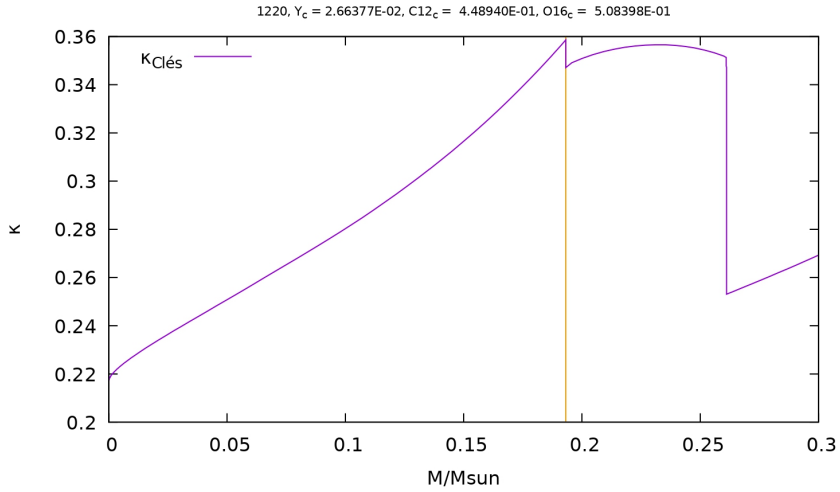

(A) $Y_c = 0.03$.

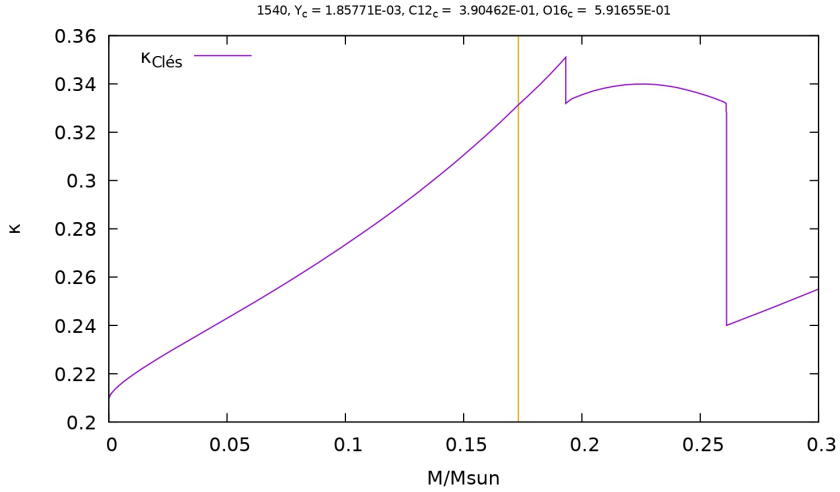

(B) $Y_c = 2\ \ 10^{-3}$, the convective core mass decreases.

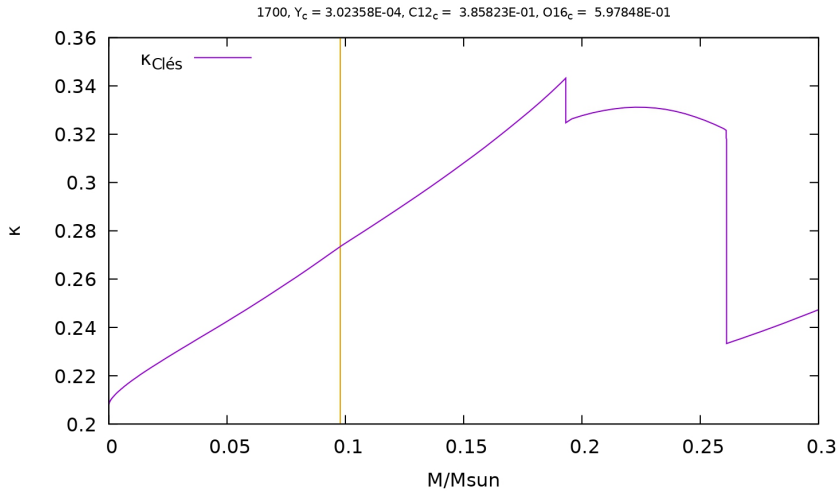

(C) $Y_c = 3.02\ \ 10^{-4}$.

FIGURE 2.8: Opacity profile as a function of the mass ratio $m/M_\odot$ for 1 $M_\odot$. The mixed core boundary (convective + overshooting layer) is the vertical orange line and the shell boundary is the vertical black line. The figure is divided into 3 sub-figures extracted from the whole sequence of evolution.

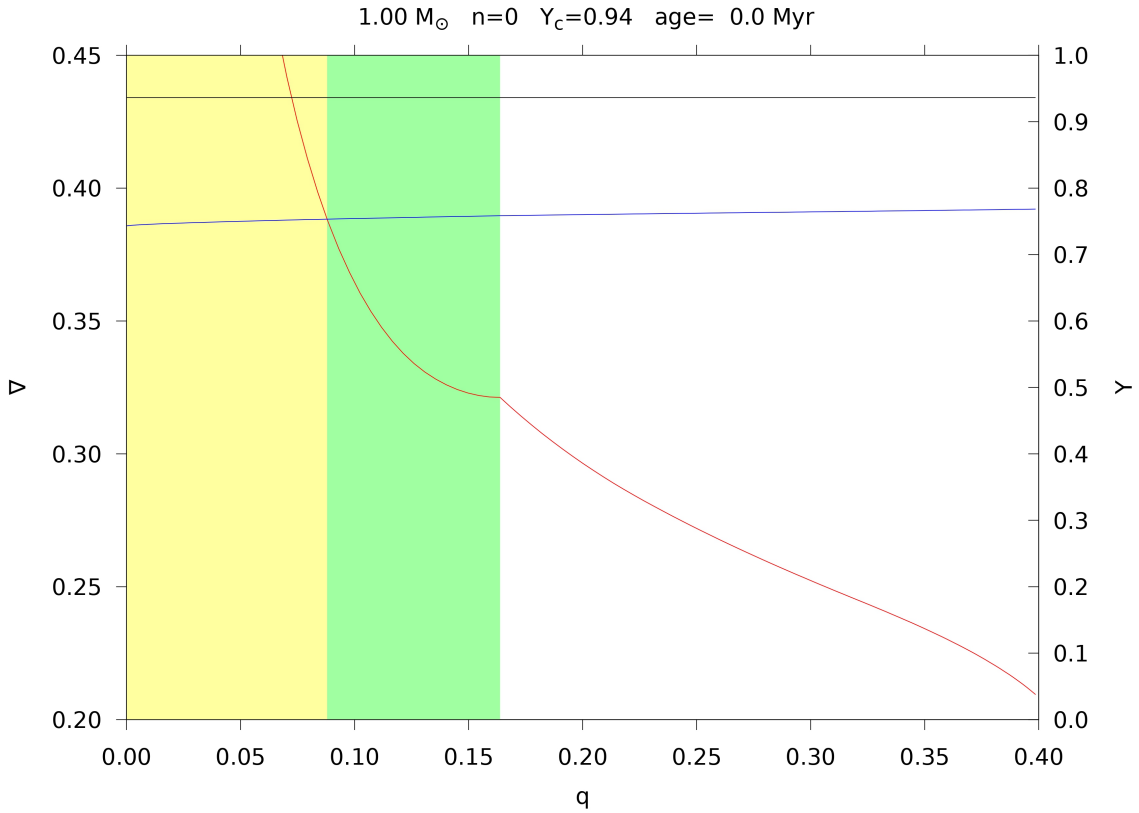

(A) $Y_c = 0.94$

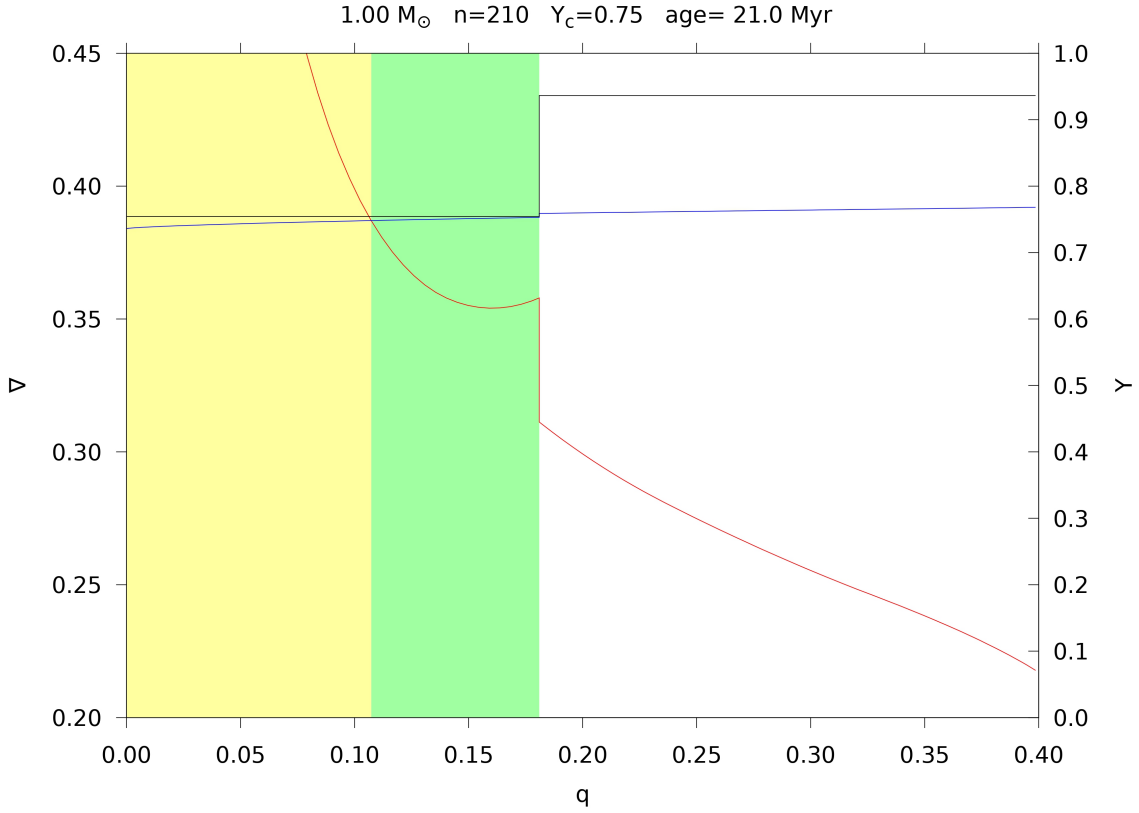

(B) $Y_c = 0.75$

FIGURE 2.9: Gradients profiles and helium mass fraction profile as a function of the mass ratio for 1 $M_\odot$. The convective zone is in yellow, the overshooting layer in green and the semi-convective zone in light blue. The radiative gradient ∇_{rad} is in red and the adiabatic gradient ∇_{ad} in blue. For the real gradient ∇, $\nabla = \nabla_{ad}$ in the mixed core and $\nabla = \nabla_{rad}$ in the radiative zone. The figure is divided into sub-figures extracted from the sequence of evolution.

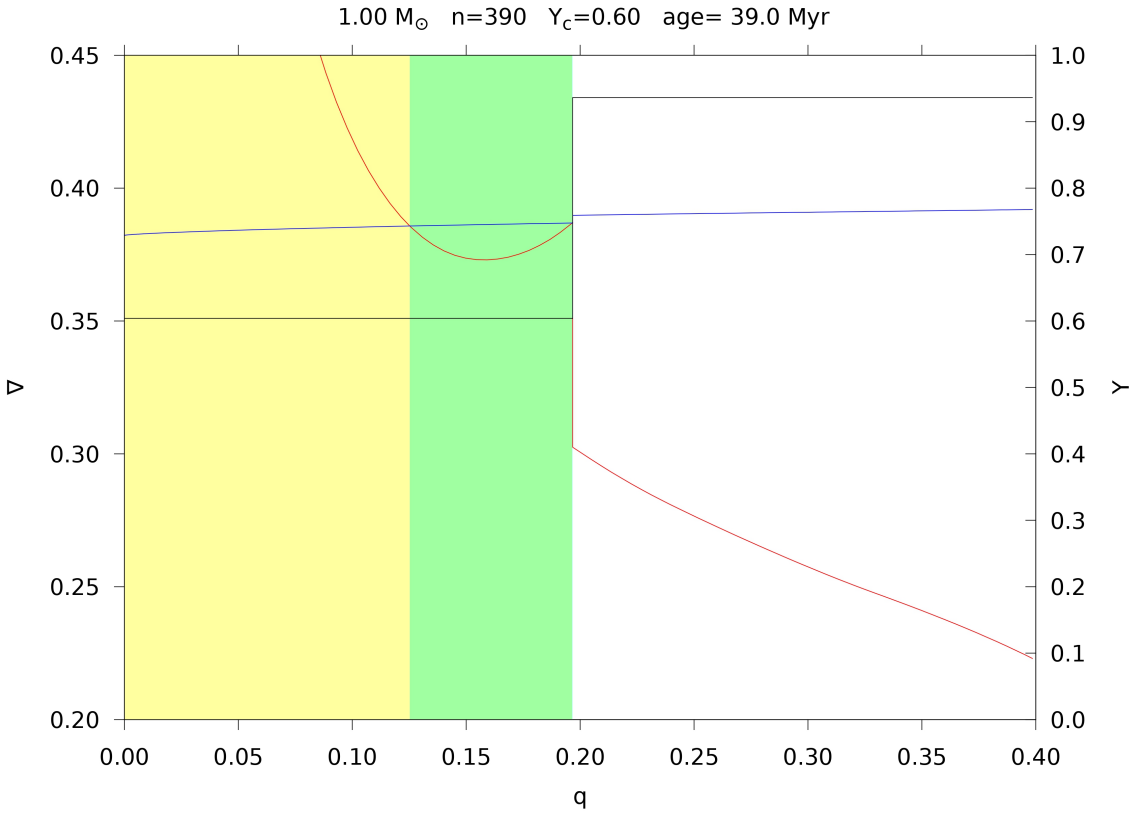

(A) $Y_c = 0.60$

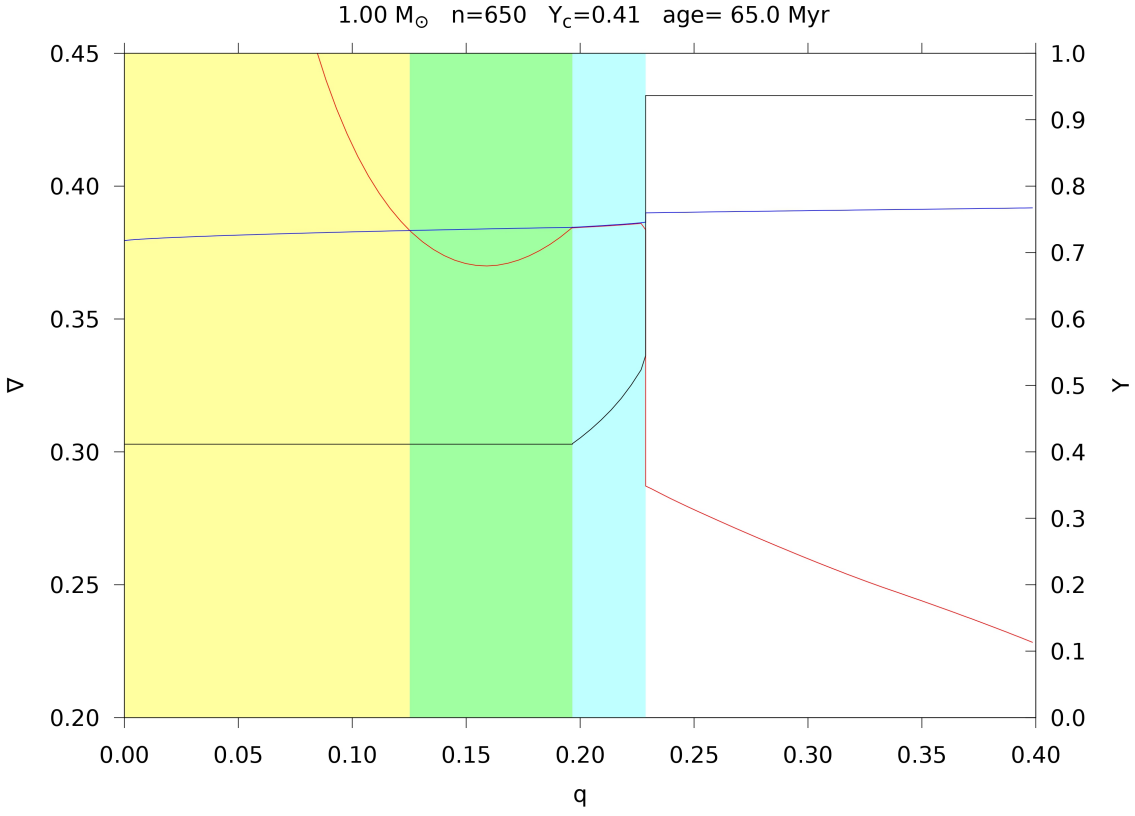

(B) $Y_c = 0.41$

FIGURE 2.10: Gradients profiles and helium mass fraction profile as a function of the mass ratio for 1 $M_\odot$. The convective zone is in yellow, the overshooting layer in green and the semi-convective zone in light blue. The radiative gradient ∇_{rad} is in red and the adiabatic gradient ∇_{ad} in blue. For the real gradient ∇, $\nabla = \nabla_{ad}$ in the mixed core and $\nabla = \nabla_{rad}$ in the radiative zone. The figure is divided into sub-figures extracted from the sequence of evolution.

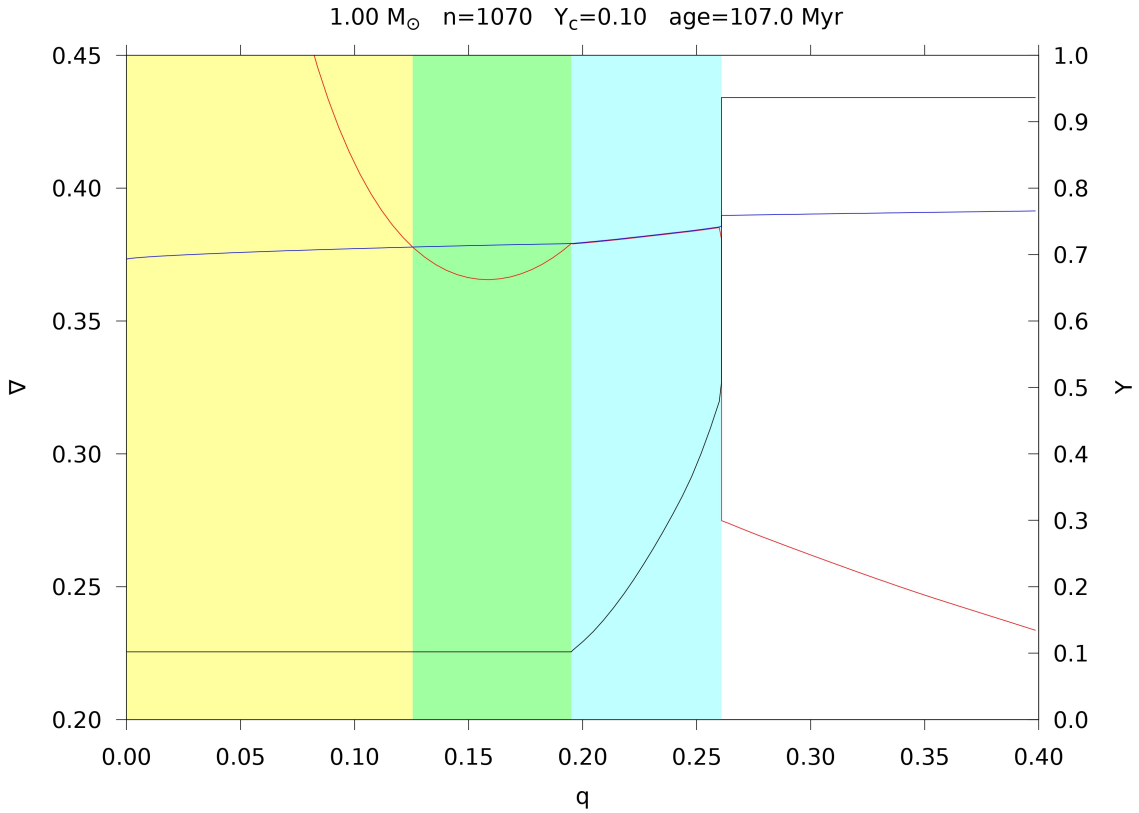

(A) $Y_c = 0.10$

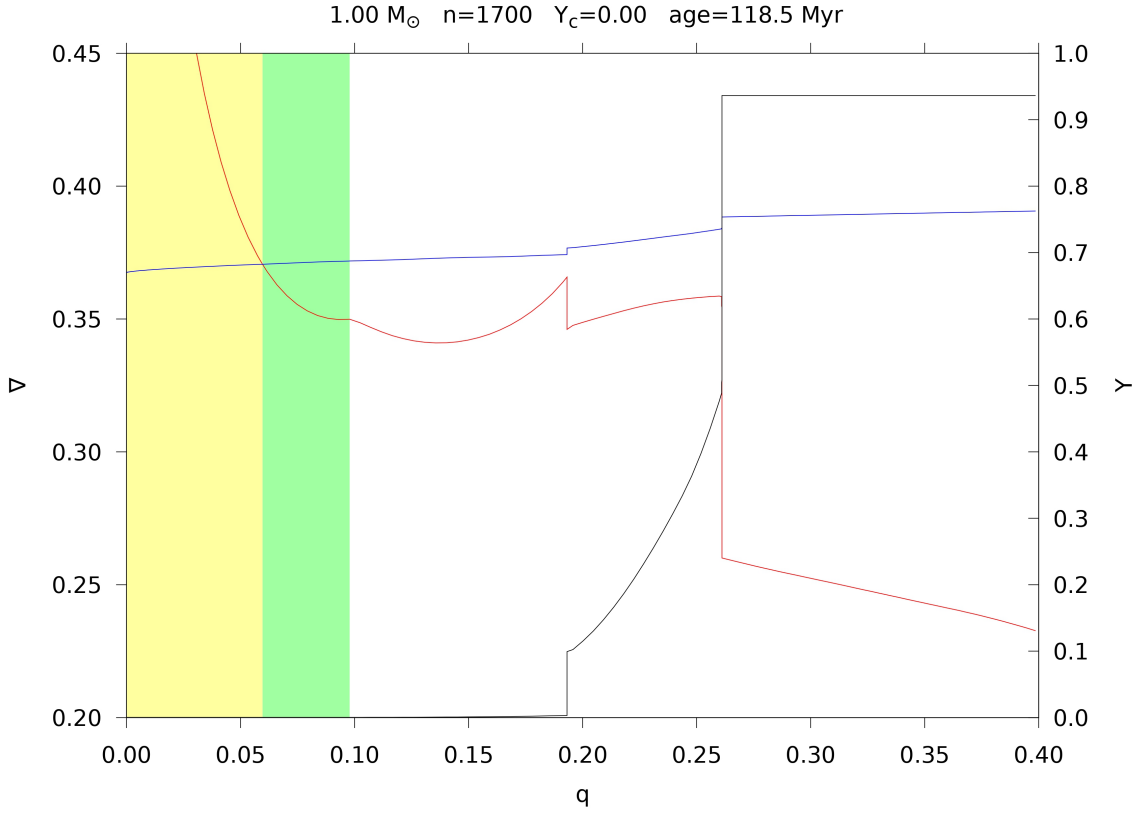

(B) $Y_c = 0$

FIGURE 2.11: Gradients profiles and helium mass fraction profile as a function of the mass ratio for 1 $M_\odot$. The convective zone is in yellow, the overshooting layer in green and the semi-convective zone in light blue. The radiative gradient ∇_{rad} is in red and the adiabatic gradient ∇_{ad} in blue. For the real gradient ∇, $\nabla = \nabla_{ad}$ in the mixed core and $\nabla = \nabla_{rad}$ in the radiative zone. The figure is divided into sub-figures extracted from the sequence of evolution.

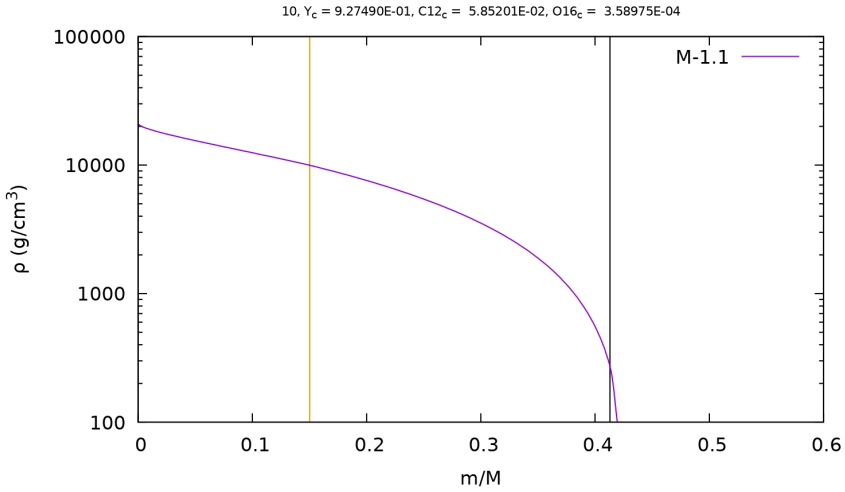

(A) $Y_c = 0.93$

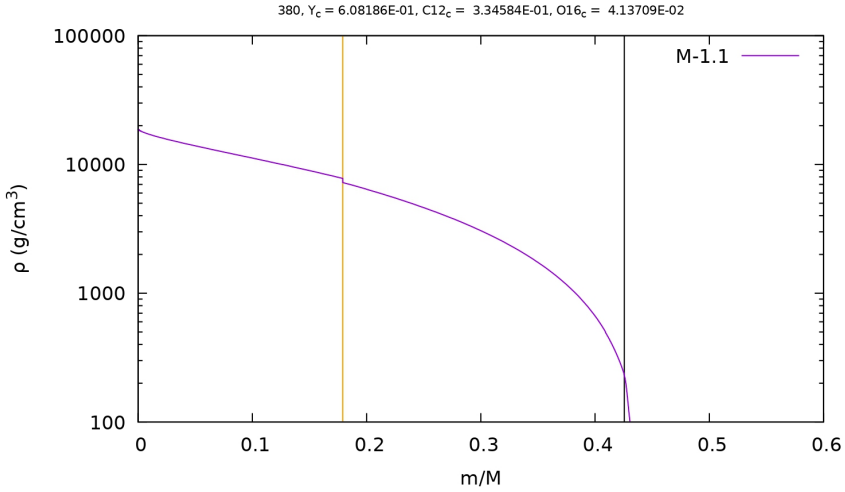

(B) $Y_c = 0.61$

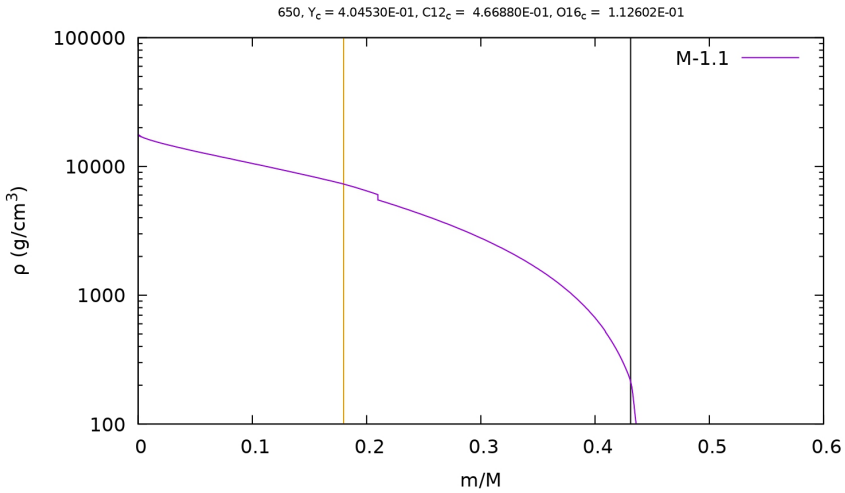

(C) $Y_c = 0.40$

FIGURE 2.12: Density profile as a function of the mass ratio $m/M_\odot$ for $1M_\odot$. The mixed core boundary (convective + overshooting layer) is the vertical orange line and the shell boundary is the vertical black line. The figure is divided into sub-figures extracted from the sequence of evolution.

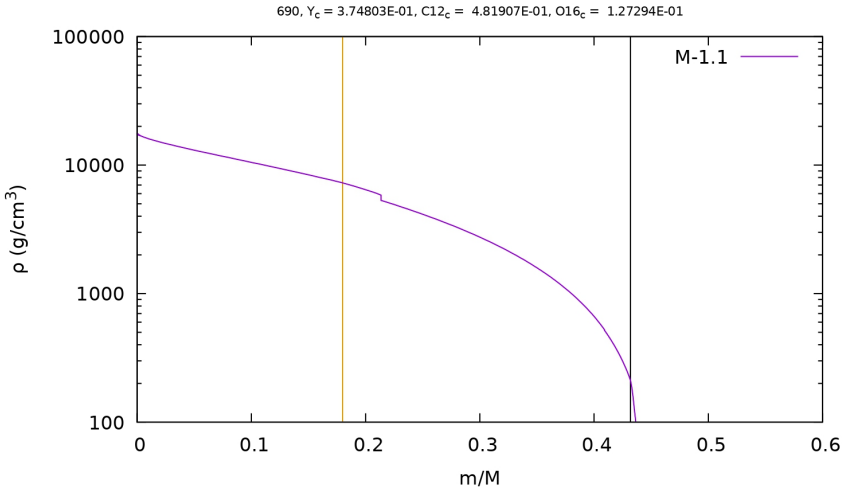

(A) $Y_c = 0.37$

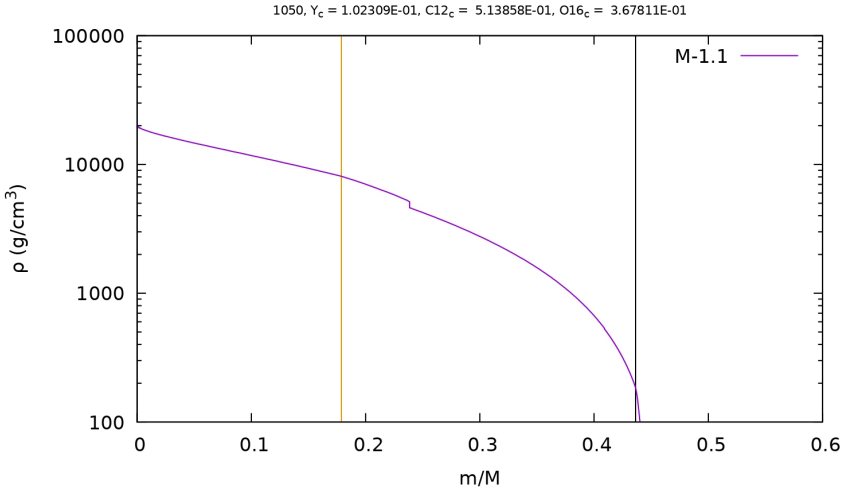

(B) $Y_c = 0.10$

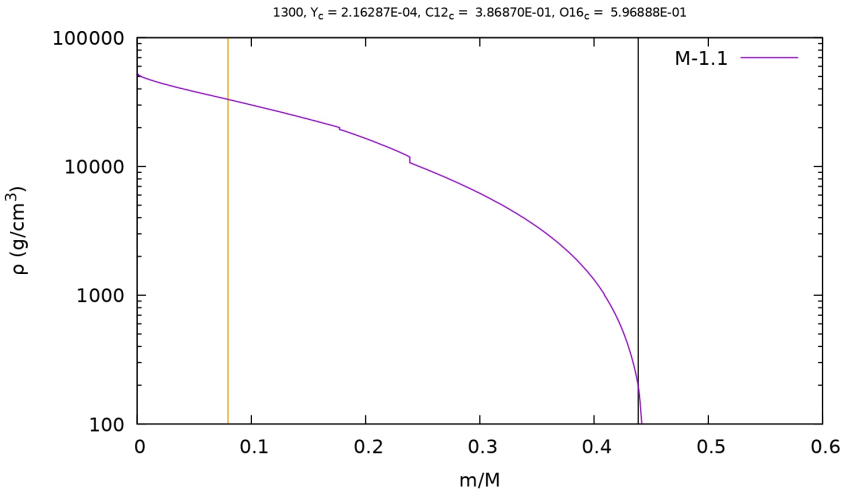

(C) $Y_c = 2.16\ 10^{-4}$

FIGURE 2.13: Density profile as a function of the mass ratio $m/M_\odot$ for $1M_\odot$. The mixed core boundary (convective + overshooting layer) is the vertical orange line and the shell boundary is the vertical black line. The figure is divided into sub-figures extracted from the sequence of evolution.

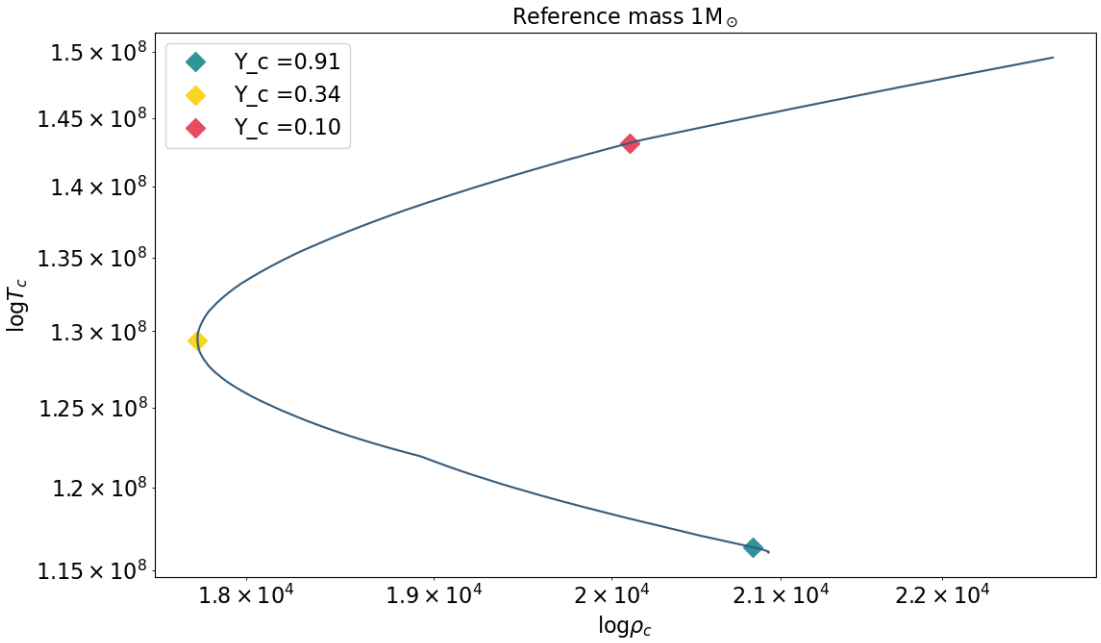

FIGURE 2.14: Central temperature as a function of the central density for the whole sequence of evolution of $1M_{\odot}$. The markers highlight the state of evolution $Y_c = (0.91,0.34,0.10)$.

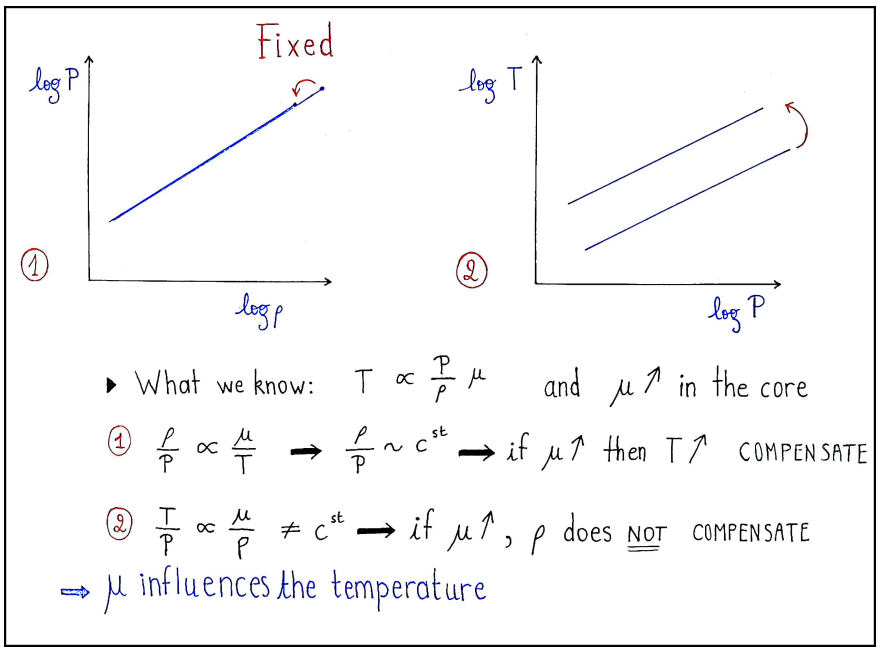

FIGURE 2.15: Schematic illustration of the logarithmic relation T-P and P-ρ.

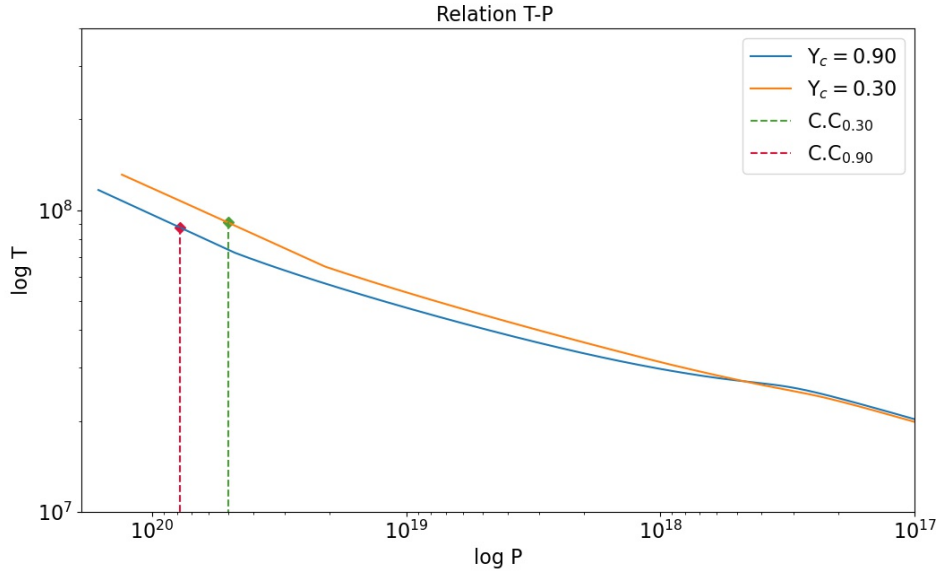

FIGURE 2.16: Log-Log profile of Temperature as a function of Pressure for $1M_\odot$ in the states Y_c=(0.90, 0.30). The x-axis has been reversed to represent the centre of the star (high pressure) on the left and the surface (low pressure) on the right. The vertical lines indicate the Schwarzschild limit of the convective core in both models.

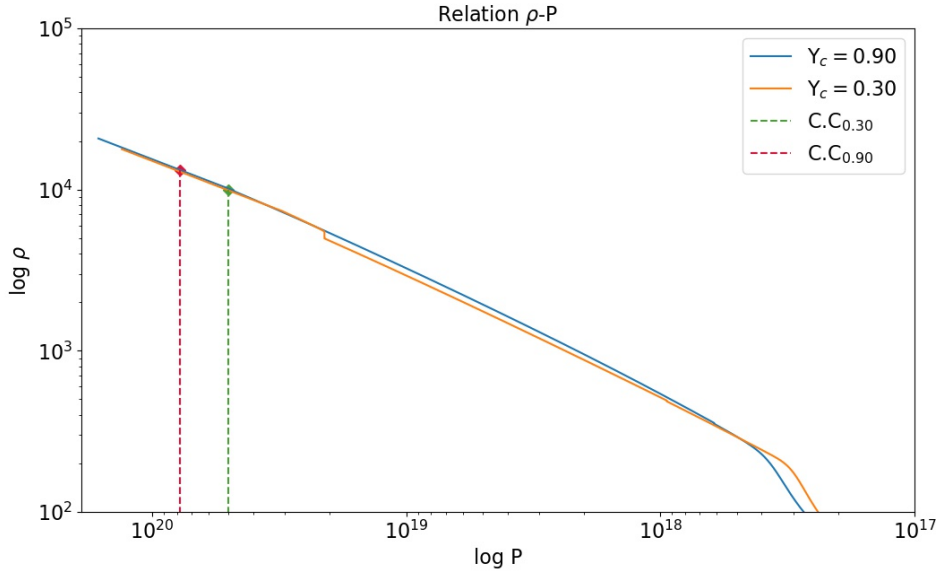

FIGURE 2.17: Log-Log profile of Pressure as a function of Density for $1M_\odot$ in the states Y_c=(0.90, 0.30). The x-axis has been reversed to represent the centre of the star (high pressure) on the left and the surface (low pressure) on the right. The vertical lines indicate the Schwarzschild limit of the convective core in both models.

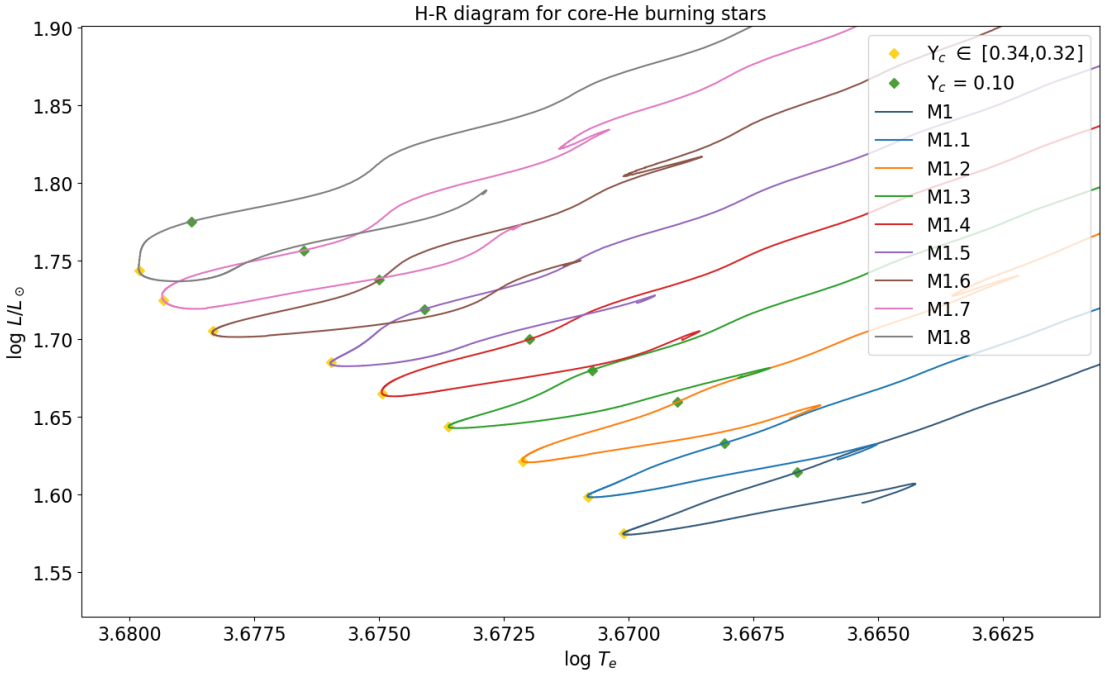

FIGURE 2.18: H-R diagram from 1 $M_\odot$ to 1.8 $M_\odot$ low mass core-He burning star. The markers indicate a state of central helium abundance ($Y_c \in [0.34,0.32]$ in yellow and $Y_c = 0.10$ in green)

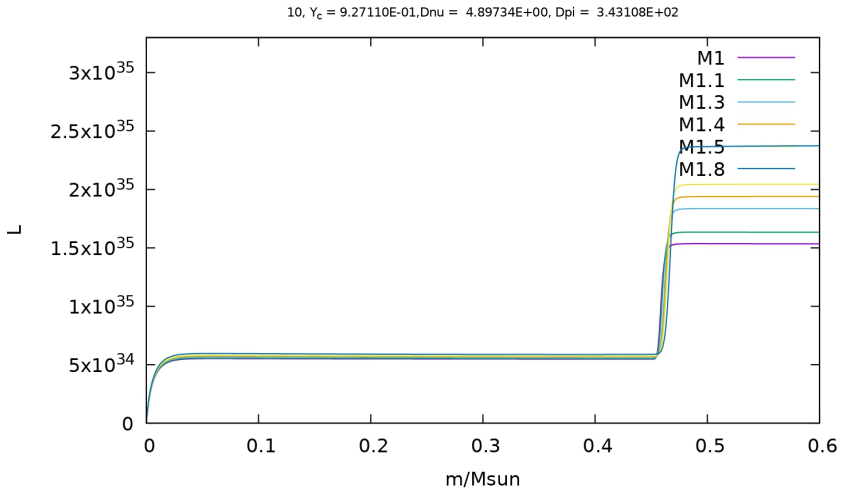

(A) Age= 1 Myr.

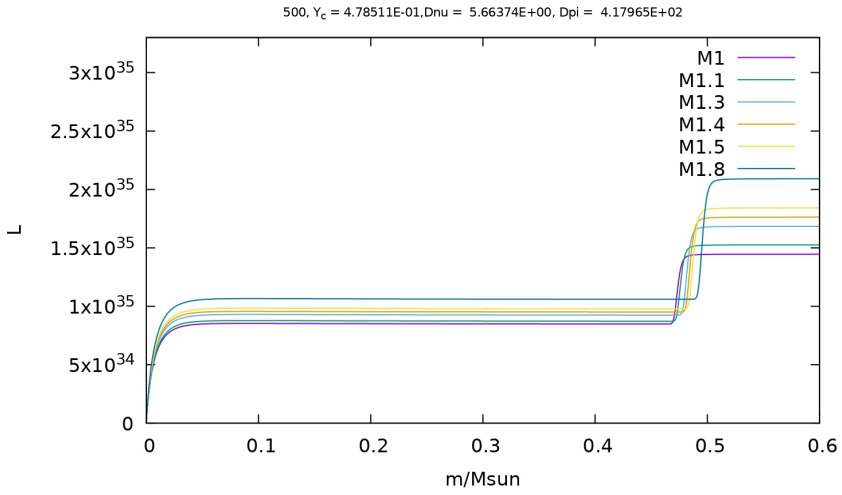

(B) Age= 50 Myr.

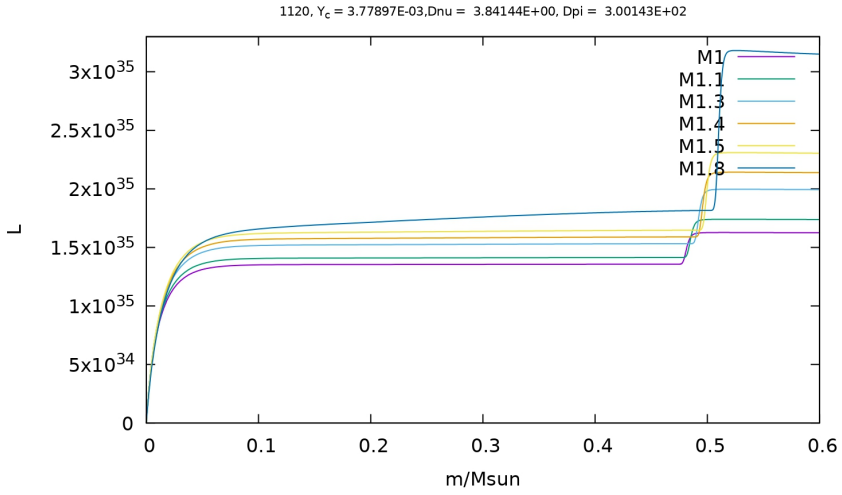

(C) Age= 109.6 Myr. The whole core is contracting in all stars.

FIGURE 2.19: Luminosity profiles as functions of the mass ratio $m/M_{\odot}$ for 1 $M_{\odot}$ to 1.8 $M_{\odot}$. The change of plateau come from the boundary of the shell for each mass.

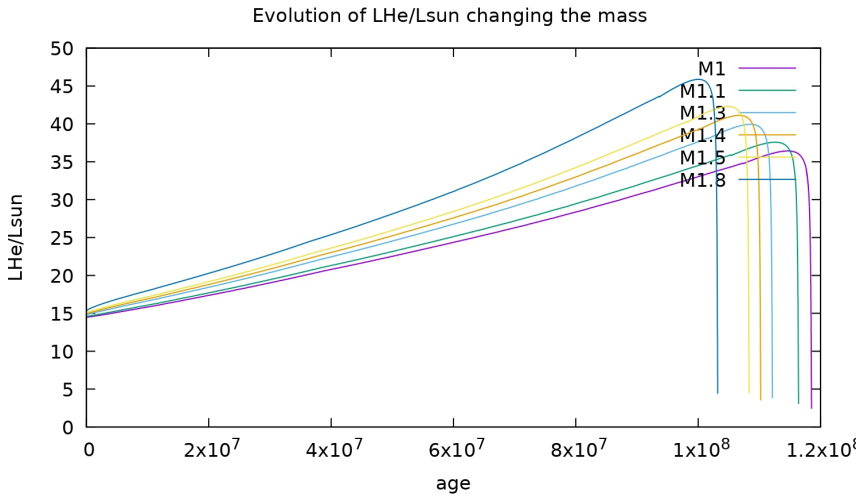

(A) Power produced by helium burning as a function of the **age** (Myr) for a set of stars from 1 $M_\odot$ to 1.8 $M_\odot$

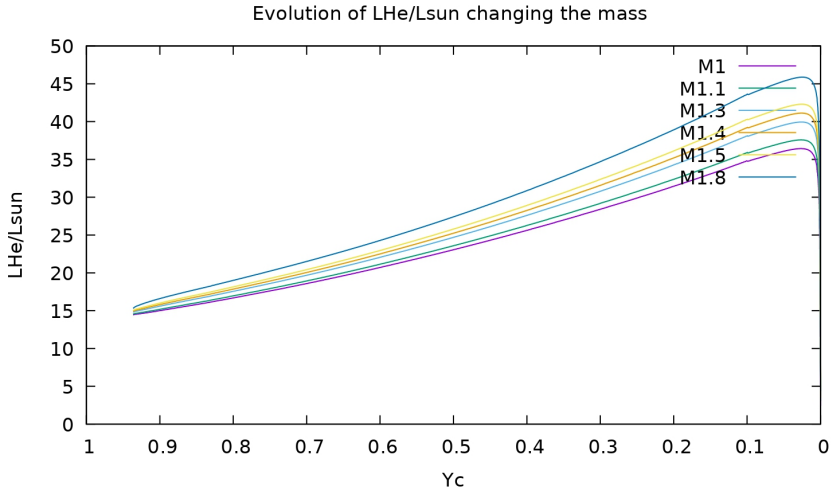

(B) Power produced by helium burning as a function of the **central helium abundance** for a set of stars from 1 $M_\odot$ to 1.8 $M_\odot$

FIGURE 2.20: Power produced by core helium burning (in solar luminosity units) for 1 $M_\odot$ to 1.8 $M_\odot$. The first panel shows profiles as functions of the age in the sequence of evolution and the second panel as a function of the helium central abundance Y_c.

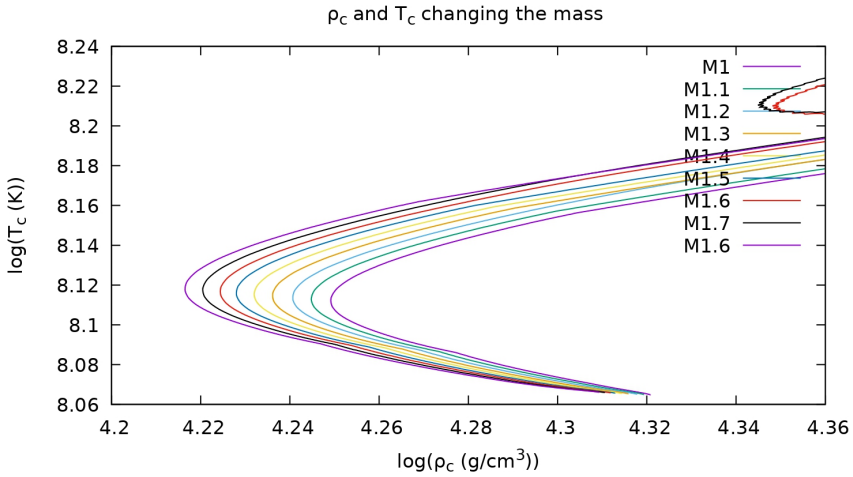

FIGURE 2.21: Central temperature as a function of the central density for the sequence of evolution, for 1 $M_\odot$ to 1.8 $M_\odot$. The bifurcations lie in the range of central helium abundance [0.34-0.32].

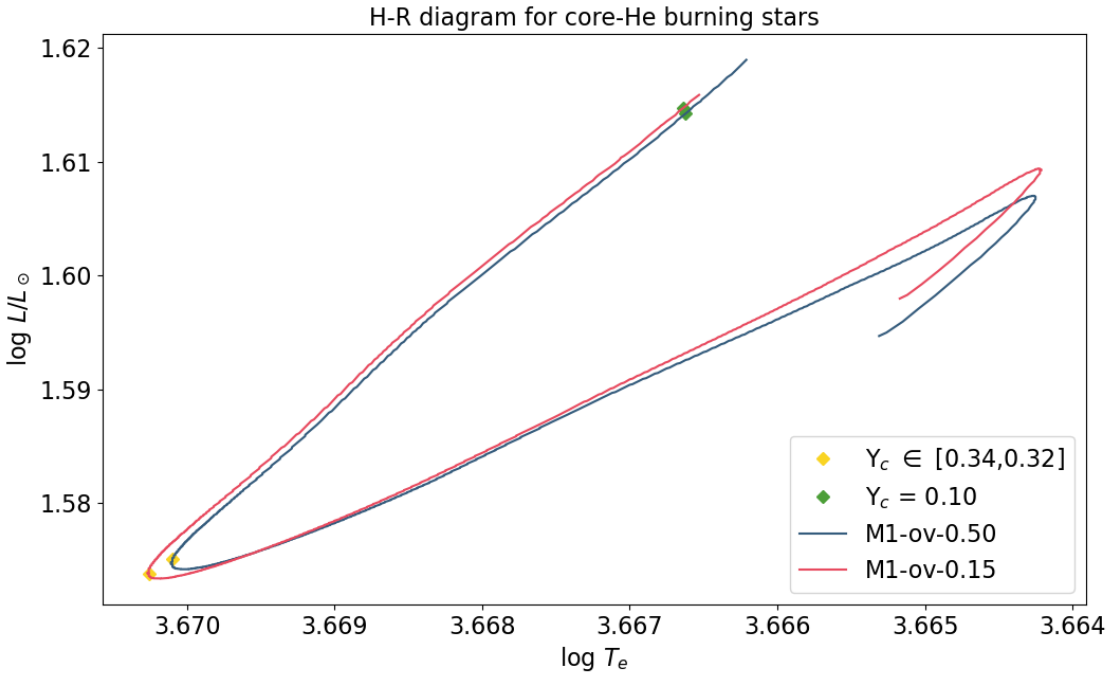

FIGURE 2.22: H-R diagram for 1 $M_\odot$, $\alpha_{over} = (0.50, 0.15)$. The markers indicate a state of central helium abundance ($Y_c \in$ [0.34,0.32] in yellow and $Y_c = 0.10$ in green)

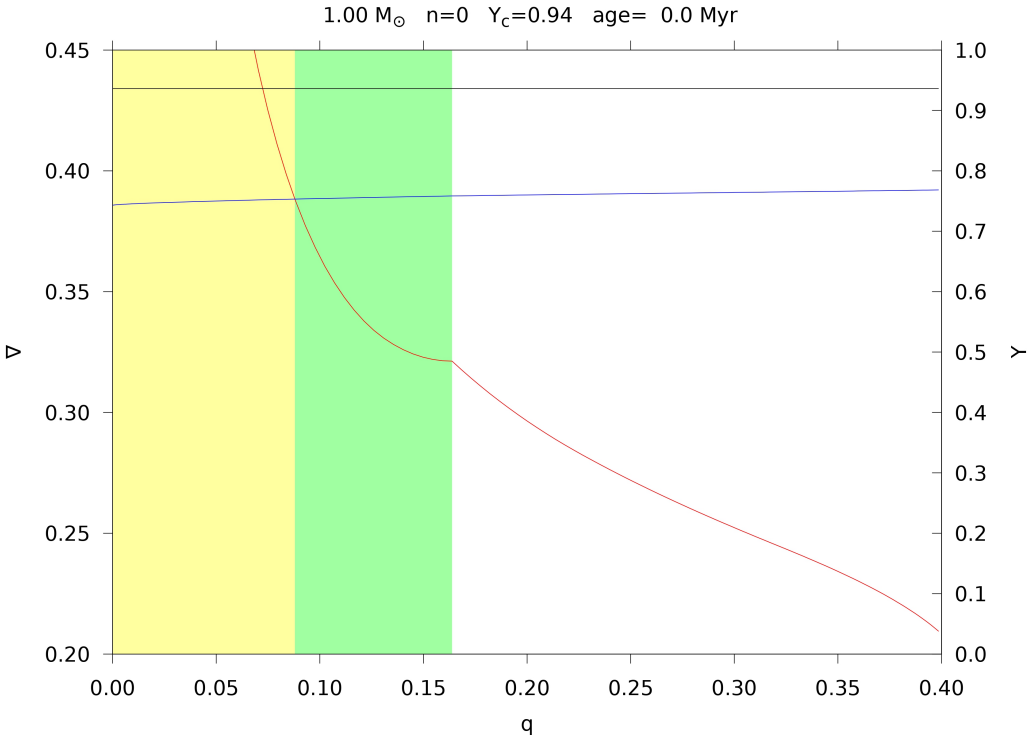

(A) Gradients and helium profiles for $\alpha_{ov} = 0.50$ and the state $Y_c = 0.94$.

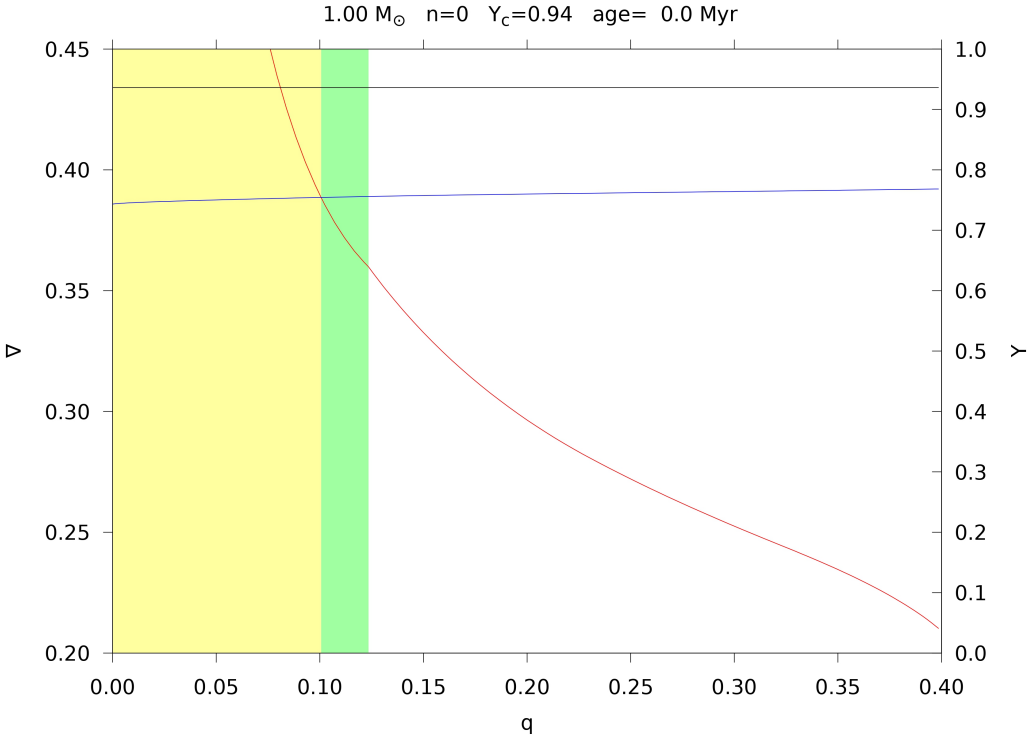

(B) Gradients and helium profiles for $\alpha_{ov} = 0.15$ and the state $Y_c = 0.94$.

FIGURE 2.23: Gradients profiles and helium mass fraction profile as a function of the mass ratio at the age = 0 Myr for $1M_{\odot}$. The convective zone is in yellow, the overshooting layer in green and the semi-convective zone in light blue. The radiative gradient ∇_{rad} is in red and the adiabatic gradient ∇_{ad} in blue. For the real gradient ∇: $\nabla = \nabla_{ad}$ in the mixed core and $\nabla = \nabla_{rad}$ in the radiative zone.

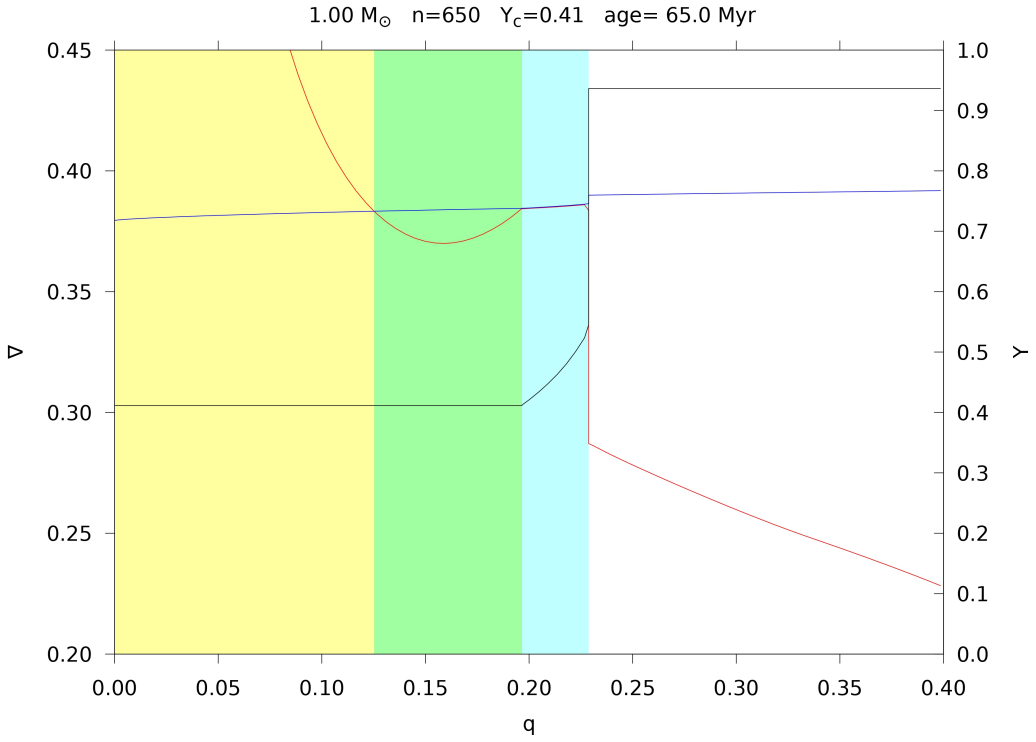

(A) Gradient and helium profiles for $\alpha_{ov} = 0.50$and the state $Y_c = 0.41$.

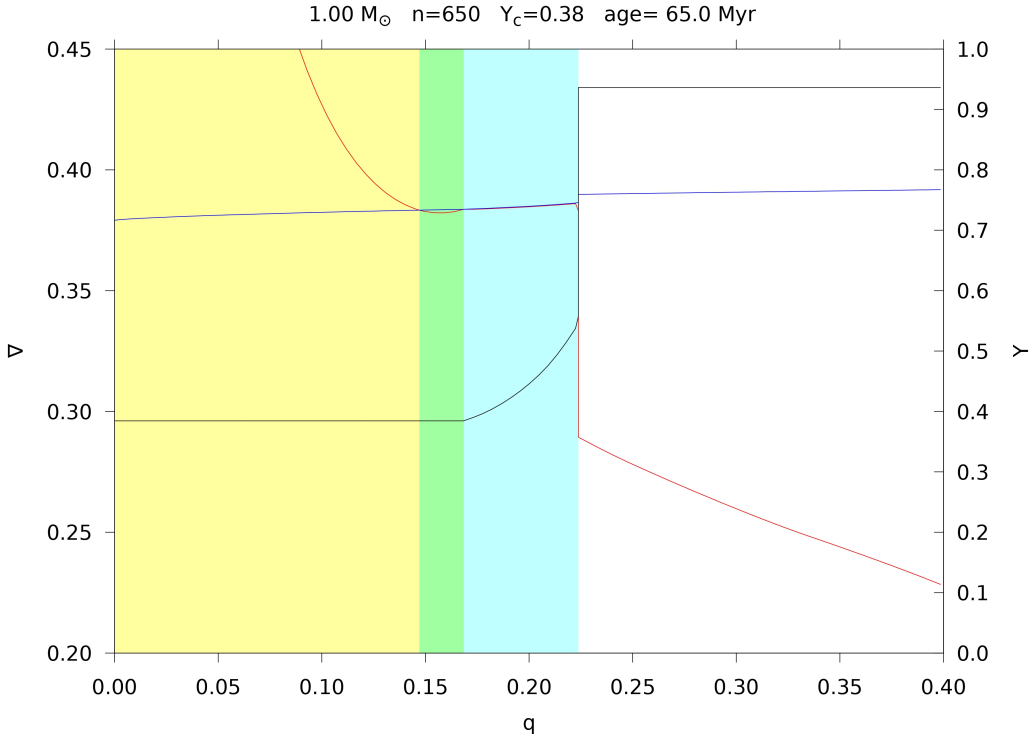

(B) Gradients and helium profiles for $\alpha_{ov} = 0.15$ and the state $Y_c = 0.38$.

FIGURE 2.24: Gradients and helium mass fraction profiles as a function of the mass ratio at the age = 65 Myr for $1M_\odot$. The convective zone is in yellow, the overshooting layer in green and the semi-convective zone in light blue. The radiative gradient ∇_{rad} is in red and the adiabatic gradient ∇_{ad} in blue. For the real gradient ∇: $\nabla = \nabla_{ad}$ in the mixed core and $\nabla = \nabla_{rad}$ in the radiative zone.

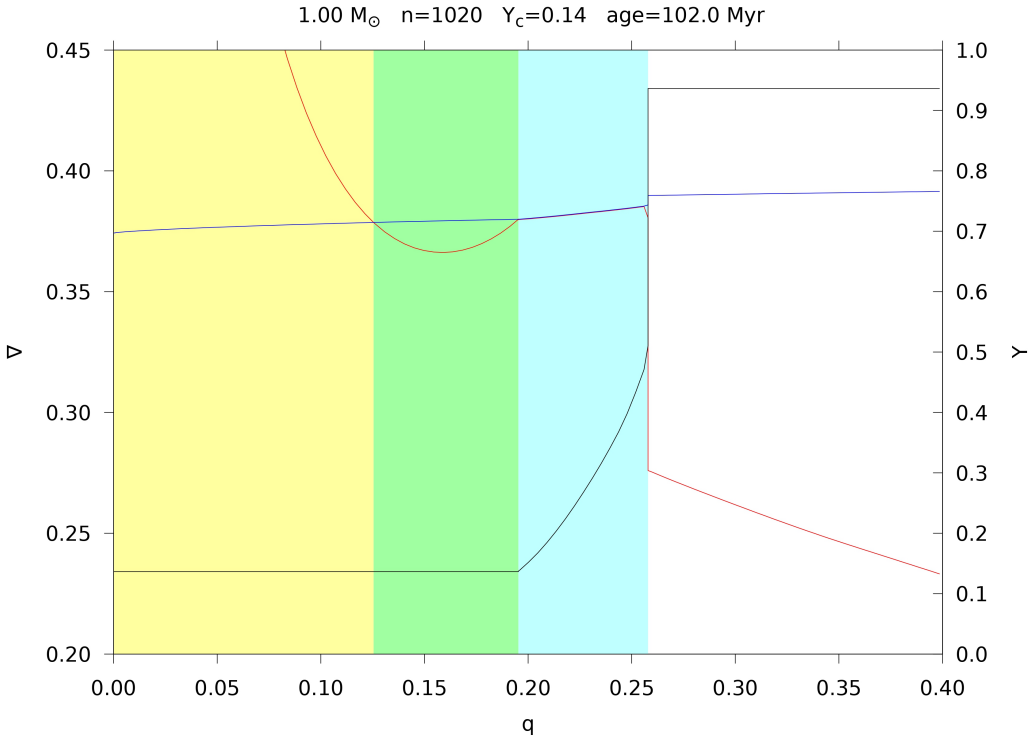

(A) Gradients and helium profiles for $\alpha_{ov} = 0.50$ and the state $Y_c = 0.14$.

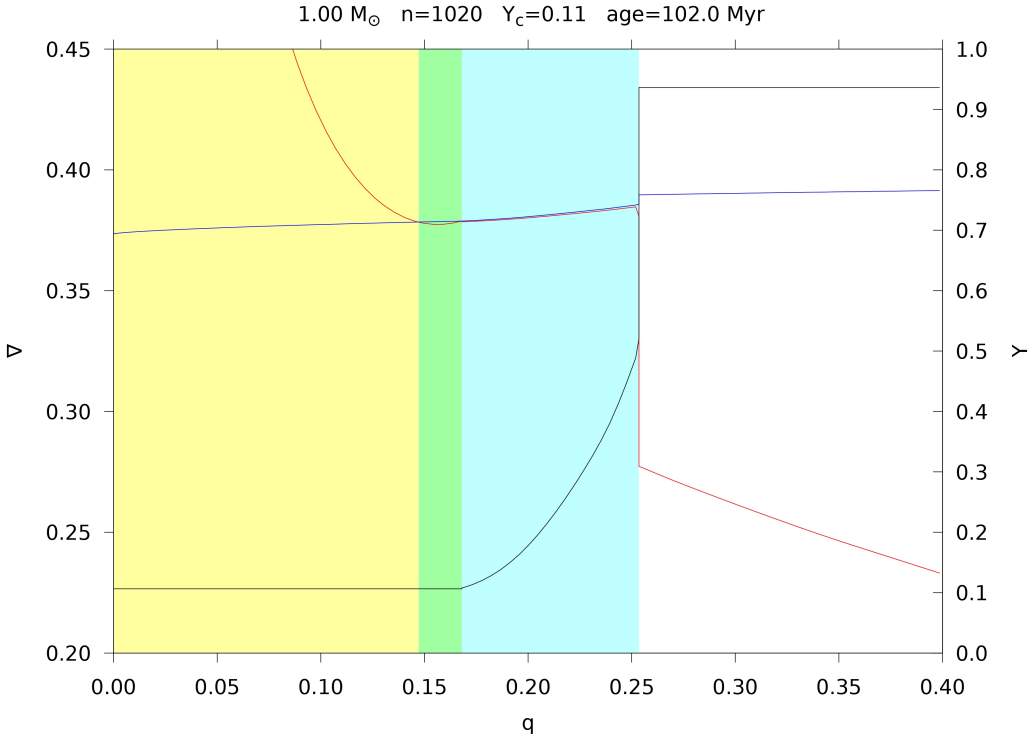

(B) Gradients and helium profiles for $\alpha_{ov} = 0.15$ and the state $Y_c = 0.11$.

FIGURE 2.25: Gradients profiles and helium mass fraction profile as a function of the mass ratio at the age = 102 Myr for $1M_\odot$. The convective zone is in yellow, the overshooting layer in green and the semi-convective zone in light blue. The radiative gradient ∇_{rad} is in red and the adiabatic gradient ∇_{ad} in blue. For the real gradient ∇: $\nabla = \nabla_{ad}$ in the mixed core and $\nabla = \nabla_{rad}$ in the radiative zone.

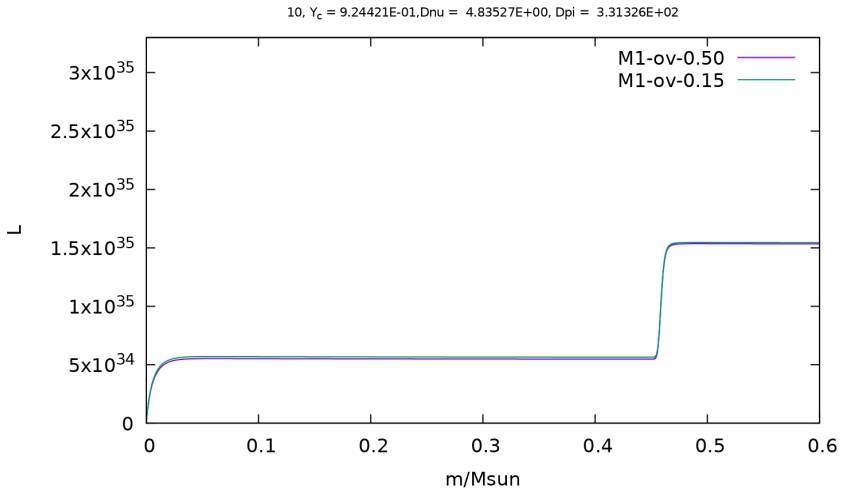

(A) Age= 1 Myr.

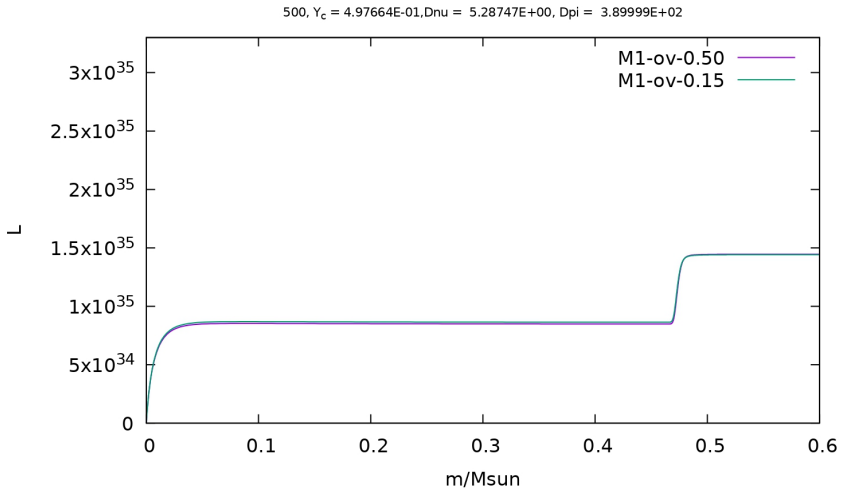

(B) Age= 50 Myr.

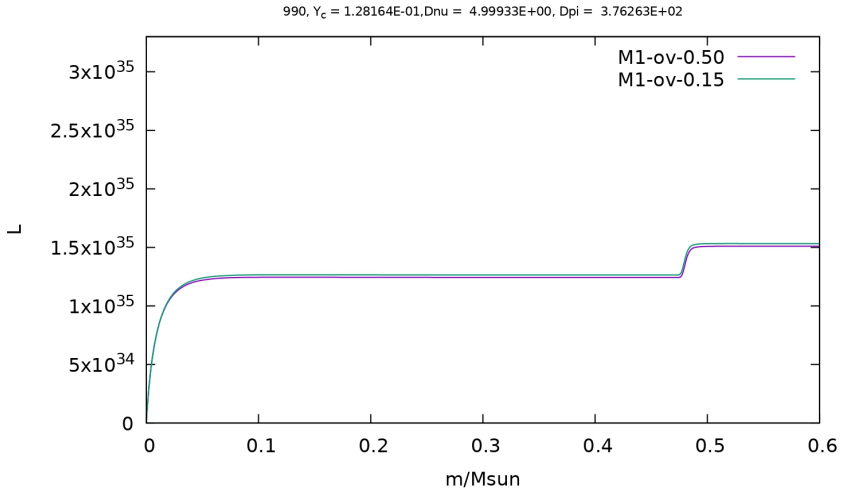

(C) Age= 99 Myr.

FIGURE 2.26: Luminosity profiles as functions of the mass ratio $m/M_{\odot}$ for 1 $M_{\odot}$, $\alpha_{over} = (0.50, 0.15)$. The change of plateau comes from the transition core-shell for each overshooting.

Chapter 3

Polytropes Model

3.1 Introduction

In the previous chapter, we observed the trend of various physical parameters throughout the evolution. In order to provide a complement to the physical and mathematical understanding of the observed profiles, we rely on a simplified model, the polytropes.

The link between pressure and density inside the convective core of a star was highlighted in Chapter 2. More precisely, the logarithmic relation between these parameters seemed to follow a straight line with a fixed slope ($lnP \sim \gamma\ ln\rho + cst$). The polytropes approximation provides a power law relation between ρ and P, which is consistent with the observation. This framework contains simple analytical expressions to quantify the convective core physical parameters and by extension, allows to study the increase of the radiative gradient below the hydrogen shell in core-He burning stars. In this Chapter, we explore the application of the model, including its derivation, relevance, and limitations.

3.2 Theoretical and Mathematical Aspects

3.2.1 Polytropes

The polytropes model assumes a power law relation between pressure and density as follows

$$P = K\rho^{\gamma} = K\rho^{1+1/n}, \tag{3.1}$$

with $\gamma = \frac{n+1}{n}$.

The power n refers to the *polytropic index* and K is a constant. To model a convective core, the index, n, is constant and usually around 1.5 as it is confirmed with the results.

3.2.2 Lane-Emden Equation

The polytropes model is related to the so-called Lane-Emden solutions. These solutions are derived from the Lane-Emden equation. The expression is obtained by combining the equations of continuity, hydrostatic equilibrium and using the polytropes relation between P and ρ. With a change of variables, we obtain the 2^{nd}-order differential equation, **Lane-Emden**:

$$\frac{1}{z^2}\frac{d}{dz}\left(z^2\frac{dw}{dz}\right) + w^n = 0, \tag{3.2}$$

where the solutions $w(z)$, expressed in terms of the variable z, are defined as

$$z = Ar \quad , \quad w = \frac{\phi}{\phi_c} = \left(\frac{\rho}{\rho_c}\right)^{1/n} , \tag{3.3}$$

$$A = \frac{4\pi G}{(n+1)K} \rho_c^{\frac{n-1}{2n}} . \tag{3.4}$$

The central conditions of the problem are the following:

$$w(0) = 1 \quad , \quad dw/dz(0) = 0.$$

For the purpose of the numerical resolution, we assume that the solutions $w(z)$ can be expanded as a power series near the central point z=0 to avoid the singularity "$\frac{1}{0}$". The power is even as the Lane-Emden equation is invariant under the transformation $z \to -z$ (Roxburgh and Stockman, 1999).

$$w_n(z) = \sum_{k=0}^{\infty} a_k z^{2k}, \quad w^n = \sum_{k=0}^{\infty} b_k z^{2k}, \quad a_0 = b_0 = 1$$

We inject these solutions into equation 3.2. By comparing the polynomials of the same order, the missing coefficients are obtained . Therefore, we obtain an expression of $w(z)$ for the singularity $z = 0$. The numerical resolution is described in Section 3.3 and Figure 3.1 shows the results plotted for a diverse set of polytropic indices.

$$w_n = 1 - \frac{1}{6}z^2 + \frac{n}{120}z^4 - \frac{n(8n-5)}{15120}z^6 + \frac{n\left(122n^2 - 183n + 70\right)}{3265920}z^8 + \dots \tag{3.5}$$

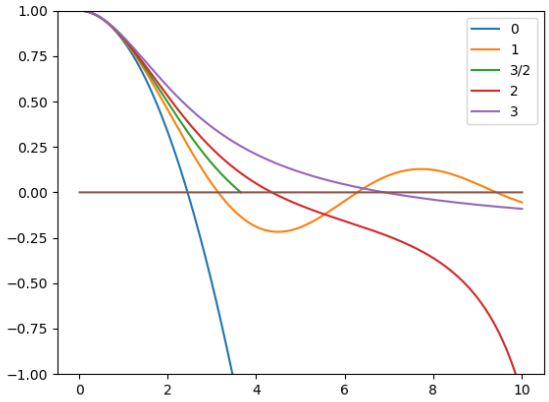

FIGURE 3.1: Lane-Emden solutions in terms of the variable z for index n ∈ (0 , 1 , 3/2 , 2 , 3).

3.2.3 Physical Parameters Equations

The physical parameters describing the stellar interior (such as temperature, density, pressure,etc.) can be expressed mathematically in terms of Lane-Emden solutions since the latter are related to density by definition (Eq.3.3). To simplify the computation, the derivation of the analytical expressions is expressed with the logarithmic

function.

Density

From the definition of the solution $w(z)$ (Eq. 3.3) and by taking the logarithm, the density equation is as follows.

$$\ln \rho(z) = \ln \rho_c + n \ln w(z) \tag{3.6}$$

Pressure

The pressure logarithmic equation comes from the polytropic relation (Eq. 3.1). This describes a straight line with the coefficients (n, K, γ).

$$\ln P(z) = \gamma \ln \rho + \ln K \tag{3.7}$$
$$= \gamma \ln \rho_c + \gamma n \ln w(z) + \ln K \tag{3.8}$$

Temperature

We start with the ideal gas law,

$$P = \frac{k_B \rho T}{\mu m_u} \Leftrightarrow T = \frac{P}{\rho} \mu \frac{m_u}{k_B},$$

where μ is the mean molecular weight and k_b the Boltzmann constant. Then, we take the logarithm and replace ρ and T by the previous relation. This way, the equation depends on a smaller number of variables.

$$\ln T(z) = \ln p - \ln \rho + \ln \mu + \ln \left(\frac{m_u}{k_B} \right) \tag{3.9}$$
$$= (\gamma - 1) \ln \rho_c + n(\gamma - 1) \ln w + \ln \mu + \ln \left(K \frac{m_u}{k_B} \right) \tag{3.10}$$

Mass

As introduced in Chapter 1, the mass of a sphere of radius r within a star is given by:

$$m(r) = \int_0^r 4\pi r^2 \rho dr$$

By a change of variable (Eq.3.3), Lane-Emden solutions appear in the equation. Finally, we obtain

$$m(r) = -4\pi r^3 \rho_c \frac{1}{z} \frac{dw}{dz}. \tag{3.11}$$

Opacity

Opacity within the core is assumed to come from a combination of the electron scattering and free-free interactions with the species Y (He), X (H) and Z (metallicity).

$$\begin{aligned}\kappa &= \kappa_{ff} + \kappa_{sc} \\ &= 3.8 \times 10^{22}(1+X)[Y+X+B]\rho T^{-7/2} + [0.20(1+X)]\end{aligned} \tag{3.12}$$

Where for a metallic species i : $B = \sum_i \frac{X_i Z_i^2}{A_i}$ with Z_i the atomic number, A_i is the atomic mass and X_i is the abundance of the element. In this case, the other species are oxygen and carbon.

Nuclear rates

The nuclear rate equation in the convective core is assumed to come only from the *3-α reaction*, 3He → C. In this case, the nuclear rate is expressed as

$$\varepsilon = c^{st}\rho^2 Y_c^3 T_8^{-3} \exp\left(-44.027/T_8\right), \tag{3.13}$$

Where $T_8 = T(K)/10^8$.

Luminosity

The nuclear reaction rates is needed to obtain the analytical expression of the luminosity. As mentioned in Chapter 1, the luminosity is given by

$$L(z) = \int \varepsilon dm = \int_0^z \varepsilon \frac{dm}{dz} dz.$$

It can therefore be expressed as

$$L(z) = \int c\rho(z)^2 Y_c^3 B(T) dm \tag{3.14}$$

$$= cY_c^3 \int_0^z \rho(z)^2 B(T) \frac{dm}{dz'} dz', \tag{3.15}$$

Where $B(T) = T_8^{-3} \exp\left(-44.027/T_8\right)$ with the notation $T_8 = T(K)/10^8$.

Radiative gradient

Finally, we take the radiative gradient definition:

$$\nabla_{\text{rad}} = \frac{3\kappa PL}{16\pi acGmT^4}, \tag{3.16}$$

Where the dependence on the luminosity, temperature, opacity, mass and pressure is clear.

3.3 Methodology

In order to solve the Lane-Emden equation, a Python code is developed using a numerical method, a 4th-Order Runge-Kutta. This section describes the general idea behind the code given in Appendix A that also implements numerically the physical

quantities of a star based on the polytropes model i.e. the equations derived in the previous section.

3.3.1 Numerical Resolution

The 4th-Order Runge-kutta numerical method is used to approximate the solutions of differential equations on a grid of points separated by a step h. The general formula is the following. Starting with the problem to solve:

$$\begin{cases} \frac{\mathrm{d}y}{\mathrm{d}x} = f(x, y) \\ y(x_0) = y_0 \end{cases}$$

For a point $i \in [x_0, x_{max}]$, the solution at the point $(i + 1)$ is given by:

$$y_{i+1} = y_i + \frac{1}{6}(k_1 + 2k_2 + 2k_3 + k_4), \tag{3.17}$$

where the coefficients are given by

$$\begin{aligned} k_1 &= hf(x_i, y_i) \\ k_2 &= hf(x_i + \frac{h}{2}, y_i + \frac{k_1}{2}) \\ k_3 &= hf(x_i + \frac{h}{2}, y_i + \frac{k_2}{2}) \\ k_4 &= hf(x_i + h, y_i + k_3) \end{aligned}$$

In order to solve numerically the Lane-Emden equation, which is a 2^{nd}-order differential equation,

$$\frac{1}{z^2}\frac{d}{dz}\left(z^2\frac{dw}{dz}\right) + w^n = 0,$$

It is separated into two 1^{st}-order differential equations with a change of variable. The Lane-Emden equation becomes a system of two equations:

$$\begin{cases} v = \frac{\mathrm{d}w}{\mathrm{d}z} = f(z, w, v) \\ \frac{\mathrm{d}v}{\mathrm{d}z} = -w^n - \frac{2}{z}v = g(z, w, v) \end{cases} \tag{3.18}$$

We want to find the solutions $v(z)$ and $w(z)$, with the initial conditions given by the power series expansion (Eq. 3.5) $w(z_0)$ and $v(0) = 0$. As there are 2 functions to find, the **RK-4** formula becomes:

$$\begin{cases} w_{i+1} = w_i + \frac{1}{6}(k_1 + 2k_2 + 2k_3 + k_4) \\ v_{i+1} = v_i + \frac{1}{6}(l_1 + 2l_2 + 2l_3 + l_4) \end{cases} \tag{3.19}$$

where the coefficients are given by:

$$
\begin{aligned}
k_1 &= hf(z_i, w_i, v_i) \\
l_1 &= hg(z_i, w_i, v_i) \\
k_2 &= hf(z_i + \frac{h}{2}, w_i + \frac{k_1}{2}, v_i + \frac{l_1}{2}) \\
l_2 &= hg(z_i + \frac{h}{2}, w_i + \frac{k_1}{2}, v_i + \frac{l_1}{2}) \\
k_3 &= hf(z_i + \frac{h}{2}, w_i + \frac{k_2}{2}, v_i + \frac{l_2}{2}) \\
l_3 &= hg(z_i + \frac{h}{2}, w_i + \frac{k_2}{2}, v_i + \frac{l_2}{2}) \\
k_4 &= hf(z_i + h, w_i + k_3, v_i + l_3) \\
l_4 &= hg(z_i + h, w_i + k_3, v_i + l_3)
\end{aligned}
$$

This part of the code is given in Appendix A.1. A convective core is generally described by an index $n = 3/2$. In the latter case, the real solution $w(z)$ cannot be negative since the term w^n lies in the Lane-Emden equation 3.1. Therefore, the polytropic indexes are processed separately in the code.

3.3.2 Slope Approximation

In order to obtain the polytropic relation between pressure and density (Eq.3.7), and to obtain the constants (γ, K n), we make a linear fit of the logarithmic relation between P and ρ in the **convective core** (Fig.2.17). It allows to obtain the coefficients of the straight line (Appendix A.3.1). The is done on a stellar model of $1M_\odot$ at the early state Y_c=0.90 (Fig. 3.2). The resulting parameters are the following:

Taking 1 $M_\odot$, we find $n = 1.55$, $K = 13.03\ 10^{12}$, $\gamma = 1.64$.

The straight lines are perfectly matched, this already indicates the interest of using the polytropes to express the pressure and density.

3.3.3 Physical Parameters Implementation

The equations introduced in the previous section 3.2.3 are implemented into the code through python functions, using the Lane-Emden solutions computed previously (Appendix A.3.2).

3.4 Results and Discussion

3.4.1 Density

The results for the density profile at early state of evolution Y_c=0.90 is presented in Figure 3.3, where a comparison between the analytical model *Clés* and the polytropes model in terms of the variable z is shown. The radial distance r can be converted into z following equation 3.3. The vertical line indicates the convective core limit (Schwarzschild criterion). The polytropes approximation seems consistent

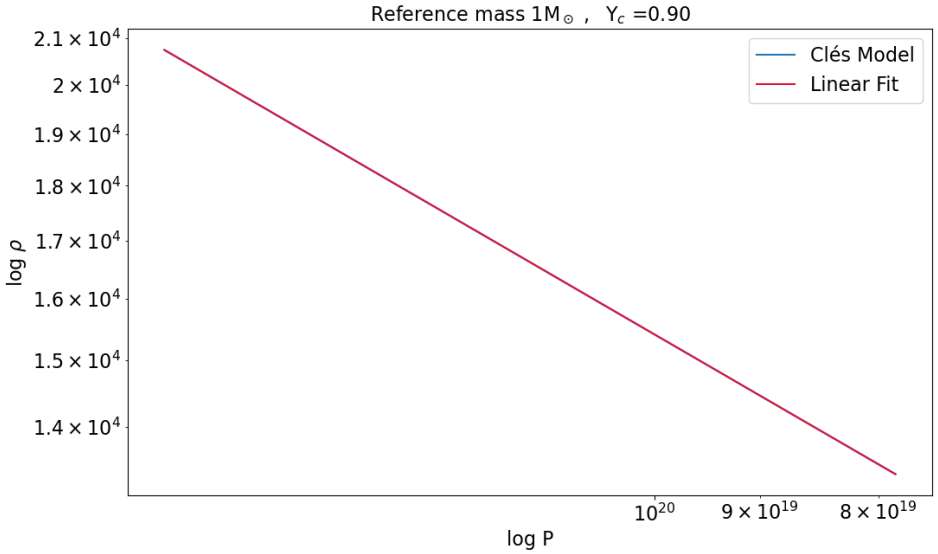

FIGURE 3.2: Log-Log plot of Pressure as a function of Density in the convective core (Schwarzschild criterion) for $1M_{\odot}$ and state Y_c=0.90. The model from *Clés* is in blue and the linear fit in red. Both lines are superposed.

when choosing the central density constant ρ_c from the model *Clés*. The matched profiles confirm that the polytropes model is able to describe the density trend in the convective core.

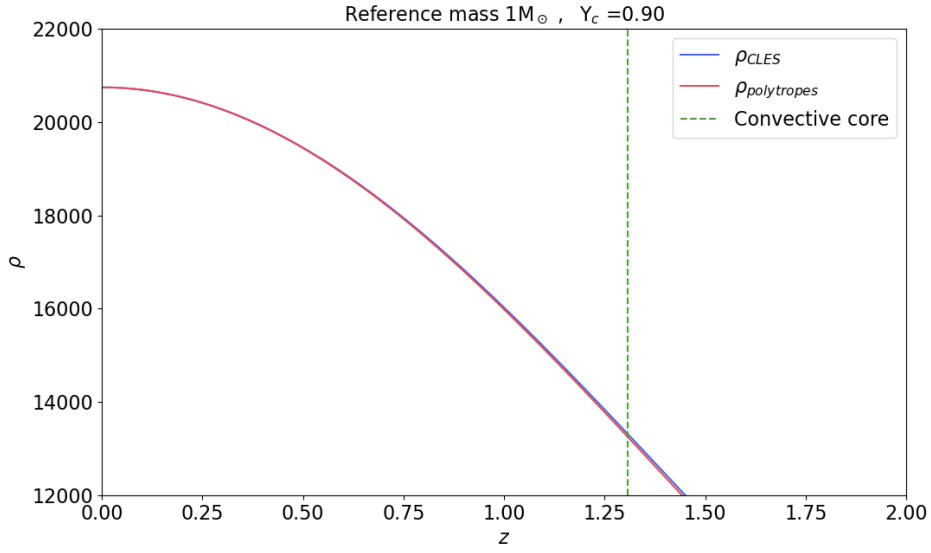

FIGURE 3.3: Comparison between the Density profiles from the polytropes model (red) and *Clés* (blue) as functions of the variable z, at the age 4 Myr and state Y_c=0.90. The convective boundary (Schwarzschild criterion) is the dashed green line.

3.4.2 Pressure

The pressure profile comes directly from the polytrope equation 3.1. With a fit of parameters, we retrieved the constant of the analytical expression of P. The result for an early model (Y_c=0.90) is shown in Figure 3.4. The comparison with *Clés* model is just as conclusive.

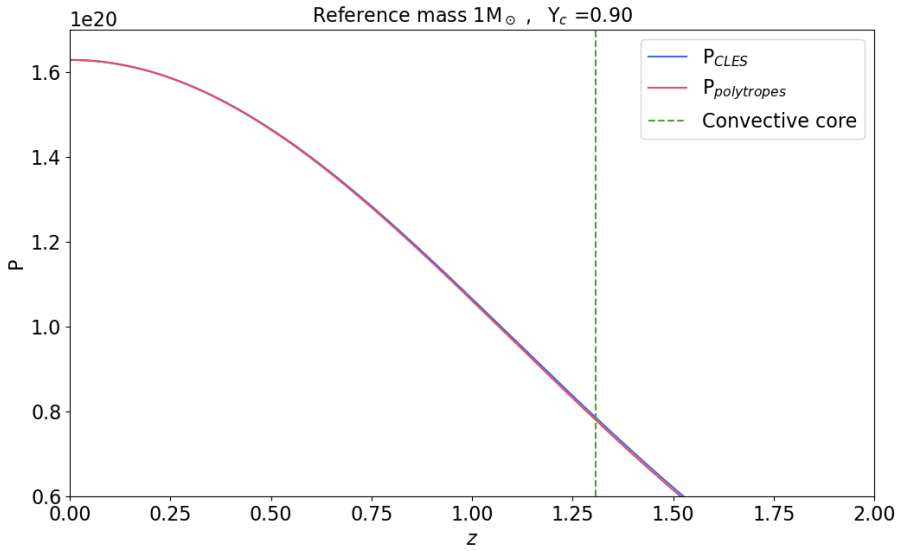

FIGURE 3.4: Comparison between the Pressure profiles from the polytropes model (red) and *Clés* (blue) as functions of the variable z, at the age 4 Myr and state Y_c=0.90. The convective boundary (Schwarzschild criterion) is the dashed green line.

3.4.3 Temperature

The approximation of the temperature expression (Eq.3.9), follows the ideal gas law. Figure 3.5 shows the result of the simulation in an early stage of evolution. In the first panel, we observe that the curves do not coincide. However, the similar shapes show that despite being too simplified , the analytical expression is sufficient to explain the origin of the profile.

The overestimation could be attributed to the ideal gas law approximation. For the purpose of this model, we can adjust the central **constant** T_c to fit the model *Clés* at the centre. Once it is done, the second panel confirms that the profile is well approximated by the simple model. It allows to understand analytically where the trend of the temperature profile comes from, which is among other things, its dependence on the molecular weight.

3.4.4 Mass

Figure 3.6 shows that the approximation of the mass (Eq. 3.11) is consistent as the two models are well matched. This confirms that the origin of the profile comes directly from the definition of the mass of a sphere of matter ρ and radius r. The mass increases with radius while density decreases towards the surface.

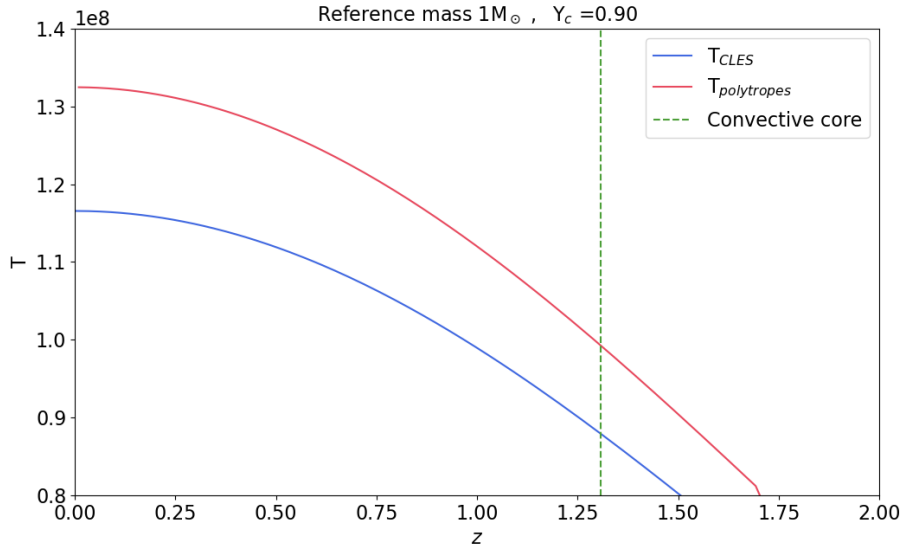

(A) Temperature profiles, without a fit of the polytropes model.

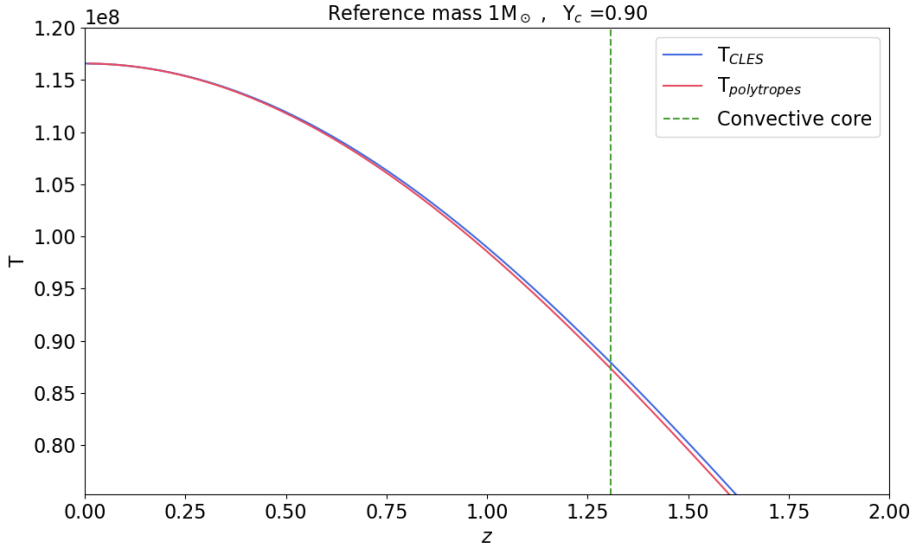

(B) Temperature profiles with a fit on the constant of polytropes model.

FIGURE 3.5: Comparison between the Temperature profiles from the polytropes model (red) and *Clés* (blue) as functions of the variable z, at the age 4 Myr and state Y_c=0.90. The convective boundary (Schwarzschild criterion) is the dashed green line. The first panel is the result for the unchanged constant of the analytical equation. The second panel is the result with a fit.

3.4.5 Nuclear Reactions

To investigate the rise of the radiative gradient, the opacity and luminosity implementation are needed (Eq. 3.16). The luminosity profile is obtained with the use of the nuclear reaction rate ϵ. The result is shown in Figure 3.7. The profile coincides well with *Clés* in the convective core. The equation of the *3-α reaction* rate is therefore consistent at this early stage of evolution, where the reactions evolving heavier elements are neglected. However, this approximation is too simple to remain efficient

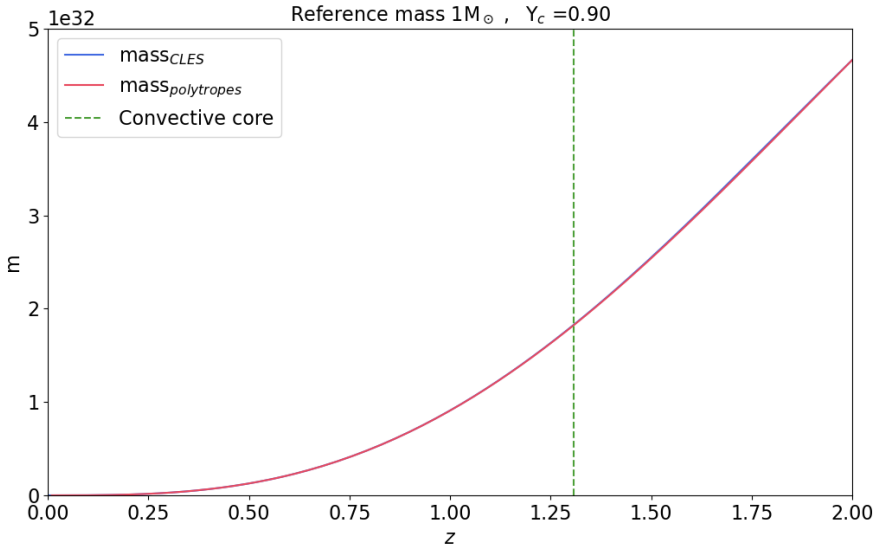

FIGURE 3.6: Comparison between the Mass profiles from the polytropes model (red) and *Clés* (blue) as functions of the variable z, at the age 4 Myr and state Y_c=0.90. The convective boundary (Schwarzschild criterion) is the dashed green line.

in later stages where other reactions take place such as the carbon burning.

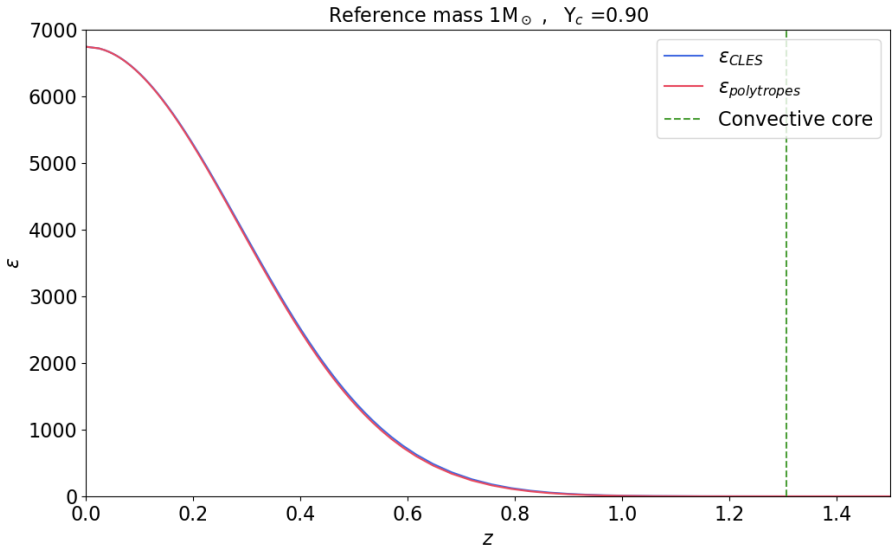

FIGURE 3.7: Comparison between the Nuclear Rate profiles from the polytropes model (red) and *Clés*(blue) as functions of the variable z, at the age 4 Myr and state Y_c=0.90. The convective boundary (Schwarzschild criterion) is the dashed green line.

3.4.6 Luminosity

The modelled luminosity profile is shown in Figure 3.8. The shapes are well matched except at the function maximum, which is slightly underestimated. This could come

from the nuclear reaction rate implementation which only consider the reactions *3-α* as an energy source. Nevertheless, as the trend is well reproduced in this early stage, the main source of energy in the convective core comes from the core-He burning.

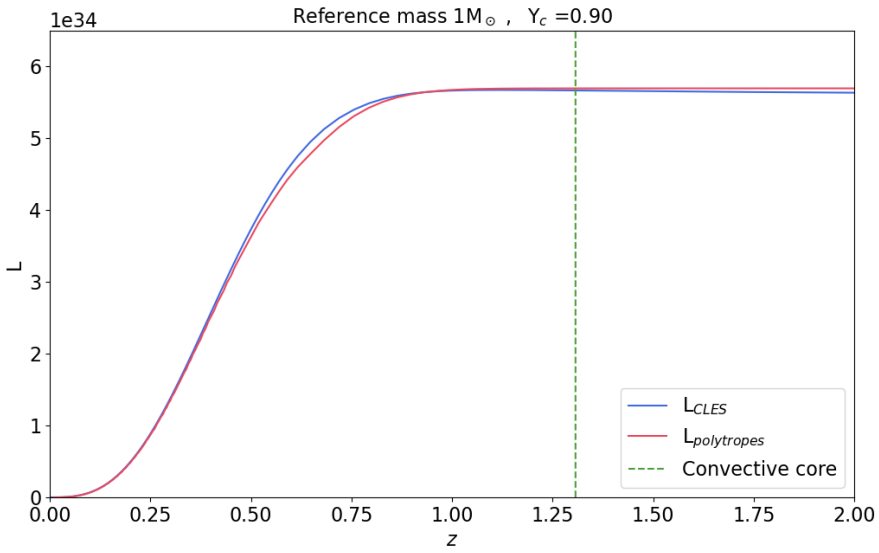

FIGURE 3.8: Comparison between the Luminosity profiles from the polytropes model (red) and *Clés* (blue) as functions of the variable z, at the age 4 Myr and state Y_c=0.90. The convective boundary (Schwarzschild criterion) is the dashed green line.

3.4.7 Opacity

The result of the modelled opacity is shown in Figure 3.9. There is a small gap between the opacity from the polytropes model and from *Clés* (±0.05).

The simplified model overestimates the opacity but **recreates the trend** of the parameter. This confirms that the free-free interactions and electron scattering play a big role in the central opacity. Most likely, another process has been missed, which could explain the gap. This could be the **conduction** by free electrons, playing a role as an energy transport. As mentioned in the introductory Chapter 1, there are 3 ways to carry energy from deep layers to upper layers: radiation, convection and conduction. Here, conduction has been neglected. The total opacity is therefore the harmonic mean of the radiative and conductive opacities, which explains why including conduction lowers it down. The equation taking the 3 transports into account has the general form:

$$\frac{1}{\kappa} = \frac{1}{\kappa_{\text{rad}}} + \frac{1}{\kappa_{cd}}$$

The model has a pedagogic purpose, the gap is therefore secondary to investigate the trend of the profile. The analytic expression of this model is therefore a mean to understand the *Clés* profile: the increase of opacity at the centre observed in Chapter 2 is caused by the production of **heavier elements** in the core i.e. the convective core mass increase. This interpretation comes from the strong dependence on the metallicity (heavier elements than He and H) lying in the opacity equation (Eq.3.12).

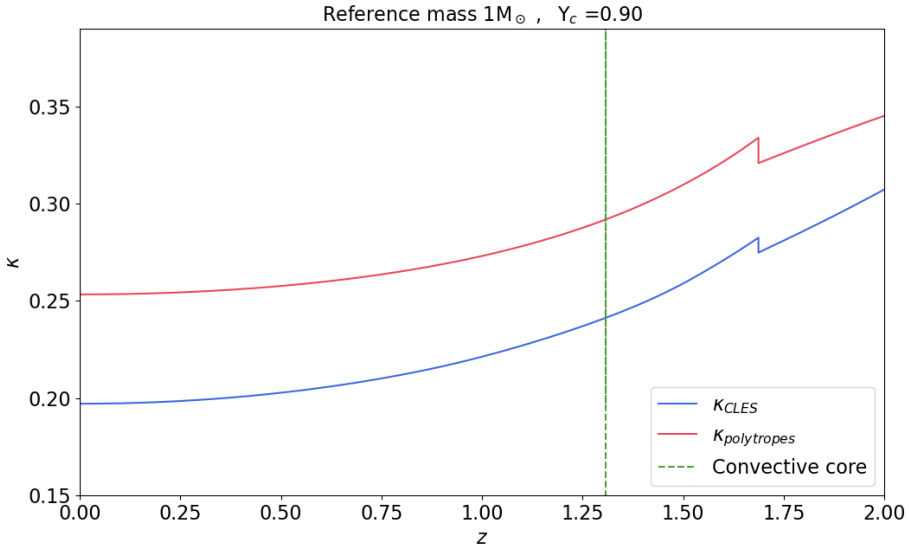

FIGURE 3.9: Comparison between the Opacity profiles from the polytropes model (red) and *Clés* (blue) as functions of the variable z, at the state and state Y_c=0.90. The convective boundary (Schwarzschild criterion) is the dashed green line.

3.4.8 Radiative Gradient

Finally, we study the gradient to explain its behaviour during the evolution. The result of the modelling is shown in Figure 3.10 for 2 different stages in the evolutionary sequence. The first panel shows an early stage (Y_c=0.90), where the profile matches the gradient from *Clés*. They have the same shape and as expected, the model no longer works outside the convective core. There is some noise near the centre of the star. This is certainly caused by error propagation due to the multiple dependence of the gradient on the physical parameters. In particular, the numerical resolution of the integral present in the analytical expression of the luminosity is more sensitive at the centre where there is a singularity L=0. To avoid error propagation, the various parameters in the analytical equation can be replaced by the ones from *Clés*. In any case, the model recreates nicely the trend of the gradient.

By looking at later stages in the second panel 3.10b, the difference with the *Clés* model is larger. This could come from the approximations made for the various physical parameters, which are less applicable when the star is further away in its evolution. For example, considering only the *3-α reaction* in the convective core becomes less efficient as the elements O and C become more abundant.

What could explain the rise of the radiative gradient ? To investigate this question, we take up the analytical expression of the gradient which shows on which parameters it depends, directly. Its rise can be explained in two ways. The first one is from a mathematical point of view: the gradient profile can be obtained from the Lane-Emden solutions. The latter exhibit a change of concavity in their shape (Fig.3.1). This implies that the profile of the physical parameters derived from these solutions also have this characteristic. This is therefore also the case for the radiative gradient, which have a change of concavity as it approaches the boundary of the convective

core. This explains its bell-shape.

The second way of explaining this increase in the overshooting layer is more physical. Highlighting the minimum point of the radiative gradient in the core (Fig.3.10) shows that the point hardly moves at all during the evolution. This contrasts with the limit of the convective core that moves towards the shell. The opacity profile for the same evolutionary stages (Fig.3.11) shows that it increases significantly at the point of minimum gradient z_0 during the evolution. The minimum gradient remains at a **fixed** value of **z** ($z_0 \sim 1.69$) and does not follow the expansion of the core. This means that z_0 comes closer and closer to the limit of the convective core since it expands. By combining this result with the concave aspect of the profile, the gradient has all the room to rise before the limit of the overshooting layer. This is also applicable to the opacity profile.

To summarise the discussion: the rise of the gradient is most likely due to the increase of opacity in the region between the convective core and the overshooting region. The minimum of the radiative gradient remains at a fixed value z_0. Since the convective boundary moves towards the shell, the boundary comes much closer to the fixed value z_0. As a consequence, the opacity profile and the radiative gradient have the space to rise before the shell.

3.5 Conclusion

The Polytropes Model proved effective in helping to understand the physical parameters profiles analysed in Chapter 2. It showed that the dependence between each quantity explains the trend observed previously. More precisely, thanks to this simpler way of visualising these parameters, the rise of the radiative gradient is investigated: the increase of opacity with the core mass increase seems to trigger a rise in the ∇_{rad} profile.

Finally, the minimum of the radiative gradient is reached at a fixed value z_0, which is interesting as it has never been observed by others. This helps us to understand why the phenomenon of rise of the radiative gradient appears in these stars and not in others: this comes from their convective cores that are so large that their boundary reaches and exceeds the limit value z_0. We can expect that in other stars, such as the convective cores of main-sequence stars, this phenomenon does not occur because their convective cores are not large enough.

A further investigation could be done, for example, by applying the same approach for a star with a smaller overshooting layer in order to study the rise of the gradient under this condition.

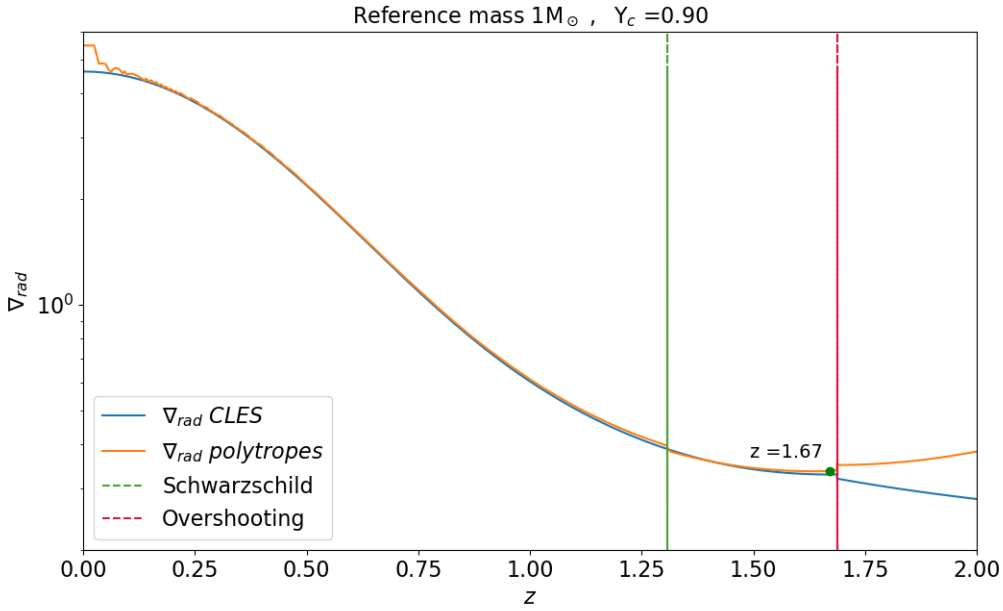

(A) Radiative gradient profiles at the state Y_c=0.90.

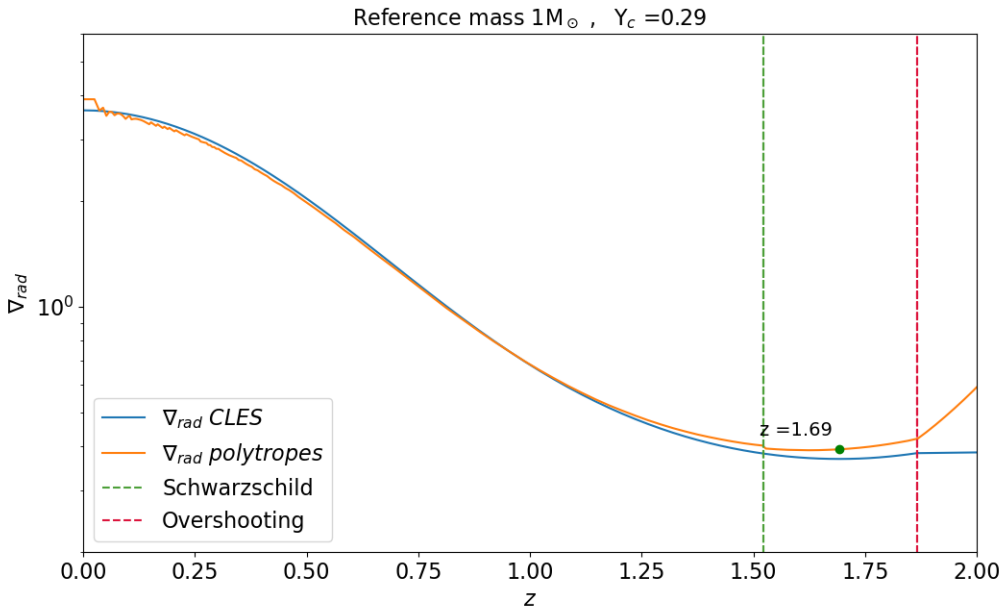

(B) Radiative gradient profiles at the state Y_c=0.29.

FIGURE 3.10: Comparison between the Radiative gradient profiles from the polytropes model (orange) and *Clés*(blue) as functions of the variable z. The convective boundary (Schwarzschild criterion) is the vertical green line and the overshooting boundary is the vertical red line. The black point indicates the minimum of the gradient.

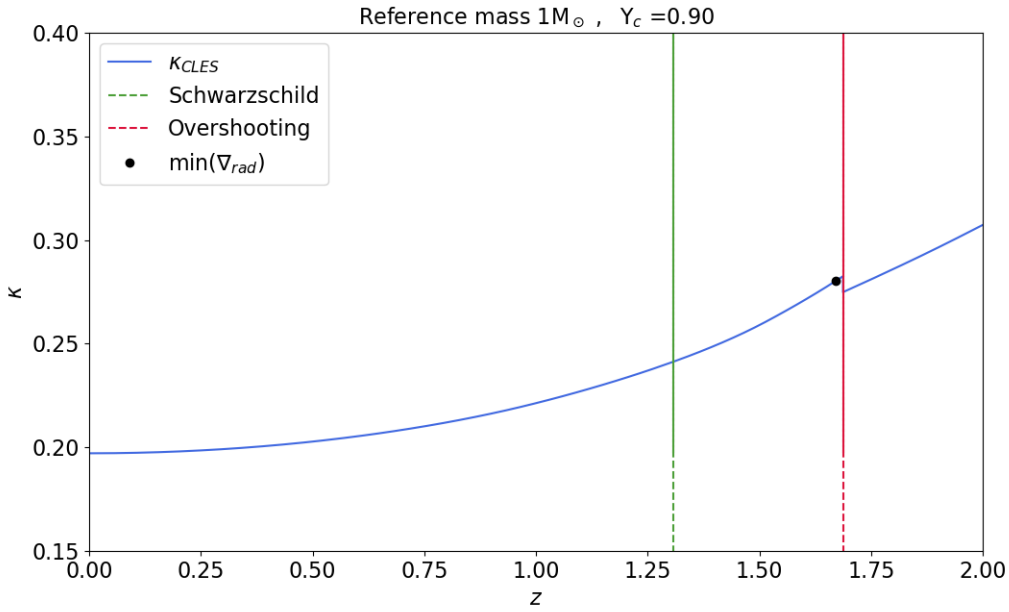

(A) Opacity profile at the age 4 Myr.

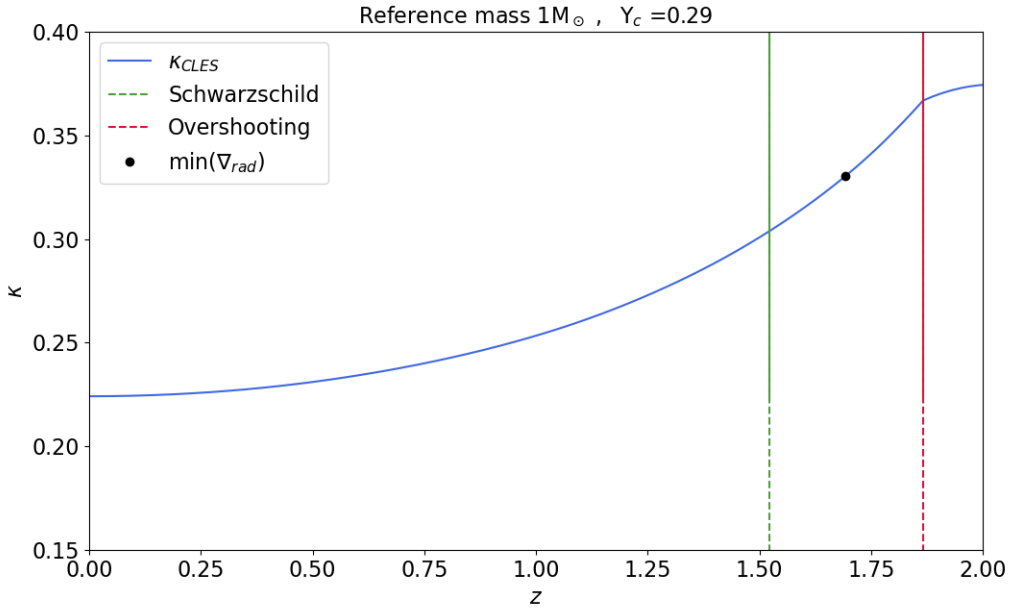

(B) Opacity profile at the age 81 Myr.

FIGURE 3.11: Opaicty profile from *Clés*(blue) as functions of the variable z. The convective boundary (Schwarzschild criterion) is the vertical green line and the overshooting boundary is the vertical red line. The black point indicates the minimum of the radiative gradient.

Chapter 4

Stellar Oscillations

4.1 Introduction

This Chapter introduces the theory of stellar oscillations and the related concepts, such as the Brunt–Väisälä frequency and the asymptotic theory. Asymptotic theory is characterised by so-called period spacing and large separation. These are analysed using the stellar evolution code *Clés*. Finally, the effects of the envelope mass and the core size are discussed.

4.1.1 Red Giant Asteroseismology

As introduced in Chapter 1, the interest of red giants asteroseismology is clear. The particularity of these stars is their mixed modes of oscillation. This provides an insight of the He-core and the envelope. We first study the parameters for a reference star, and then examine their dependence on the envelope mass and core size.

4.1.2 Non-radial adiabatic oscillations

In order to define the parameters discussed in this work, the equation describing the general case of non-radial oscillations within the interior of a star are introduced. The adiabatic oscillations is assumed i.e. no time to exchange energy on the time-scale of an oscillation.

We define $\vec{\xi} = (\xi_r, \xi_\theta, \xi_\phi)$ the displacement vector and take the asymptotic approximation where the wave vector scale $|k|$ is higher than the scale height of physical parameters such as the pressure. In this case, the equation of interest is given by:

$$\frac{d^2\xi_r}{dr^2} + k^2(r)\xi_r \approx 0, \tag{4.1}$$

where

$$k^2 = \frac{1}{c^2}\left(1 - \frac{L_l^2}{\sigma^2}\right)(\sigma^2 - N^2) \quad \text{is the wave vector}$$

and

$$N^2 = \frac{Gm}{r}\left(\frac{1}{\Gamma_1}\frac{d\ln P}{dr} - \frac{d\ln \rho}{dr}\right) \quad \text{Brunt-Väisälä frequency,}$$

$$L_l^2 = \frac{l(l+1)c^2}{r^2} \quad \text{Lamb frequency,}$$

$$\sigma^2 \quad \text{Wave frequency.}$$

The perturbed solutions are obtained using the separation of variables. This method can be used to write solutions of the governing equations within the interior of a star, described in Chapter 1, as

$$X'(r,\theta,\phi) = X'(r)Y_l^m(\theta,\phi).$$

We denote the function $Y_l^m(\theta,\phi)$, the spherical harmonics which are eigenfunctions of the legendrian operator L^2:

$$L^2 Y_l^m(\theta,\phi) = l(l+1)Y_l^m(\theta,\phi),$$

where

$$L^2 = -r^2\nabla_h^2 = -\frac{1}{sin(\theta)}\frac{\partial}{\partial\theta}\left(sin(\theta)\frac{\partial}{\partial\theta}\right) - \frac{1}{sin^2(\theta)}\frac{\partial^2}{\partial\phi^2}$$

with ∇_h, the nabla operator for horizontal coordinates (θ,ϕ).

The variables l and m define respectively the spherical harmonic degree and order. A spherically symmetric star has no dependence on the variable m, meaning that only a different l corresponds to a different mode of oscillation.

The Brunt-Väisälä frequency can be written as a function of the gradients:

$$N^2 = g\left(\frac{1}{\Gamma_1}\frac{d\ln P}{dr} - \frac{d\ln\rho}{dr}\right) \tag{4.2}$$

$$\approx \frac{\rho g^2}{P}(\nabla_{ad} - \nabla + \nabla_\mu), \tag{4.3}$$

where

$$\nabla = \frac{d\ln T}{d\ln P}\ ,\ \nabla_{ad} = \left.\frac{\partial\ln T}{\partial\ln P}\right|_S\ ,\ \nabla_\mu = \frac{d\ln\mu}{d\ln P}.$$

Taking the case $k^2 > 0$, the equation 4.1 describes a wave propagating in a cavity with the wave vector k. We can identify two different ways for it to propagate:

$$\text{Case 1:}\quad \sigma^2 > N^2 \text{ and } \sigma^2 > L_l^2$$
$$\text{Case 2:}\quad \sigma^2 < N^2 \text{ and } \sigma^2 < L_l^2$$

The first case corresponds to a regime at high frequency and is called the pressure mode (p-mode). The second case corresponds to a regime at low frequency and is called the gravity mode (g-mode).

↪ **Pressure modes** are stellar oscillations that behave as acoustic waves. In this case, the wave vector becomes

$$k_r^2 \approx \frac{\sigma^2}{c^2}.$$

The waves propagate at the local sound speed $c(r)$ by compression and expansion of material. Pressure modes are also described through the asymptotic theory in the limit of high frequencies. The separation between 2 consecutive **frequencies** of p-modes is more or less constant. In other words, for a mode n and *n-1* of the same number l:

$$\Delta\nu_{n,l} = \nu_{n,l} - \nu_{n-1,l} \sim \left(\int_0^R \frac{\mathrm{d}r}{c}\right)^{-1}. \tag{4.4}$$

This is called the **large separation** and it is used as a seismic indicator for p-modes.

↪ **Gravity modes** on the other hand, are oscillation waves resulting from a horizontal motion of matter. The physical interpretation of such a mode can be understood as the consequence of the force restoring the balance in a slice of material, where elements of matter are heavier or lighter than the surrounding medium. It results in horizontal motions that behave like a wave. In this case, the wave vector becomes

$$k_r^2 \approx l(l+1)\frac{N^2}{\sigma^2 r^2},$$

where there is a strong dependence on the Brunt-Vaisälä frequency. In analogy to the p-modes, the main feature describing the g-modes is the asymptotic theory valid in the limit of high periods. In this case, the separation between two consecutive **periods** of modes is constant. In other words, for a mode n and *n-1* of the same number l:

$$\Delta\Pi_{n,l} = P_{n,l} - P_{n-1,l} \sim I^{-1} = \left(\int_{r_1}^{r_2} \frac{N}{r}\mathrm{d}r\right)^{-1}, \tag{4.5}$$

where $I = \int \frac{N}{r}\mathrm{d}r$ is a useful integral to study g-modes.

The case $k^2 < 0$ corresponds to a region called *Evanescent Zone*, where the eigenfunctions have an exponential behaviour similar to quantum tunnelling.

4.1.3 Mode trapping

Actually, there are regions where a mode can propagate while exponentially vanishing away from it. As the oscillation is restrained to this region, it is called a trapped region. The boundary of a trapped region is usually called as *turning points* due to the waves reflecting on these points. This means that the specific mode has large amplitudes in the trapping region and much smaller ones away from it.

4.1.4 Mixed mode

In the case of main sequence stars, the trapping regions of g- and p-modes are separated. That makes a clear distinction of the mode frequencies observed (σ_g or σ_p). However, the modes of evolved stars such as the core-He burning phase can be different from pure g- or p-modes and are called **mixed modes**. These stars have a high contrast of density between the centre and envelope[1]. The Brunt-Vaisälä frequency strongly depends on density (Eq.4.2) therefore, N is high in the radiative inner part of a star and decreases significantly in the envelope, until reaching the boundary of the convective part of the outer layers where it drops. The cavities of g- and p-modes are then very close, *coupled*. As a consequence, the observed frequency range corresponds to a gravity mode in the deep interior (where the Brunt-Vaisälä and Lamb

[1]The envelope has a low density while the core is dense.

frequency are high, implying $\sigma^2 < N^2, L_l^2$) and corresponds to a pressure mode in the convective envelope (where the Brunt-Vaisälä and Lamb frequency are low, implying $\sigma^2 > N^2, L_l^2$). The distinction of frequency between g- and p-mode is therefore, not clear anymore. Figure 4.1 shows what is called a propagation diagram (Basu and Hekker, 2020). The observed frequency range corresponds to a g-mode in deeper layers and to a p-mode in outer layers.

As a result, it is possible to measure both the period spacing typical of g-modes **and** the large separation typical of p-modes. These features can give valuable information on the internal structure of a star such as the physical properties of its core and its stage of evolution. As an example, figure 4.2 shows the period spacing as a function of the large separation (Mosser et al., 2014). This figure presents data points corresponding to various stars. Depending on the evolutionary state, a star will occupy a different position in the diagram. Indeed, we observe a cluster of stars in the state of H-shell burning (ascending the Red Giant Branch RGB), in the lower part of the diagram, and another one in the Core-He burning phase (called the Red clump), in the upper part of the diagram. The position within the group also indicates the current state of a star (how far it is on its branch of evolution). This illustrates the valuable information that red giants asteroseismology can give.

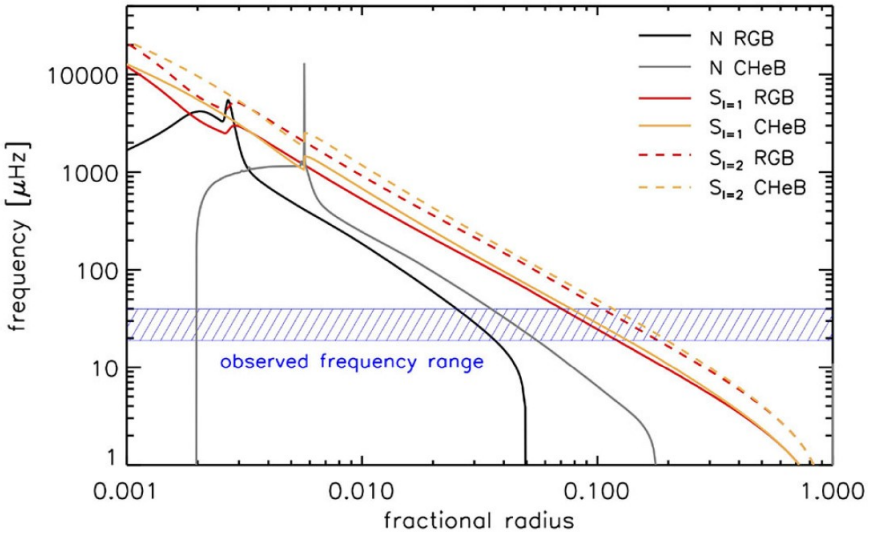

FIGURE 4.1: Propagation diagram for a model of 1 $M_\odot$ RGB star and Core-He burning star (CHeB) (Basu and Hekker, 2020) . The Brunt–Vaisälä frequency N and the Lamb frequency S_l (for l=1 and l=2) are in grey and orange for the CHeB star. The observed frequency is indicated with a blue horizontal line. The H-burning shell of the CHeB star is located around the peak of the Brunt-Vaisälä frequency and the convective boundary of the envelope, in the right part of the figure.

4.2 Modelling

This study uses the code of stellar evolution *Clés*. The introduction to this model and its initial parameters is described in the section 2.2. Similarly to Chapter 2, this Chapter contains a study of the effect of **Envelope Mass** and **Overshooting**. At first, we study the Period-Frequency spacing diagram and the Brunt-Vaisälä frequency

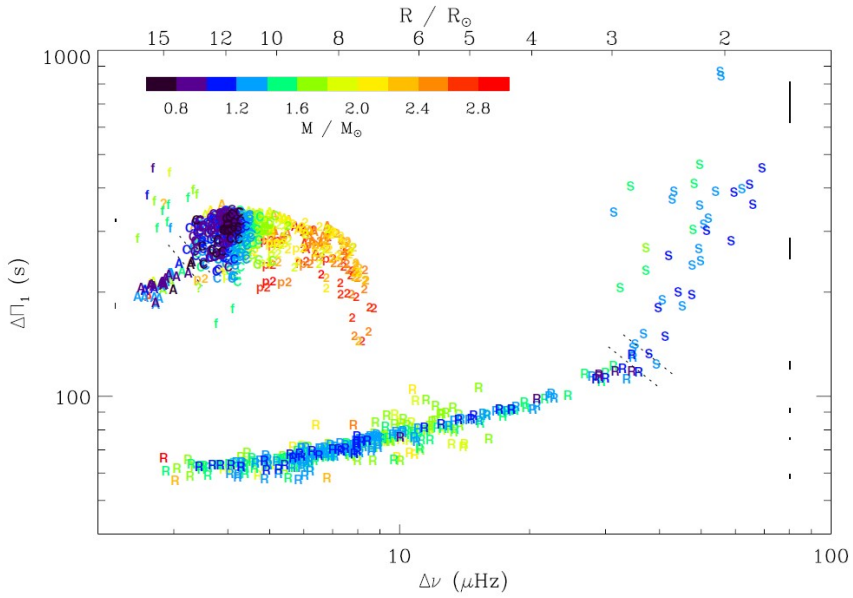

FIGURE 4.2: Seismic $\Delta\Pi - \Delta\nu$ diagram for various stars (Mosser et al., 2014). The relative mass is indicated with a colour-bar and the stage of evolution by a letter.

profile for a star of reference (1 $M_\odot$) then, we use a set of total masses (from 1 $M_\odot$ to 1.8 $M_\odot$) to change the envelope mass. Finally, the size of the overshooting zone is altered to study the impact on the seismic signature.

4.3 Results and Discussion

4.3.1 Reference Mass

This section reviews the profiles of the parameters of interest for a reference mass, 1 $M_\odot$.

Period Spacing and Large Separation

The seismic diagram $\Delta\Pi - \Delta\nu$ can reveal information on the internal layers of a star during its evolution, based on the dependence of the period spacing with the Brunt-Vaisälä frequency (Section 4.1.2).

Figure 4.3 shows the relation for the main part of the evolution (from Y_c=0.9 up to the critical Y_c=0.1). The small loop at the beginning of the sequence is similar to the one in the H-R diagram (Fig. 2.2) and could be an effect of the onset of the core-He burning. Starting in the early stages $\sim$ Y_c=0.91, up to a value around Y_c=0.34, the period spacing $\Delta\Pi$ increases. Beyond this state, a turnover in the profile appears. This is familiar with the bifurcation in the H-R diagram observed for the same helium abundance $Y_c \in [0.34, 0.32]$, in Chapter 2. The $\Delta\Pi$ starts to decrease until the end of the sequence. Brunt-Vaisälä frequency profile could explain this behaviour.

Brunt-Vaisälä Frequency

As mentioned in the equation 4.2, the Brunt-Vaisälä frequency strongly depends on the adiabatic gradient, real gradient and molecular weight gradient. In the mixed

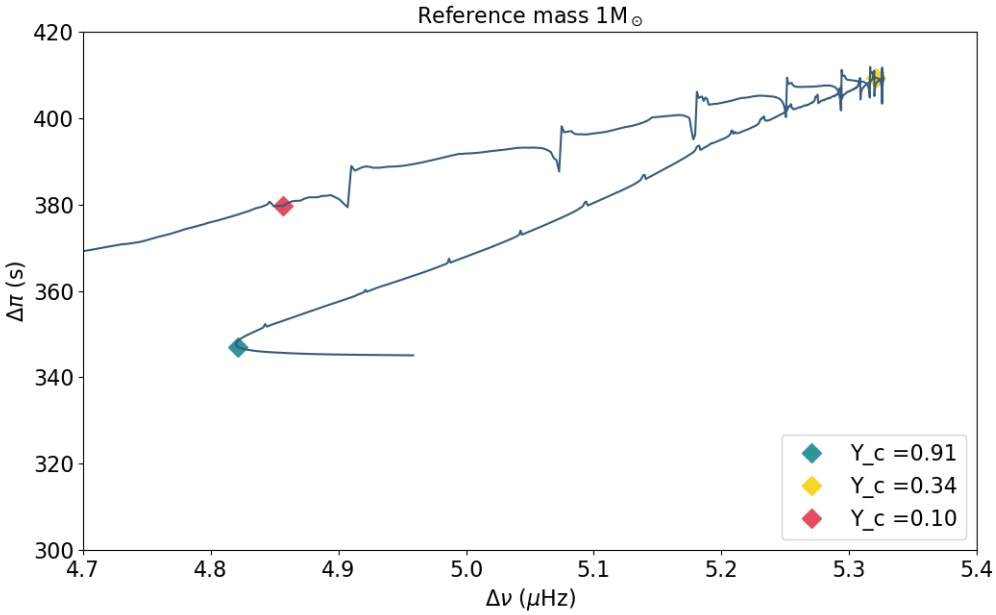

FIGURE 4.3: Figure $\Delta\Pi - \Delta\nu$ for 1 $M_\odot$ core-He burning star. The markers indicate a state of central helium abundance (Y_c=0.91 in blue ,Y_c=0.34 in yellow and Y_c = 0.10 in red).

core (convective core + overshooting zone), the adiabatic gradient is set as equal to the real gradient ($\nabla_{ad} = \nabla$). Furthermore, the molecular weight gradient vanishes in this region due to the homogeneous composition ($\nabla_\mu = 0$). As a consequence, the Brunt-Vaisälä frequency also **vanishes** in the mixed core and has a non-zero profile in the radiative parts. This is illustrated in Figure 4.4a, where the Brunt-Vaisälä frequency is presented as a function of the mass ratio $m/M_\odot$ and placed in parallel to the helium profile. The Brunt-Vaisälä frequency profile appears with a discontinuity at the mixed core boundary and peaks in the shell. The latter change comes from a change of chemical composition due to the hydrogen burning (Fig. 4.4b).

Figure 4.5 regroups some steps in the evolution, from early stages (first panel) to the state right before the semi-convective region appearance (second panel). We observe the following trend: the Brunt-Vaisälä frequency decreases in the shell while the discontinuity in the core is pushed towards the shell due to the convective core's mass increase. The decrease of N^2 in the shell can be related to the decreasing trend of the density profile observed in Chapter 2.

The effect of the semi-convective region is illustrated in Figure 4.6. The first panel 4.6a presents the Brunt-Vaisälä frequency while the other one 4.6b shows the helium profile at the same stage of evolution. The discontinuities in the Brunt-Vaisälä frequency profile can be explained by the density profile. Indeed, a density discontinuity on the boundary corresponds to an infinite density gradient, and therefore an infinite Brunt-Vaisälä frequency (Dirac delta function). As a result, the discontinuities will act as zone of partial reflection of the waves and may therefore also produce a mode trapping. Some associated seismic signatures are predicted as a consequence of this phenomenon and called "buoyancy glitches".

The peak on the semi-convective border ($\sim$ 0.2 m/M) is therefore caused by the sharp difference of composition between the inner and outer part of the boundary (Y has a step-shape profile). This sudden increase in the Brunt-Vaisälä frequency in the convective zone will probably have a signature on the period spacing of the mixed modes, similar to what is predicted and observed for main-sequence g-modes. In the latter case, this seismic signature is due to the variable chemical composition profile created by the convective core, whose mass decreases over time (Miglio et al., 2008). Asteroseismology should therefore allow to detect and characterise the semi-convective zone.

Finally, at the end of the sequence, central helium exhaustion induces a decrease of the convective core mass therefore, a global increase of density. This process is linked to the global increase of the Brunt-Vaisälä frequency (Fig.4.9).

We note that from one model to another, there is some sudden increase of the peak on the semi-convective boundary (Fig. 4.7b). These noises come from the numerical computation. ∇ , ∇_{ad} and ∇_{rad} separate from each other on the semi-convective border ($\nabla_{ad} \neq \nabla_{rad}$ and $\nabla_{rad} = \nabla$ beyond the discontinuity) and the numerical computation adjusts the model at some points before the boundary (Fig. 4.8), causing sudden peaks.

In the following study, we analyse the profile of the Brunt-Vaisälä frequency as a function of the relative radial distance (r/R) (Fig.4.10) instead of the mass ratio (m/M). This will enable us to study the behaviour of the period spacing in the $\Delta\Pi - \Delta\nu$ figure (Fig.4.3). the profile of N^2 moves rather rapidly towards the shell in terms of radial distance. This comes from the core that gradually takes over a greater part of the inside of the star during the evolution. As mentioned previously, the period spacing depends on the inverse of the Brunt Vaisälä integral $\Delta\Pi \sim \int (N/r)^{-1}$. The decrease of N^2 during the evolution, combined with the increase of the radial distance r of the core, is linked to the observed increase of the period spacing $\Delta\Pi$. At some point in the evolution, around the value Y_c= 0.30, the core slows down its expansion and finally, contracts rapidly. This reduces the radial parameter r in the Brunt Vaisälä integral and therefore explains the bifurcation in the seismic Figure 4.3, around Y_c= 0.34.

4.3.2 Envelope Mass Dependence

This section focuses on the effect of envelope mass on the various parameters. As previously, since the mass of the helium core remains unchanged, the variation of the envelope mass is quantified by changing the total mass of a star.

Period Spacing and Large Separation

Figure 4.12 shows the seismic $\Delta\Pi - \Delta\nu$ diagram for a set of stars (from 1 $M_\odot$ to 1.8 $M_\odot$). The curves start at roughly the same position. Then, during the evolution, they depart from each other while the period spacing increases. For a same value of $\Delta\nu$, the less massive is a star, the higher is $\Delta\Pi$. The curves have then a turn over around the same central helium abundance $\sim$ Y_c= 0.33. There is therefore a clear effect of the envelope mass on the seismic signature. Let us note that the various spikes in the curves are not physical and are noises from the numerical computation as they are not as marked for all the masses.

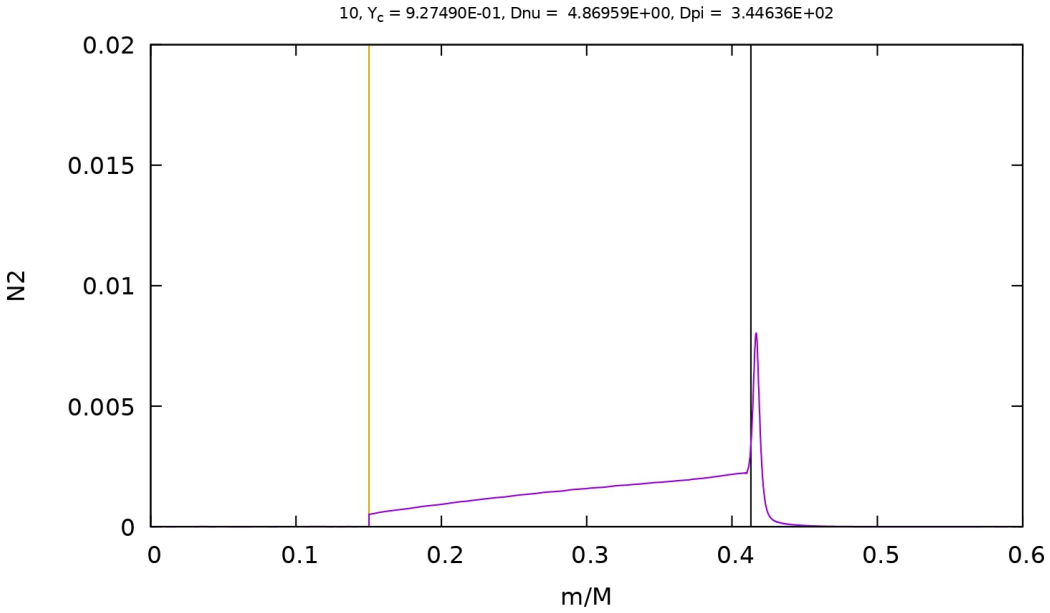

(A) Brunt-Vaisälä frequency profile for $Y_c = 0.93$.

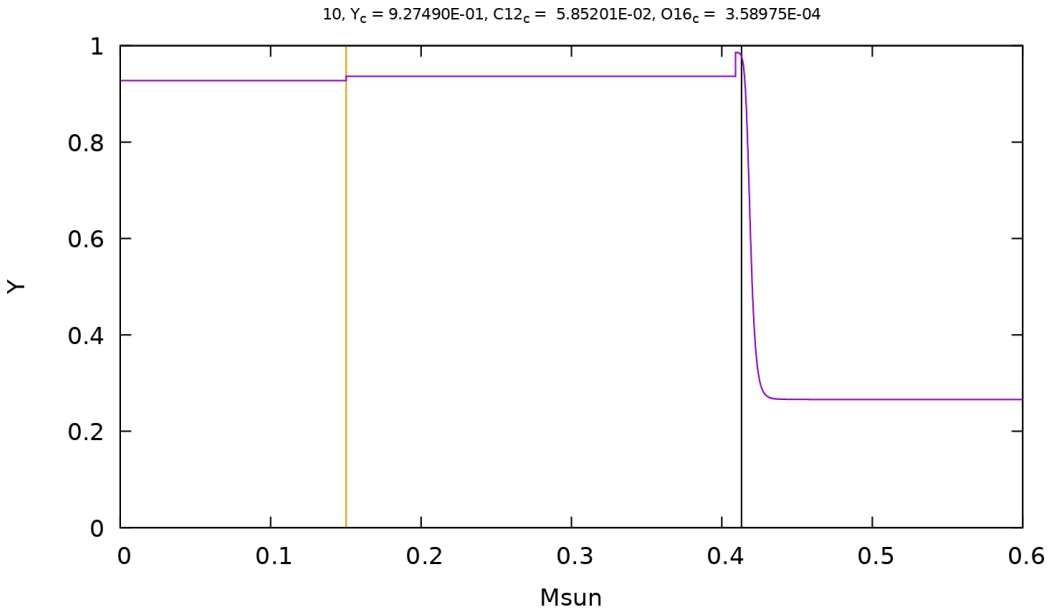

(B) Helium profile for $Y_c = 0.93$.

FIGURE 4.4: Brunt-Vaisälä frequency and the Helium profiles as functions of the mass ratio $m/M_\odot$ for 1 $M_\odot$ from the core up to the shell in the early stage of evolution $Y_c = 0.93$. The mixed core boundary (convective + overshooting layer) is the vertical orange line and the shell boundary is the vertical black line.

Brunt-Vaisälä Frequency

What is the effect of the envelope mass on the Brunt-Vaisälä frequency ? Figure 4.13 presents 3 stages of evolution in the sequence. In the first panel presenting the Zero-Age, we observe that the mixed core (convective core + overshooting) of each star has the same size in terms of mass ratio. As a consequence, the Brunt-Vaisälä

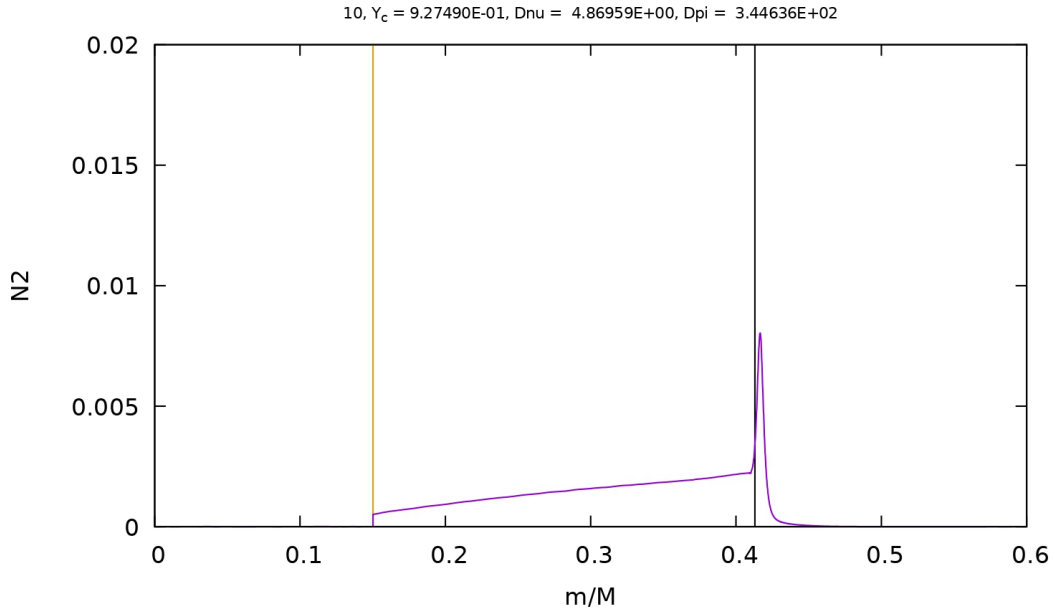

(A) $Y_c = 0.93$.

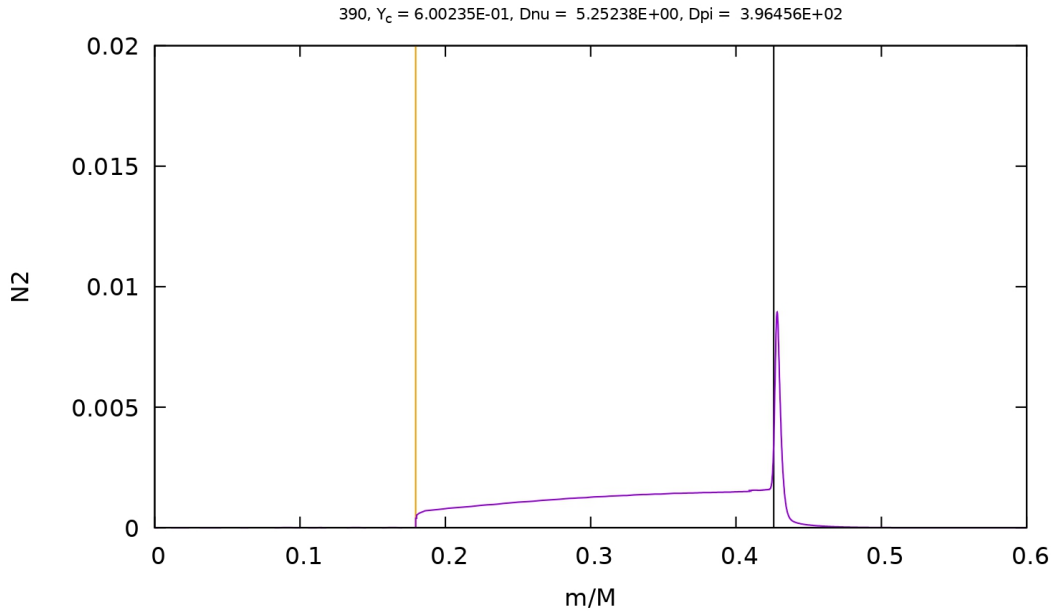

(B) $Y_c = 0.60$.

FIGURE 4.5: Brunt-Vaisälä frequency profile as a function of the mass ratio $m/M_\odot$ for 1 $M_\odot$ from the core up to the shell. The mixed core boundary (convective + overshooting layer) is the vertical orange line and the shell boundary is the vertical black line. The figure is divided into sub-figures extracted from the sequence of evolution.

frequency rises at the same point on the boundary of the region (~ 0.17 $m/M_\odot$). The peak located in the shell is higher for a lower-mass star. Then, during the evolution, this peak decreases for the set of stars at a different speed. Indeed, we notice that the gap between the height of the peaks decreases with time. In other words, the decrease of N^2 in the shell is higher for a less massive star (evolution from panel 4.13a to 4.13b). This could be linked to the faster increase of $\Delta\Pi$ for a less massive star.

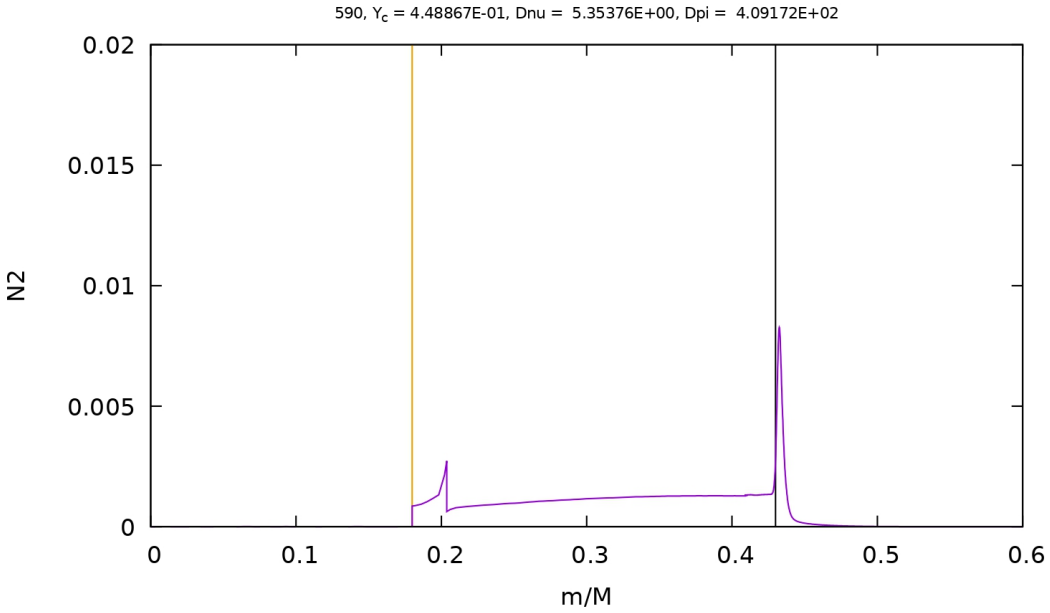

(A) Brunt-Vaisälä frequency profile for $Y_c = 0.45$.

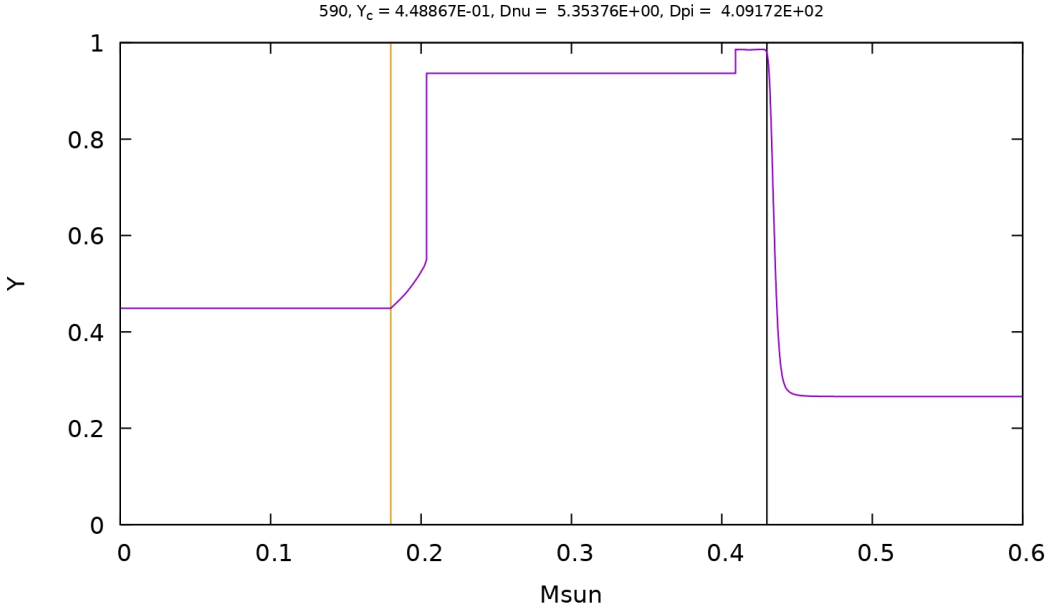

(B) Helium profile for $Y_c = 0.45$.

FIGURE 4.6: Brunt-Vaisälä frequency and the Helium profiles as functions of the mass ratio $m/M_\odot$ for 1 $M_\odot$ from the core up to the shell in the early stage of evolution $Y_c = 0.90$. The mixed core boundary (convective + overshooting layer) is the vertical orange line and the shell boundary is the vertical black line.

We also observe from these figures that the evolution is faster for more massive stars, where there is a faster advance of the H-burning shell and the discontinuity border. This is in perfect agreement with the discussion in the previous Chapter 2. Then, the appearance of the semi-convective layer (see the sub-figure 4.13b) creates a step in the frequency N^2 profile for each star.

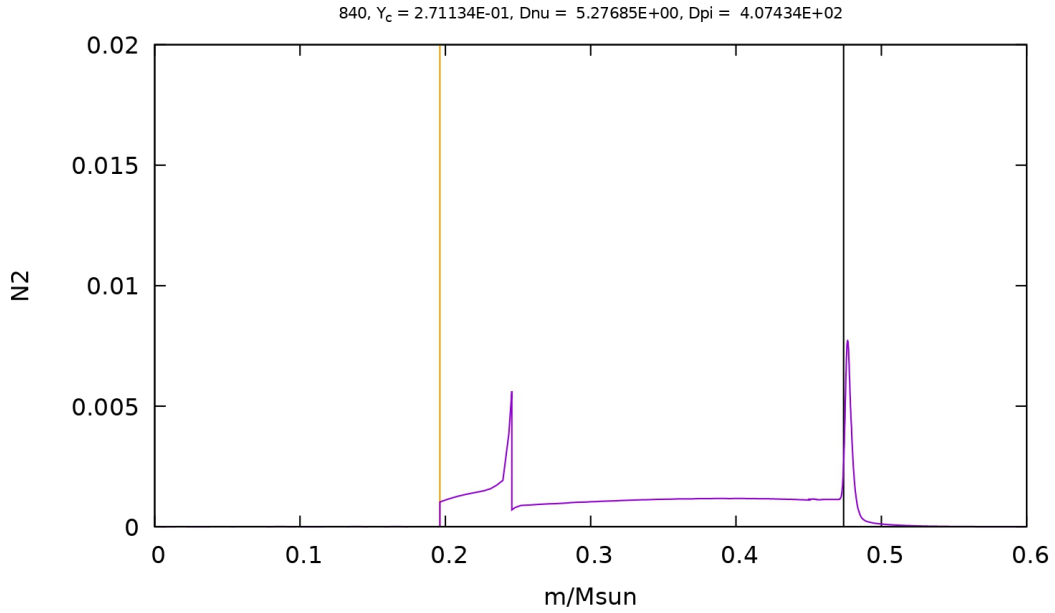

(A) $Y_c = 0.27$

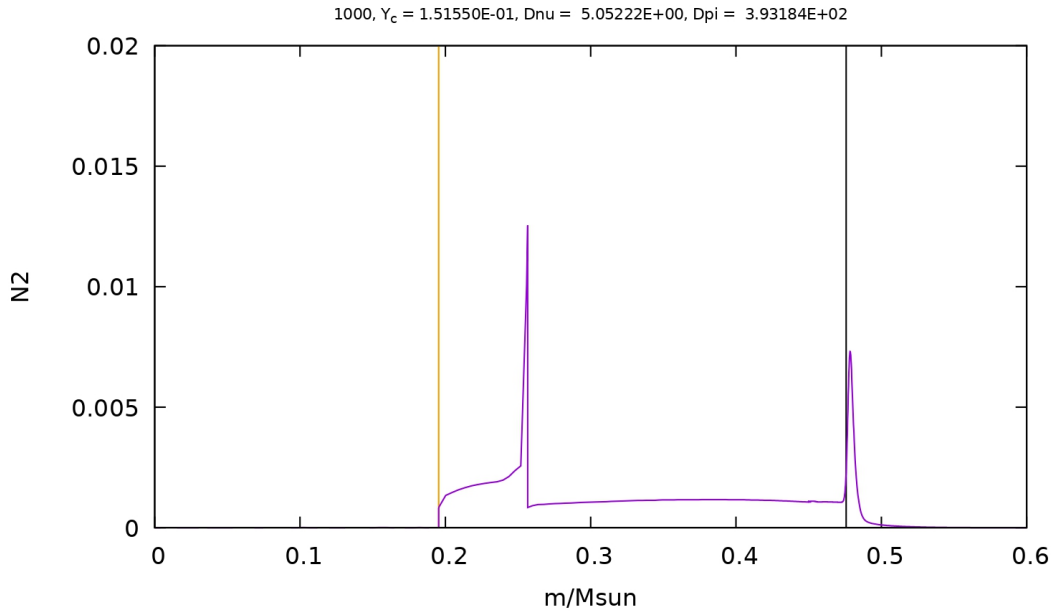

(B) $Y_c = 0.15$

FIGURE 4.7: Brunt-Vaisälä frequency profile as a function of the mass ratio $m/M_\odot$ for 1 $M_\odot$ from the core up to the shell. The mixed core boundary (convective + overshooting layer) is the vertical orange line and the shell boundary is the vertical black line. The figure is divided into sub-figures extracted from the sequence of evolution.

The last panel 4.13c, shows that some numerical noise can appear from one model to the other at the discontinuity border, as discussed previously.

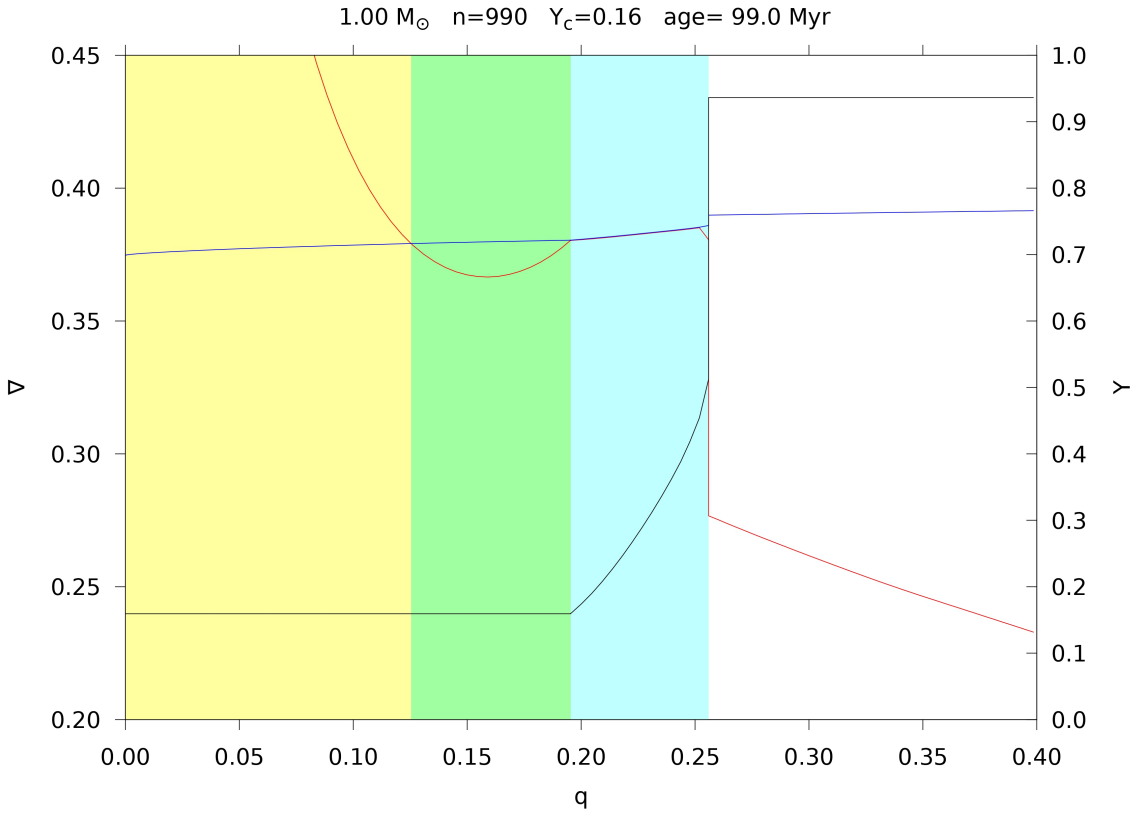

(A) Y_c=0.16

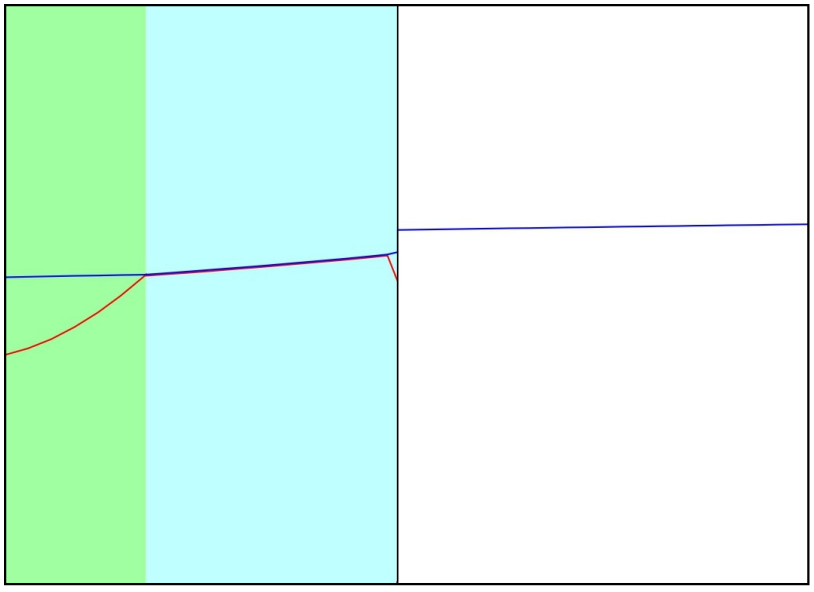

(B) Zoom around the mass ratio q = 0.25.

FIGURE 4.8: Gradients profiles and helium mass fraction profile as a function of the mass ratio for 1 $M_\odot$. The convective zone is in yellow, the overshooting layer in green and the semi-convective zone in light blue. The radiative gradient ∇_{rad} is in red and the adiabatic gradient ∇_{ad} in blue. For the real gradient ∇, $\nabla = \nabla_{ad}$ in the mixed core and $\nabla = \nabla_{rad}$ in the radiative core. The second panel is a zoom on the discontinuity boundary.

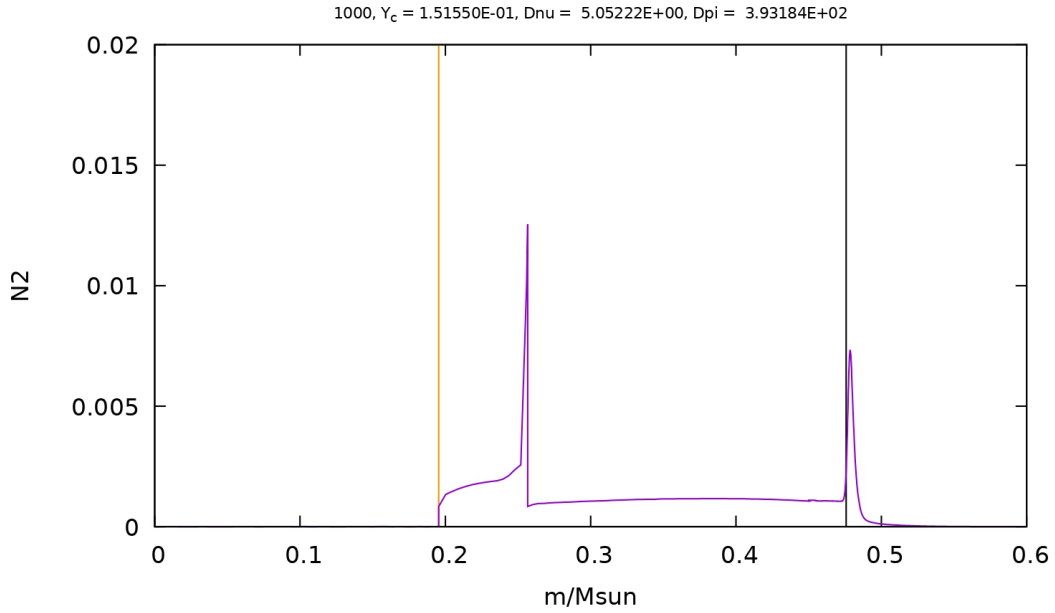

(A) $Y_c = 0.15$

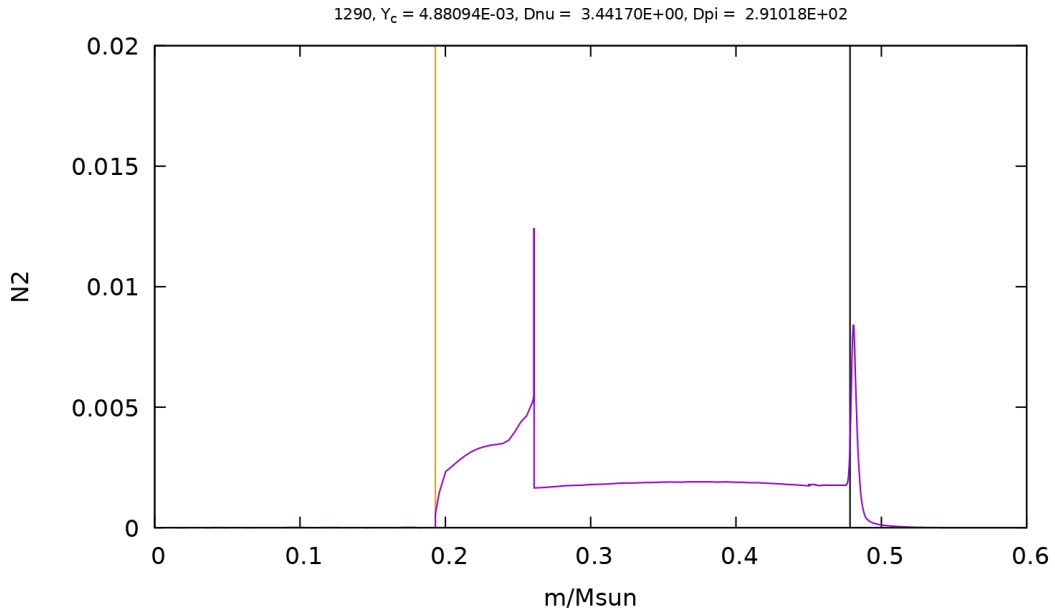

(B) $Y_c = 4.8\ 10^{-3}$

FIGURE 4.9: Brunt-Vaisälä frequency profile as a function of the mass ratio $m/M_\odot$ for 1 $M_\odot$ from the core up to the shell. The mixed core boundary (convective + overshooting layer) is the vertical orange line and the shell boundary is the vertical black line. The figure is divided into sub-figures extracted from the sequence of evolution.

4.3.3 Overshooting Variation

This section presents the effect of the size of the overshooting zone for a reference mass $1M_\odot$.

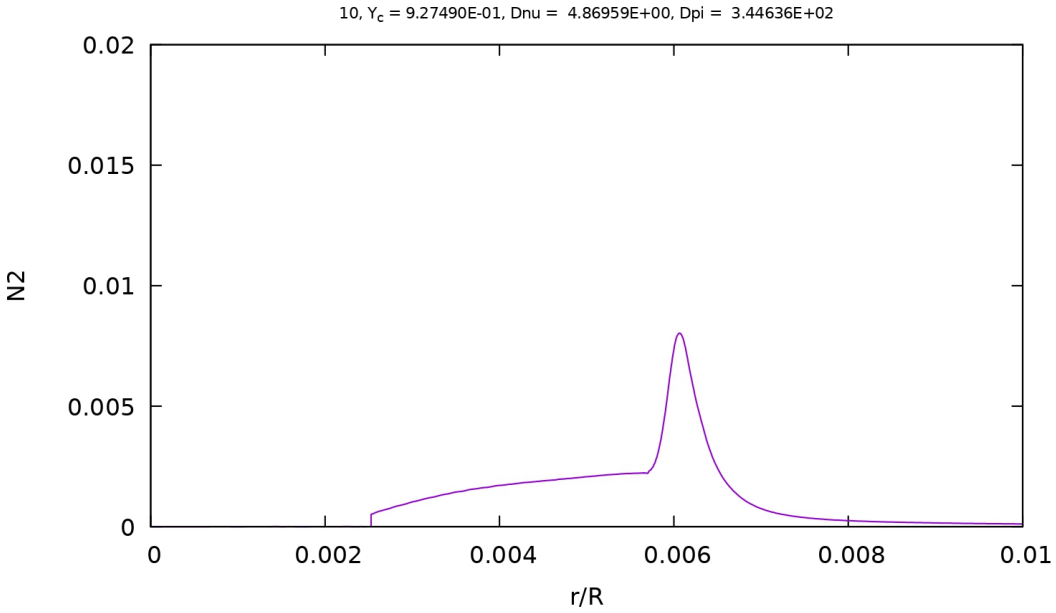

(A) $Y_c = 0.93$

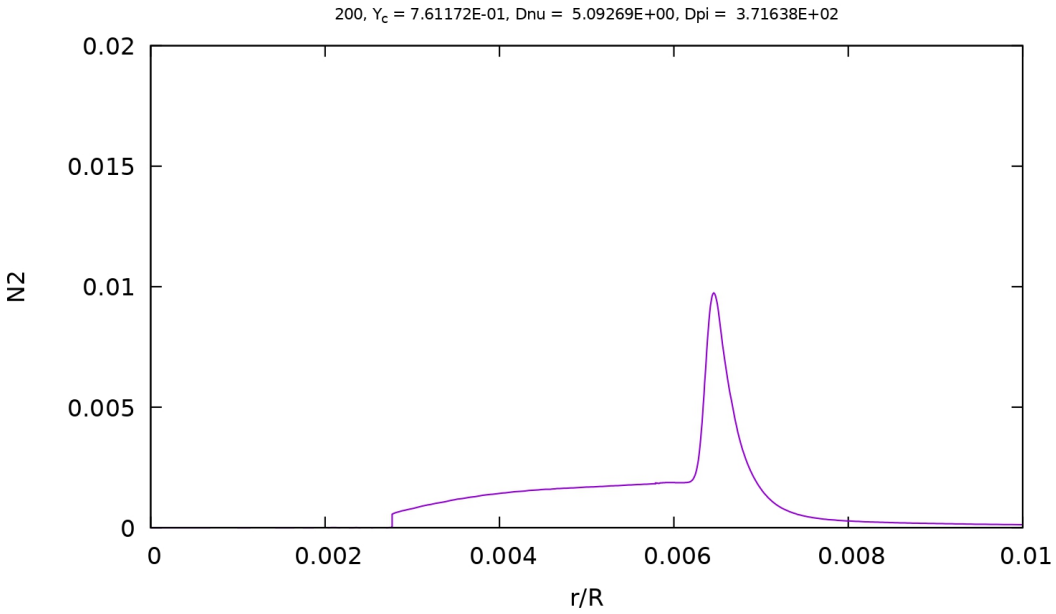

(B) $Y_c = 0.76$

FIGURE 4.10: Brunt-Vaisälä frequency profile as a function of the radius ratio $r/R_\odot$ for 1 $M_\odot$ from the core up to the shell. The figure is divided into sub-figures extracted from the sequence of evolution.

Period Spacing and Large Separation

At first, we compare the $\Delta\Pi - \Delta\nu$ figure, by varying the overshooting (Fig. 4.14). Here, the starting point $\Delta\Pi$ in the diagram is not the same in both stars. However, the lines evolve in parallel and the turn over happens again in the range $Y_c \in [0.34,0.32]$. Brunt-Vaisälä frequency profile could explain this behaviour.

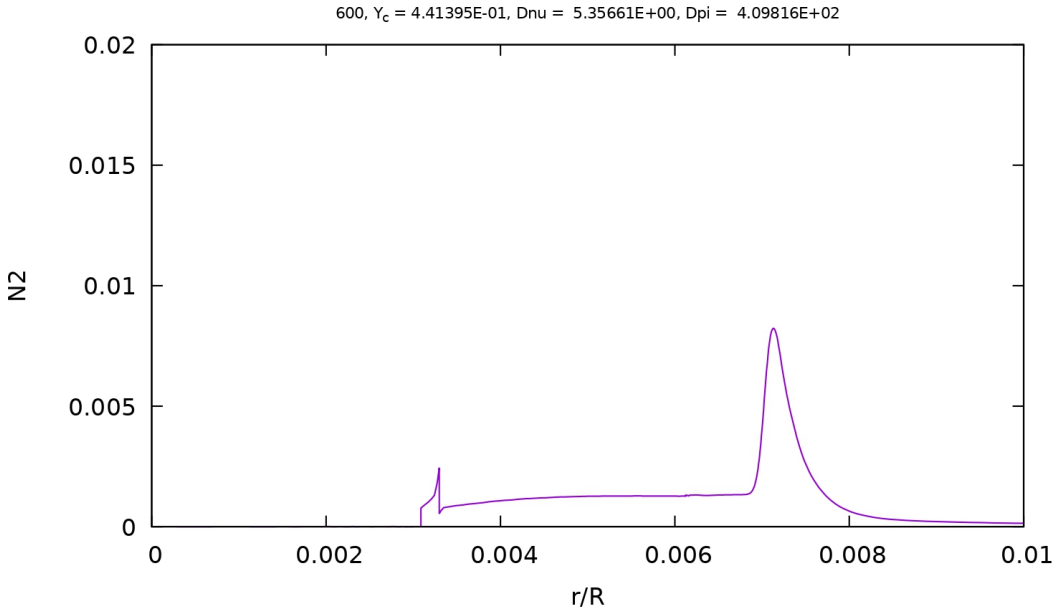

(A) $Y_c = 0.44$

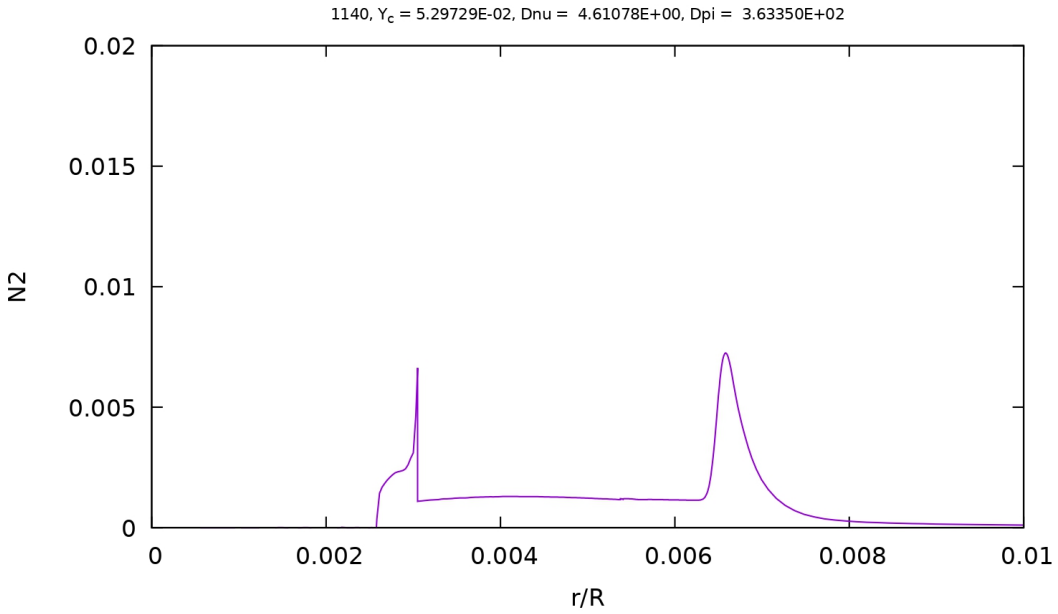

(B) $Y_c = 0.05$

FIGURE 4.11: Brunt-Vaisälä frequency profile as a function of the radius ratio $r/R_\odot$ for 1 $M_\odot$ from the core up to the shell. The figure is divided into sub-figures extracted from the sequence of evolution.

Brunt-Vaisälä Frequency

Figure 4.15 regroups profiles of different stages in the evolution. At the starting point of the sequence (panel 4.15a), the profiles are already distinct in the central part. The step of N^2 at the mixed core boundary is not located at the same mass ratio $m/M_\odot$. This comes from the variation of overshooting that modifies the initial size of the mixed core. For a small overshooting ($\alpha_{ov} = 0.15$), the region where N^2 have a non-zero profile is more extensive and closer to the centre than the other model

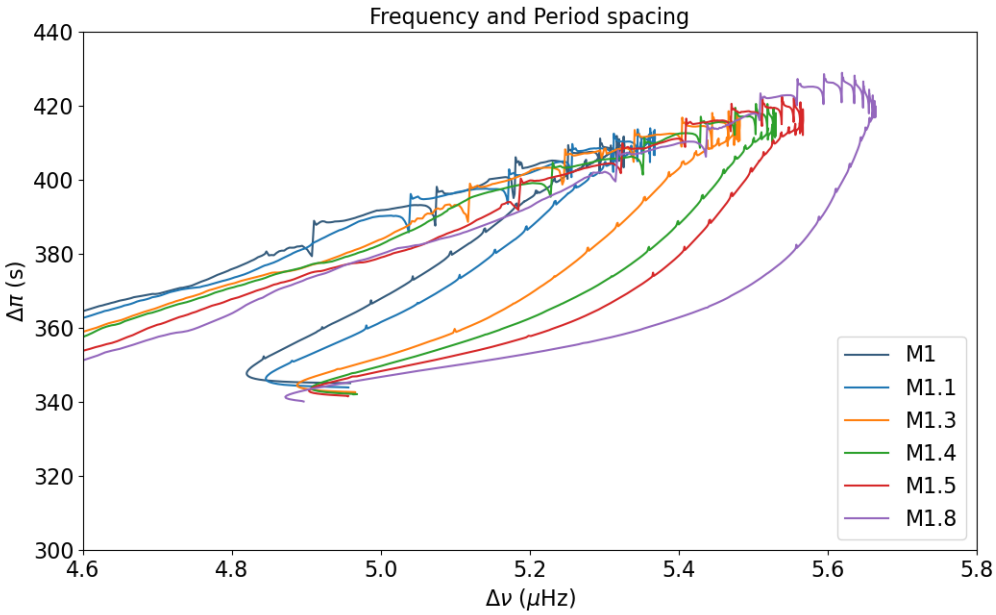

FIGURE 4.12: Figure $\Delta\Pi - \Delta\nu$ from 1 $M_\odot$ to 1.8 $M_\odot$. The bifurcations appear in the range $Y_c \in [0.34, 0.32]$.

of high overshooting ($\alpha_{ov} = 0.50$). A small mixed core therefore produce a smaller radial distance of the Brunt-Vaisälä Frequency profile. As a consequence, the period spacing $\Delta\Pi \sim (N/r)^{-1}$, is smaller for a small overshooting. This explains the seismic $\Delta\Pi - \Delta\nu$ figure 4.14.

Finally, the semi-convective layer also makes a distinction in the two profiles (panel 4.15b and 4.15b). A small overshooting implies that the semi-convective layer is larger. The profile of N^2 in the semi-convective layer is therefore more extended. This also explains the lower period spacing $\Delta\Pi \sim (N/r)^{-1}$.

4.4 Conclusion

From Chapter 2 we concluded that the envelope mass impacts the evolutionary trajectory of a star (Fig.2.2) and the evolution rate (Fig.2.20). Then, to summarise this Chapter: the overshooting of core-He burning stars has an effect in the seismic signature and not much on the evolution. The envelope mass, on the other hand, impacts the seismic signature **and** the evolution.

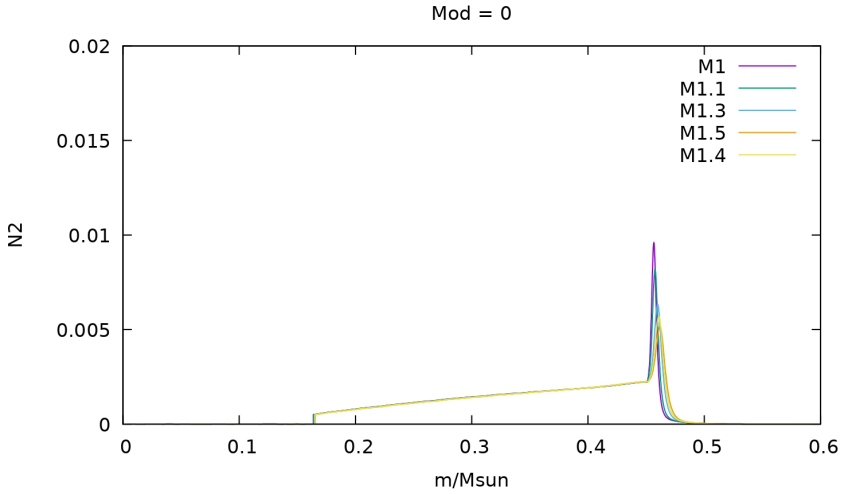

(A) Age = 0 Myr.

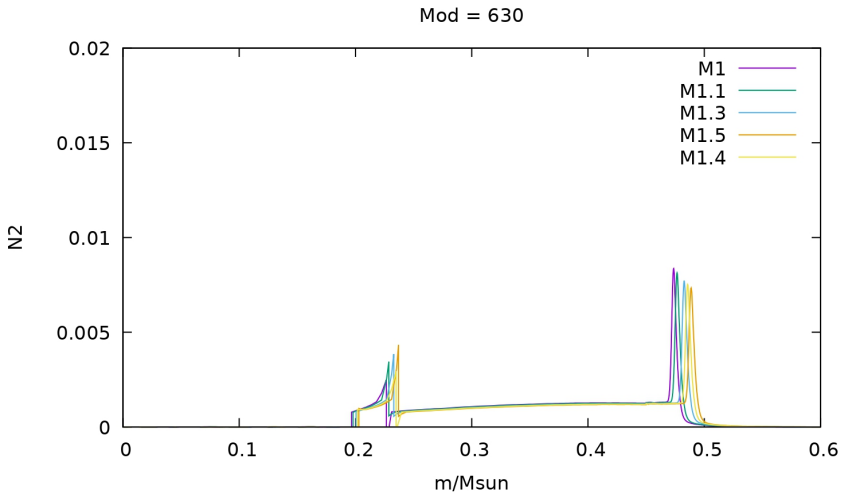

(B) Age = 63 Myr.

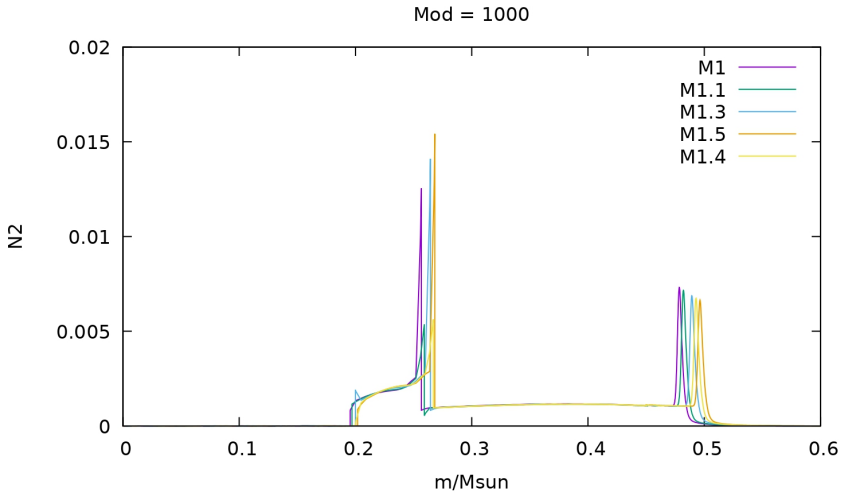

(C) Age = 100 Myr .

FIGURE 4.13: Brunt-Vaisälä frequency profile as a function of the mass ratio $m/M_{\odot}$ from 1 $M_{\odot}$ to 1.8 $M_{\odot}$.

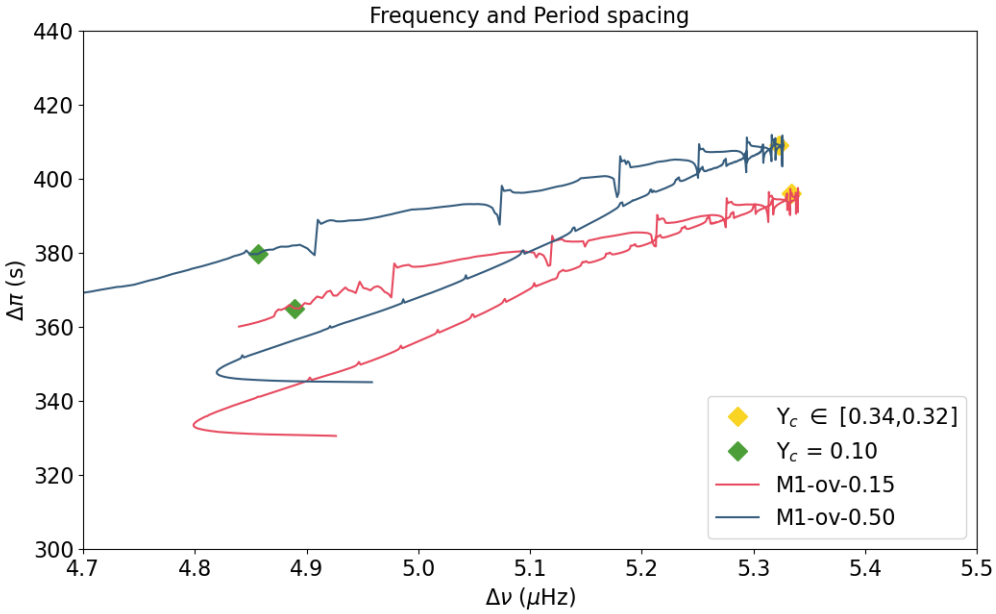

FIGURE 4.14: Figure $\Delta\Pi - \Delta\nu$ for 1 $M_{\odot}$,$\alpha_{ov} = (0.50, 0.15)$. The markers indicate a state of central helium abundance ($Y_c \in [0.34, 0.32]$ in yellow and ,Y_c=0.10 in green).

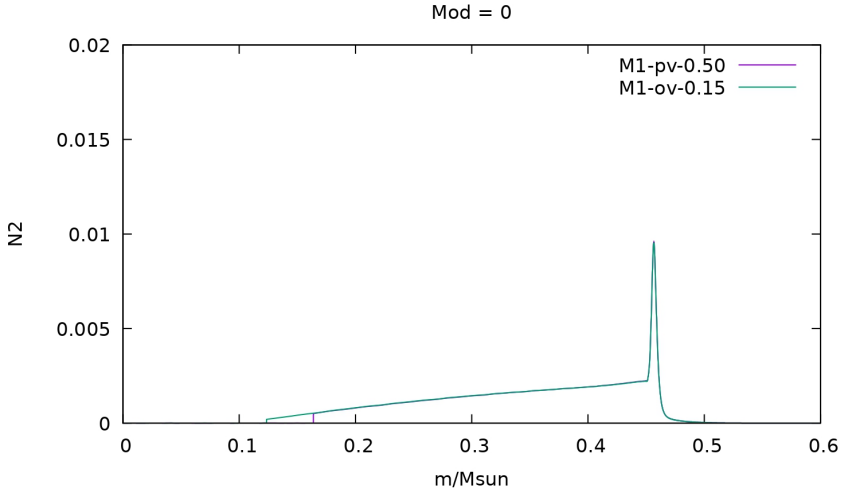

(A) Age = 0 Myr.

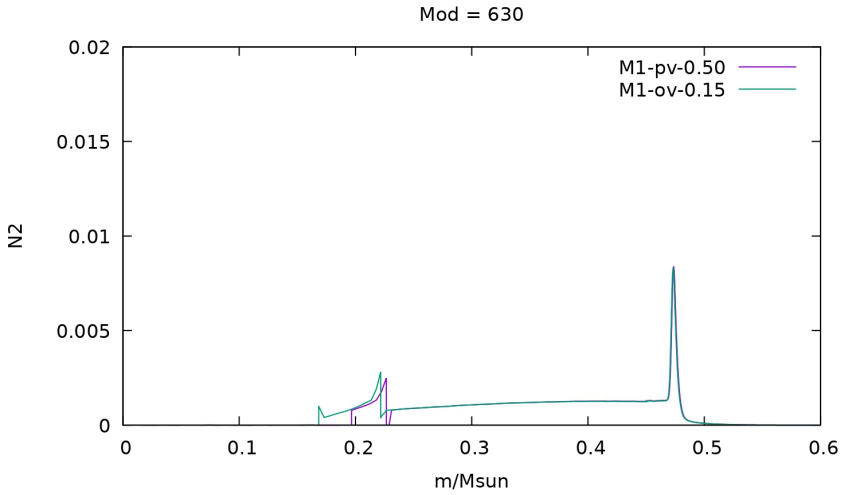

(B) Age = 63 Myr.

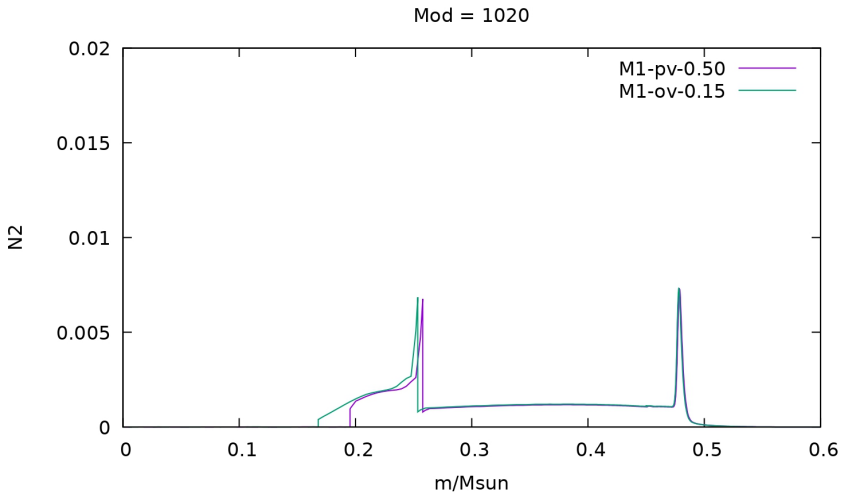

(C) Age = 102 Myr.

FIGURE 4.15: Brunt-Vaisälä frequency profile as a function of the mass ratio $m/M_{\odot}$ for 1 $M_{\odot}$, $\alpha_{ov} = (0.50, 0.15)$ from the core up to the shell of each star.

Chapter 5

Conclusion

In this master thesis, we explored two aspects of low-mass core-He burning stars: the helium core and the mixed modes of stellar oscillations. The primary focus of this work was to study the evolution of the physical parameters of a star of interest in the He-core. This investigation was carried out using two approaches.

The first approach was based on a code of stellar evolution developed by the group "Astrophysique Stellaire Théorique et Astérosismologie" of the Department of Astrophysics, Geophysics and Oceanography of the University of Liège (Scuflaire et al., 2007), *Clés*. This provided a description of the trend of central parameters during the evolution.

The second approach was designed to provide a pedagogic complement to the results obtained with *Clés*. This work was based on a simplified model, the polytropes. A Python code was developed to implement the framework based on the so-called Lane-Emden solutions related to the polytropes. This framework added substance to the discussion and allowed to investigate further the trends in the central parameters profiles.

The last part of the study focused on the asteroseismology of red giants, in particular the evolution of period spacing, large separation and Brunt-Väisälä frequency from the asymptotic theory of pressure and gravity modes, appearing in mixed modes.

To summarise the main results and interpretations of this master thesis:

5.1 Physical Parameters with *Clés*

In Chapter 2, we investigated the evolution of a star of reference, then made the same approach for a set of star of different masses and of different overshooting.

During the evolution of a core-He burning star, its convective core expands and grows in mass, while the H-burning shell surrounding the core becomes less and less active. Given a star of reference, we observed **3 main phases** in the evolution. The **first stage**, which begins at the onset of the core-He burning, describes a surface luminosity that decreases on the horizontal branch, while the He-core luminosity tends to increase. In parallel, the central temperature and opacity increase due to the He-core mass increase and the central density decreases to maintain control of the nuclear reactions. The radiative gradient, on the other hand, has a peculiar increase beyond the overshooting layer that ends up in the appearance of a semi-convective layer.

The **second phase**, close to a central helium abundance of $Y_c \sim 0.33$ marks a big turn in the evolution. Due to the exhaustion of central helium, the central part of the star contracts to maintain a thermal equilibrium which slows down the extension of the mixed core. This induces a slow reactivation of the shell that affects the surface luminosity and creates a turn over in the H-R diagramn trajectory. This is the beginning of the **final phase**: the shut down of the core-He burning due to an almost complete exhaustion of fuel. At this point, the whole core contracts to maintain the equilibrium of the stellar structure and the total luminosity continues to increase with the luminosity of the shell. This stage marks the end of the Horizontal Branch.

Finally, the envelope mass of a given star makes some impacts on the evolution. In addition to changing the total luminosity, it also influences slightly the time spend on the horizontal branch. The higher is the mass, the faster comes the phase of central helium exhaustion. On the other hand, despite changing the chemical profiles in the core, the overshooting parameter does not significantly influence the evolutionary trajectory.

The highlight of the logarithmic relation between pressure and density ($lnP \sim \gamma\ ln\rho + cst$) is the basis of the following Chapter on polytropes.

5.2 Physical Parameters with Polytropes

In Chapter 3, we made a different and simpler approach to investigate the origin of the trends observed in Chapter 2 for the convective core. Based on the observed fixed slope of the logarithmic Pressure and Density relation, we concluded that the polytropes model could be interesting to describe the physical parameters. The aim of this Chapter was to test the efficiency of this model and give a complement to the results obtained with *Clés*.

The polytropes model forms a mathematical framework based on the so-called Lane-Emden solutions, where they are defined by the density and central density $w = (\rho/\rho_c)^{1/n}$. With the use of some approximations, a clear mathematical link was made between the whole physical parameters of interest. This way, the parameters were implemented with the use of the Lane-Emden solutions.

The results showed that the model described nicely the parameters trend and had limitations in final stages of evolution due to its simplicity. The more evolved is a star on its sequence of evolution, the less the model holds to describe the quantities that have the most complicated analytical form (mainly the Radiative Gradient). However, through this model, the origin of the rise of the radiative gradient was highlighted and it showed that the minimum of radiative gradient is a fixed point of the variable z. The rise of the opacity with the extension of the core induces the gradient rise and the increase of central opacity is caused by the He-core that grows in metallic elements. Finally, it showed that further aspects could be explored as the model has only been tested for a reference mass.

5.3 Red Giant Asteroseismology

In the last Chapter 4, we studied the period spacing and large separation from the asymptotic theory of the mixed modes and the Brunt–Väisälä frequency profiles during the sequence of evolution. This was made using the same stellar evolution code, *Clés*. At first, we analysed the results for a star of reference, then we made the same approach for a set of stars of different mass and of different overshooting. As the main interest was in the study of the core of a reference star, we examined in particular the period spacing behaviour specific to the g-modes, propagating in this part of the core.

The results showed that the dependence of the period spacing with the Brunt–Väisälä frequency $\Delta\Pi \sim (\int N/r)^{-1}$ can be related to the observed seismic $\Delta\Pi - \Delta\nu$ diagram. Due to the presence of a convective core, where the real gradient is equal to the adiabatic gradient, the Brunt–Väisälä frequency N^2 has no profile throughout the region. On the mixed core boundary (convective + overshooting), a profile appears. In the **first phase** of evolution (from Y_c=0.9 to $Y_c \simeq$0.33) , we concluded that the trend of $\Delta\Pi$ to increase during the evolution was related to the decrease of N^2 and the extension of the core, increasing the radial distance r. We also noticed that the the semi-convective region creates a step in the profile of N^2 due to the discontinuity of density profile and chemical composition . In the **second phase** and **last phase** (from $Y_c \simeq$0.33 to $Y_c \rightarrow$0) , the central helium exhaustion creates a general increase of N^2 due to a density increase. This change of behaviour draws a bifurcation in the $\Delta\Pi - \Delta\nu$ figure, at the same Y_c.

The next results showed that a variation of the envelope mass of a star had an effect on the seismic signature. This could come from the difference of the rate of evolution between stars of different mass. The speed at which the profile of N^2 decreases in the shell is different as well as the speed at which the core mass increase. A less massive star have a decrease of N^2 in the shell higher than the other and a faster increase of $\Delta\Pi$.

Finally, we observed that the overshooting, despite having small effect on the evolution, have a significant effect on the seismic signature. This is due to the size of the semi-convective region, which differs according to the initial overshoot. This layer has a stabilising effect that creates a variable chemical composition and affects the Brunt–Väisälä frequency profile. A large semi-convective layer leads to a higher general value of N^2. In turn, it influences the period-spacing $\Delta\Pi$, which becomes smaller compare to a star with a small semi-convective layer.

5.4 Conclusion

In conclusion, this master thesis has provided an analysis of the central region of core-He burning stars through the study of its physical parameters. A simplified model based on polytropes has been added as a complement to the discussion and has provided an additional understanding of the evolution of the parameters within the convective core. Finally, it was used to introduce the asymptotic theory in mixed modes where the links between the Brunt-Väisälä frequency, the period spacing and the behaviour of the physical parameters were highlighted.

Appendix A

Polytropes Code

A.1 Lane-Emdem Solutions

```
import matplotlib.pyplot as plt
import numpy as np
import math

############################################################
###########----------------------------------###########
###########       Runge-Kutta Functions       ###########
###########----------------------------------###########
############################################################


def w(xi,n):
    w = 1-(xi**2/6) + (n/120)*(xi**4) - (n*(8*n-5)*xi**6)/15120
    return w

def dw(xi,w,v): # derivative dw/dx = v
    return v

def dv(xi,w,v,n): # derivative dv/dx
    return -w**n - (2*v/xi)


def rk4(x0,w0,v0,h,n): # functions of runge-kutta, return solutions v(z
                                    ), w(z), and the points z

    w = np.zeros(N) # solutions vectors (on each point on the grid)
    v = np.zeros(N)
    xi = np.zeros(N)

    #----Assign the initial conditions to the solution vectors:

    xi[0]= x0
    v[0]= v0
    w[0]= w0

    if n==3/2 :
        for i in range(N-1):

                k1 = h * dw(xi[i], w[i], v[i])
                l1 = h * dv(xi[i], w[i], v[i], n)

                k2 = h * dw(xi[i] + (h/2), w[i] + (k1/2), v[i] + (l1/2)
                                                    )
                l2 = h * dv(xi[i] + (h/2), w[i] + (k1/2), v[i] + (l1/2)
                                                      , n)
```

```
                k3 = h * dw(xi[i] + (h/2), w[i] + (k2/2), v[i] + (l2/2)
                                                    )
                l3 = h * dv(xi[i] + (h/2), w[i] + (k2/2), v[i] + (l2/2)
                                                    , n)

                k4 = h * dw(xi[i] + h, w[i] + k3, v[i] + l3)
                l4 = h * dv(xi[i] + h, w[i] + k3, v[i] + l3, n)


                w[i+1] = w[i] + (k1+2*k2+2*k3+k4)*(1/6)
                v[i+1] = v[i] + (l1+2*l2+2*l3+l4)*(1/6)

                xi[i+1] = xi[i] + h

        # To determine where the solution w(x) breaks when coming close
                                                    to 0
        a=0
        sol=[]
        dev=[]
        x=[]
        while w[a] >= 0 :
            sol.append(w[a])
            dev.append(v[a])
            x.append(xi[a])

            a+=1
        print('index= ',a-1, ', xi =',x[a-1], "w =",sol[a-1], "dw/dxi =
                                                    ",dev[a-1])
        return x , w , v, sol, dev

    if n != 3/2 :

        for i in range(N-1):


                k1 = h * dw(xi[i], w[i], v[i])
                l1 = h * dv(xi[i], w[i], v[i], n)

                k2 = h * dw(xi[i] + (h/2), w[i] + (k1/2), v[i] + (l1/2)
                                                    )
                l2 = h * dv(xi[i] + (h/2), w[i] + (k1/2), v[i] + (l1/2)
                                                    , n)

                k3 = h * dw(xi[i] + (h/2), w[i] + (k2/2), v[i] + (l2/2)
                                                    )
                l3 = h * dv(xi[i] + (h/2), w[i] + (k2/2), v[i] + (l2/2)
                                                    , n)

                k4 = h * dw(xi[i] + h, w[i] + k3, v[i] + l3)
                l4 = h * dv(xi[i] + h, w[i] + k3, v[i] + l3, n)


                w[i+1] = w[i] + (k1+2*k2+2*k3+k4)*(1/6)
                v[i+1] = v[i] + (l1+2*l2+2*l3+l4)*(1/6)

                xi[i+1] = xi[i] + h


        return xi,w,v

##############################################
#-------------Initial Conditions-------------#
```

```
h = 1e-3 # step between points
t_max=10 # x_max in the interval [x_0,x_max]
N=int(t_max/h) # total number of points in the interval

x0 = 1e-2 # x=z^2 and z_0 = 1e-2
n = 3/2 # theoretical polytropic index
n1 =0
n2 =1
n3 =3
n4 =2

w01=w(x0,n)
w02=w(x0,n1)
w03=w(x0,n2)
w04=w(x0,n3)
w05=w(x0,n4)




#----Lane-Emden Solutions for several polytropic index ----#

x,w1,v, sol , dev =rk4(x0,w01,0,h,n) # sol = w(z) and dev = v(z) = dw/
                                       dz
x1,w2,v=rk4(x0,w02,0,h,n1)
x2,w3,v=rk4(x0,w03,0,h,n2)
x3,w4,v=rk4(x0,w04,0,h,n3)
x4,w5,v=rk4(x0,w05,0,h,n4)

plt.plot(x2,w2,label='0')
plt.plot(x2,w3,label='1')
plt.plot(x2,w1,label='3/2')
plt.plot(x2,w5,label='2')
plt.plot(x2,w4,label='3')

plt.plot(x2,np.zeros(len(w2)))

plt.ylim([-1,1])
plt.legend()
plt.show


#\\\\\\\\\\\\\\\\\\\\\\\\\\\\\\\\\\\\\\\\\\\\\\\\\\\\\\\\\\\\\\\\\\\\\\\\\\\\#

#-----Comparison for analytical solution n=0 and n=1 ------#

def w_0(x):
    F=[]
    for i in x :
        f=(1-((1/6)*i**2))
        F.append(f)
    return F

def w_1(x):
    F=[]
    for i in x :
        f=math.sin(i)/i
        F.append(f)
    return F


sol_0=w_0(x2)
sol_1=w_1(x2)
```

```
#---------For n=0---------#

plt.plot(x2,w2,label=r'$w_0 \ $ numeric')
plt.plot(x2,sol_0,label=r'$w_0 \ $ analytic')
plt.plot(x2,np.zeros(len(w2)))

plt.ylim([-1,1])
plt.legend()
plt.show()

#------For n=1------#

plt.plot(x2,w3,label=r'$w_1 \ $ numeric')
plt.plot(x2,sol_1,label=r'$w_1 \ $ analytic')
plt.plot(x2,np.zeros(len(w2)))


plt.legend()
plt.show()
```

A.2 Clés Data Extraction

```
import csv
import numpy as np
import math
from scipy import stats

#########################################################
##########-----------------------------------##########
##########  DATA EXTRACTION from CLES file ##########
##########-----------------------------------##########
#########################################################

rows = []
with open("C:/Users/Lucy Itoko/Documents/Master 2/M moire/lane-emden/
                                    Autre Mod/M1/Mod 40/M1-0040.txt", '
                                    r') as file:
    csvreader = csv.reader(file)
    header = next(csvreader)
    for row in csvreader:
        rows.append(row)


# row[1]= 1st data line, row[0] are the head names of the data column
# 1 data line = 1st line of each column parameters of the star  (names
                                    in row[0])



N=len(rows)-1 # number of line in the data matrix (=number of lines in
                                    the CSV file columns) removing the
                                    first line (names of the column)

mat=np.zeros([N,28]) # matrix containing the data column of the CSV
                                    file
```

```
for i in range(0,N): # From 1 to N-1

    l=str(rows[i+1][0]).split()
    a=l[1:] # To avoid the 1st element, the layer number
    b=[]

    for j in a :
        b.append(float(j))
    mat[:][i]=b



#---Fill in the physical quantities data from CLES file into vectors (
                                    density, temperature, luminosity
                                    and so on)

rho_cles=[]
P_cles=[]
Dgrad=[]
Dad=[]
Drad_cles=[]
x_cles_original=[]
mu_cles=[]
L_cles=[]
x_m0=[]
enuc_He_cles=[]
X=[]
Y=[]
O=[]
C=[]
Y=[]
kap_cles=[]
T_cles=[]

for i in mat:
   rho_cles.append(i[2])   #density
   P_cles.append(i[4])  #pressure
   x_cles_original.append(i[0]) #   r/R
   Drad_cles.append(i[9])
   Dad.append(i[10])
   Dgrad.append(i[9]-i[10])
   mu_cles.append(i[25])
   L_cles.append(i[5])
   enuc_He_cles.append(i[20]) # Core-He nuclear rate
   x_m0.append(i[1]) #  m/M
   X.append(i[6]) # H mass fraction
   Y.append(i[27]) # He mass fraction
   O.append(i[24])
   C.append(i[22]) # C mass fraction
   kap_cles.append(i[13]) # opacity
   T_cles.append(i[3])


#---Schwarzschild criterion, convective core boundary
for index, val in enumerate(Dgrad) :
    if val <=0 :
        c_c=index
        print(index,val)
        break
```

```
x_cles=np.concatenate((x_cles_original[:123], x_cles_original[124:140],
                                    x_cles_original[141:])) #To avoid
                                    the double points in the list


#--Makes line to delimit the convective core in the figures

x_conv=x_cles_original[:c_c]
r_cnv=[]
for i in range(len(x_cles_original)):
    r_cnv.append(x_conv[-1])


#------ Convert the relative mass m/M into the mass m ------#

m_tot=1.9884099E+33
mass_cles=[]
for i in x_m0:
    mass_cles.append(i*m_tot)
```

A.3 Physical Variables Implementation

A.3.1 Polytropic Index Approximation

```
rho_sc = rho_cles[:c_c] # takes data up to the convective core boundary
                                    (limit of the model)
P_sc = P_cles[:c_c]


####---Linear regression with the data for log P-\rho  to find the
                                    coefficients of the straight line
                                    equation.


xlog = np.log(rho_sc)
ylog = np.log(P_sc)

slope, ordo, r_value, p_value, std_err = stats.linregress(xlog, ylog)
n_approx= 1/(slope-1)

print("gamma = ",slope, "K = ", math.exp(ordo)  )
print("n =",n_approx, "n_theoric =", 3/2)
```

A.3.2 Implementation

```


#------------Lane-Emden Solutions------------#

x_th,w_th,v_th=rk4(x0,w06,0,h,n_app) # Using the approximated
                                    polytropic index n_app

###---Extract existent solutions w(z) from the vector as the solutions
                                    for a polytropix index of 3/2 does
                                    not exist in the negative
b=0
w_ap=[]
v_ap=[]
x_ap=[]
while w_th[b] >= 0 :
```

```
    w_ap.append(w_th[b])
    v_ap.append(v_th[b])
    x_ap.append(x_th[b])

    b+=1
#########################################################
###########-----------------------------------###########
###########  Modelling physical quantities  ###########
###########-----------------------------------###########
#########################################################



#----------- Sphere mass M(z) -----------#

def ln_m(z,rho,v,n,K,r):

    F=[]
    for i, val in enumerate(z):
        f = (r[i]**3)*(1/val)*(-4*math.pi*rho)*v[i]
        F.append(f)

    return F

#----------- Pressure P(z) -----------#

def ln_P(rho,w,gamma,K,n):
    F=[]
    for i in w :
        f = gamma*math.log(rho) + gamma*n*math.log(i) + math.log(K)
        F.append(math.exp(f))
    return F

#----------- Density \rho(z) -----------#

def ln_rho(rho,n,w):
    F=[]
    for i in w :
        f = math.log(rho) + n*math.log(i)
        F.append(math.exp(f))
    return F

#----------- Temperature T(z) -----------#

def ln_T(rho,w,gamma,K,n,m_u,k_b,mu,T_c):
    F=[]
    a=(1/1.1364436159524631)

    for i, val in enumerate(w) :
        f = (gamma-1)*math.log(rho) + (gamma-1)*n*math.log(val) + math.
                                        log(K*(m_u/k_b)*a) + math.
                                        log(mu[i])
        F.append(math.exp(f))

    return F

#----------- Nuclear Rate -----------#

def nucl(T, T_c, Y_c, rho):
    F=[]
    c=858062289818.0402

    for i, val in enumerate(T) :
```

```
        f = c*(rho[i]**2)*(Y_c**3)*(((val*1e-8)**(-3))*math.exp(-44.027
                                                    /(val*1e-8)))
        F.append(f)

    return F

#----------- Luminosity L(z) -----------#

def L(z,T,rho,m, Y_c):
    F=[]
    c=858062289818.0402

    for k in range(1,len(z)):
        N=len(z[:k])
        g=np.zeros(N-1)
        dm = deriv(m, z[:k])
        for i in range(N-1) :
            g[i] = rho[i]**2 * (((T[i]*1e-8)**(-3))*math.exp(-44.027/(T
                                                    [i]*1e-8)))*dm[i]

        F.append( c*(Y_c**3)*integral(g, z[:k]))
    return  F[122],F,dm


#----------- Radiative Gradient -----------#

def D_rad(kap,P,T,m,L) :
    a=0.00022450410695358747
    F=[]
    F.append(0)
    for i in range(1,len(L)) :
        f = (L[i]*3*kap[i]*P[i])/((16*math.pi*G*a)*m[i]*(T[i])**4 )
        F.append(f)
    F[0]=F[1]
    return F

#----------- Opacity -----------#

def ln_kap(Y,X,T,rho,O,C):
    k = np.zeros(len(T))
    k_sc=np.zeros(len(T))
    for i in range(len(T)):

        k_sc[i] = 0.2*(1+ X[i])

        k[i]=(k_sc[i] + (3.8e22*(1+X[i])*(Y[i] + X[i] + ((O[i]*8**2)/15
                                                    .99) + ((C[i]*6**2)/12)) *
                                                    rho[i]*T[i]**(-7/2)))


    return k,k_sc


#-----------------------------------------------------#
#-------Function to numerically solve Luminosity integral-------#

def deriv(f,z):
    N=len(z)
    s = np.zeros(N-1)
    for i in range(N-1):
        s[i] = (f[i+1] - f[i]) / (z[i+1] - z[i])
    return s
```

```
def integral(f,z):
    s=0
    N=len(f)
    for i in range(N-1):
        s = s + ((z[i+1]-z[i])/2) * (f[i] + f[i+1])
    return s

#-----------------------------------------------------#
###########---------- Constants ----------#############

rho_c = rho_cles[0] ########- central density (ClES)

gamma =  slope
K =  math.exp(ordo)
G = 6.743e-8
kBoltz = 1.380649e-16
m_u = 1.66053906660e-24

T_c=T_cles[0] #######- central temperature (ClES)
Y_c= Y[0]
R_total=  9.9390070E+00 * 6.957e10 #######- Total radius of the star (1
                                    M_0 ClES)

#-----------------------------------------------------#
#------------Functions to convert z into r------------#

def convert(z,K,n,rho):

    x=[] # coordonates r
    y=[] #coordonates r/R
    A=( (4*(math.pi)*G)/((n_app+1)*K))**(1/2) *(rho_c)**((n_app-1)/(2*
                                        n_app))
    for i in z :
        g=(i/ A)
        f= (i/ A)/R_total
        x.append(f)
        y.append(g)
    return x,y

#------------Functions to convert r into z------------#

def invert(r,K,n,rho):
    x=[]
    A=( (4*(math.pi)*G)/((n_app+1)*K))**(1/2) *(rho_c)**((n_app-1)/(2*
                                        n_app))
    for i in r :
        g=i*R_total
        f= (g*A)
        x.append(f)

    return x

#-------------------------------------------------------------#
################----------------------------------##############

r,r_true=convert(x_ap, K, n_app, rho_c) # r_true = r and r = r/R
z_retrieve=invert(x_cles_original,K,n_app,rho_c) # conversion x_cles in
                                    z
z_sc=z_retrieve[c_c-1] # z of the convective boundary (Schwarzschild)
z_cnv=invert(r_cnv,K,n_app,rho_c)  # z of the convective boundary
                                    converted from Cl s data
```

```
###########----------------------------###########
### To compare ClES with the simplified model, ###
###       the grid points must be the same      ###
###########----------------------------###########

end= len(r)-1
index=[0]
r_x=[r[0]]
w_x=[w_ap[0]] # To match grid points from ClES with grid points from
                                    the model
v_x=[v_ap[0]]
z_x=[x_ap[0]] #Same, to match the derivatives v
r_true_x=[r_true[0]]
for i, val in enumerate(x_cles):

    for k,truc in enumerate(r):
        if k==end:
            pass
        else:
            if val > r[k] and val < r[k+1]:
                index.append(k)
                w_x.append(w_ap[k])
                r_x.append(r[k])
                v_x.append(v_ap[k])
                z_x.append(x_ap[k])
                r_true_x.append(r_true[k])
            else:
                pass



#----Results----#
rho= ln_rho(rho_c,n_app,w_ap)
P=ln_P(rho_c, w_x, gamma, K, n_app)
T=ln_T(rho_c, w_x, gamma, K, n_app, m_u, kBoltz, mu_cles,T_c)
mass=ln_m(z_x, rho_c, v_x, n_app, K, r_true_x)
kap,k_ff = ln_kap(Y,X,T_cles,rho_cles,0,C)
enuc_He=nucl(T_cles, T_c, Y_c, rho_cles)
L_s,L,dm = L(z_x,T_cles,rho_cles,mass,Y_c)
a1=len(L)
Drad = D_rad(kap_cles[:a1],P[:a1],T[:a1],mass[:a1],L[:a1])

#----To match the vector size of the polytrope model results
x_cles_cut=x_cles[:a1]
mass_cles_cut=mass_cles[:a1]
```

Bibliography

Basu, Sarbani and Saskia Hekker (2020). "Unveiling the Structure and Dynamics of Red Giants With Asteroseismology". In: *Frontiers in Astronomy and Space Sciences* 7. DOI: 10.3389/fspas.2020.00044. URL: https://doi.org/10.3389%2Ffspas.2020.00044.

Constantino, Thomas et al. (2015). *The treatment of mixing in core helium burning models - I. Implications for asteroseismology*. arXiv: 1506.01209 [astro-ph.SR].

"Equations of Stellar Structure" (2005). In: *Evolution of Stars and Stellar Populations*. John Wiley Sons, Ltd. Chap. 3, pp. 49–103. ISBN: 9780470033456. DOI: https://doi.org/10.1002/0470033452.ch3. eprint: https://onlinelibrary.wiley.com/doi/pdf/10.1002/0470033452.ch3. URL: https://onlinelibrary.wiley.com/doi/abs/10.1002/0470033452.ch3.

Kippenhahn, Rudolf, Alfred Weigert, and Achim Weiss (2013). *Stellar Structure and Evolution*. DOI: 10.1007/978-3-642-30304-3.

Miglio, Andrea et al. (May 2008). "Probing the properties of convective cores through g modes: high-order g modes in SPB and γ Doradus stars". In: 386.3, pp. 1487–1502. DOI: 10.1111/j.1365-2966.2008.13112.x. arXiv: 0802.2057 [astro-ph].

Mohan, Chander and A. Al-Bayaty (Nov. 1980). "Power-series solutions of the Lane-Emden equation". In: *Astrophysics and Space Science* 73, pp. 227–239. DOI: 10.1007/BF00642378.

Mosser, B. et al. (2014). "Mixed modes in red giants: a window on stellar evolution". In: *Astronomy &amp Astrophysics* 572, p. L5. DOI: 10.1051/0004-6361/201425039. URL: https://doi.org/10.1051%2F0004-6361%2F201425039.

Roxburgh, Ian W. and Lynne M. Stockman (1999). "Power series solutions of the polytrope equations". In: *Monthly Notices of the Royal Astronomical Society* 303.3, pp. 466–470. DOI: 10.1046/j.1365-8711.1999.02219.x.

Scuflaire, R. et al. (2007). "CLÉS, Code Liégeois d'Évolution Stellaire". In: *Astrophysics and Space Science* 316.1-4, pp. 83–91. DOI: 10.1007/s10509-007-9650-1. URL: https://doi.org/10.1007%2Fs10509-007-9650-1.

"The Hydrogen Burning Phase" (2005). In: *Evolution of Stars and Stellar Populations*. John Wiley Sons, Ltd. Chap. 5, pp. 117–159. ISBN: 9780470033456. DOI: https://doi.org/10.1002/0470033452.ch5. eprint: https://onlinelibrary.wiley.com/doi/pdf/10.1002/0470033452.ch5. URL: https://onlinelibrary.wiley.com/doi/abs/10.1002/0470033452.ch5.